

OPTIMAL SUBSTRATE FOR DIRECT DETECTION
OF LIGHT DARK MATTER

A DISSERTATION
SUBMITTED TO THE DEPARTMENT OF PHYSICS
AND THE COMMITTEE ON GRADUATE STUDIES
OF STANFORD UNIVERSITY
IN PARTIAL FULFILLMENT OF THE REQUIREMENTS
FOR THE DEGREE OF
DOCTOR OF PHILOSOPHY

To Chin Yu
December 2022

© 2022 by To Chin Yu. All Rights Reserved.
Re-distributed by Stanford University under license with the author.



This work is licensed under a Creative Commons Attribution-3.0 United States License.
<http://creativecommons.org/licenses/by/3.0/us/>

This dissertation is online at: <https://purl.stanford.edu/sh926jm9954>

I certify that I have read this dissertation and that, in my opinion, it is fully adequate in scope and quality as a dissertation for the degree of Doctor of Philosophy.

Blas Cabrera, Primary Adviser

I certify that I have read this dissertation and that, in my opinion, it is fully adequate in scope and quality as a dissertation for the degree of Doctor of Philosophy.

Noah Kurinsky, Co-Adviser

I certify that I have read this dissertation and that, in my opinion, it is fully adequate in scope and quality as a dissertation for the degree of Doctor of Philosophy.

Peter Graham

I certify that I have read this dissertation and that, in my opinion, it is fully adequate in scope and quality as a dissertation for the degree of Doctor of Philosophy.

Chao-Lin Kuo

Approved for the Stanford University Committee on Graduate Studies.

Stacey F. Bent, Vice Provost for Graduate Education

This signature page was generated electronically upon submission of this dissertation in electronic format.

Abstract

The topic of dark matter (DM) and its possible interaction with ordinary matter has occupied the central stage of the field of particle physics in recent decades. One line of research attempts to directly detect such interaction in a controlled lab environment with extremely sensitive (and in some cases even quantum-limited) sensors. SuperCDMS is one such experiment that utilizes transition-edge sensors (TES) fabricated on large silicon or germanium crystals cooled to cryogenic temperatures (around 50 mK). Silicon and germanium are typically used as the substrate material since they are cost-efficient and well-understood. Numerous alternative substrates have been proposed over the years but these novel substrates are often complex and difficult/costly to grow or make. In other cases they may require significant improvement in detector technology in order to work as intended. As such silicon and germanium remain the dominant substrate material in DM direct detection experiments.

Expanding the repertoire of substrate materials is valuable. It can lead to better sensitivity to DM interactions, and a higher degree of material complementarity across different detectors and experiments. The latter point is especially important as we move deeper into the low mass region and look for lighter and lighter DM particles. We can begin to encounter backgrounds caused by non-perturbative many-body effects that are highly material-specific. Having substrates of different materials operating under similar conditions provides information about the nature of such backgrounds as we can compare the response in different materials to break any potential degeneracy not resolved by just having silicon and germanium.

The work presented in this thesis is an attempt to systematically survey and understand the various solid state physics pertinent to the DM direct detection, and as application suggest criteria for the optimal substrate material to be used for various interaction channels. Towards the end of this work we will present concrete examples of substrates that can potentially be used in the next generation of DM detection experiments.

Acknowledgements

The past 5 years has been filled with turbulence - my father's battle with cancer and eventual passing, complete halt of lab activities due to COVID lock-down, and my own (luckily short) battle with cancer. It would have been impossible to achieve what I have today without the following people:

SLAC Richard Partridge, Paul Brink, Noah Kurinsky, Tsuguo Aramaki, Michael Kelsey, Tina Cartaro, Robert Cameron, Joseph Garvie

Without the unyielding support and guidance from Richard this academic journey would have been very short-lived. Richard paid great attention to ensure that I am making constant progress especially during the difficult times of COVID lock-down. He granted me great academic freedom to explore theoretical and computational topics while also providing me with plenty of hands-on experiences and projects in order to make sure that I develop a well-rounded understanding in all aspects of the SuperCDMS experiment. He has made me not only a better physicist, but also a better engineer. Paul has been an endless source of inspirations and knowledge. I always learn something new whenever I talk to him. Without his patient and pedagogical explanations I would not have understood nearly as much as I do today. Noah is my initial contact in SuperCDMS. I first learned about the group and the physics of cryogenic particle detectors when we met at orientation. He has since been a great mentor and a close friend, and we collaborated on many interesting ideas that eventually formed the basis of this thesis. Tsuguo taught me about many practical aspects of experimental physics and the academic career. His words of support has been a great source of confidence. On the computing side, I am constantly in awe of Mike's and Tina's technical prowess when it comes to software and programming. I have learned many tricks from their bags that will probably last me a life-time. Rob has always been a warm presence at group meetings and eager to ask the “dumb” questions I am at times too afraid to ask myself. Joseph briefly shared a cubicle with me. His lively demeanor made the otherwise empty and borderline depressing space much more enjoyable.

Stanford Blas Cabrera, Betty Young, Francisco Ponce, Jon Leyva, Steven Yellin

Blas is an intellectual powerhouse and source of infinite wisdom. I am constantly impressed by his ability to quickly dissect and debug confusing results and issues. I am grateful for having him as my co-adviser. Betty and Francisco both taught me a lot about the practicalities of cryogenics at the Stanford lab. Jon has shared with me a lot of his practical know-hows, and has been a great companion as we take on various hardware and software tasks together. Steve helped me greatly with computing at Stanford and always promptly alerted me of any runtime issues in my scripts or webpages. I salute his vigilance.

Berkeley Matt Pyle, Bruno Serfass, Caleb Fink, Samuel Watkins

Matt, Caleb and Sam taught me everything I know about SuperCDMS data analysis and optimal filter. Matt's notes prompted me to view optimal filter in a more general probabilistic framework and eventually led to all my work in optimal filter theory. Matt's thesis and papers were essential for me to understand various nuanced aspects of the detector. Bruno has been instrumental to everything in SuperCDMS's DAQ and, along with Tsuguo, taught me everything about the DAQ and the data workflow in general.

HUJI Yonit Hochberg

Yonit is effectively my yet another adviser in all the theoretical aspects of my work. She has been my co-author in every single paper I participated. Aside from physics I have learned from her how to formulate a physics paper. During the COVID hiatus I would have been completely unproductive without her guidance.

Hamburg Belina von Krosigk

Belina became my role model as I started to straddle between the worlds of theory and experiment and get into more phenomenological work. I am especially grateful for the chance to work with her on the dark Compton paper.

UIUC/Fermilab Yonathan Kahn

Yoni is perhaps the smartest physicist I have met during my PhD years. I am lucky to have had the chance to collaborate with him and learn from his approach of gaining great physical insights by leveraging simple, yet very clever arguments.

UMN Matt Fritts, Nicholas Mast

Matt and Nick has inspired and helped refined many of my ideas in position reconstruction and machine learning in general. Nick also gave me the opportunity to chair the machine learning effort

in SuperCDMS, for which I am deeply grateful.

I would also like to thank the staff members at SLAC and Stanford Physics Department, especially Maria Frank, Martha Siegel, and Nick Swan. I am extremely bad at paperwork and forms and following deadlines but they have been extraordinarily patient and helpful. For one year I also had the pleasure to serve as the president of Hong Kong Student Association through which I have made many close friends both at Stanford and across the entire bay area. I shall refrain from putting all their names here as the list would be very, very long. If one of them is reading this, thank you for your friendship and the time we have spent together.

Last but not least, I would not have survived these years without the financial, physical and emotional support from my family, especially my mother. I would have collapsed in more than one way without her fervent and heroic support in all non-academic aspects of my life - thanks Mom.

In memory of my father.

E dolore fortitudo

Contents

Abstract	iv
Acknowledgements	v
1 Introduction	1
1.1 WIMP Dark Matter	1
1.2 Light Dark Matter	3
1.3 Looking for Light Dark Matter	3
2 DM Interaction with Matter	6
2.1 Fermi's Golden Rule	6
2.2 Lattice System	9
2.2.1 Elastic Nuclear Recoil	10
2.2.2 Phonon Production	12
2.2.3 Stable Defect Formation	17
2.2.4 Crowdion	18
2.3 Electron System	19
2.3.1 Bloch Wavefunctions	19
2.3.2 Electron Transition	20
2.3.3 Nearly Free Electron Model	21
2.3.4 Dielectric Formulation	23
2.3.5 Optical Interactions	25
2.4 Mixed Channels	31
2.4.1 Phonon-Assisted Electron Transition	32
2.4.2 Inelastic Nuclear Recoil (Bremsstrahlung)	32
2.4.3 Migdal Effect	33

3 Detector Response	34
3.1 Lindhard Model	34
3.2 Electron Recoil Ionization Yield	36
3.3 Neganov-Trofimov-Luke Effect	37
3.4 Phonon Transport	38
3.4.1 Callaway Model	39
3.4.2 Interface Matching	41
3.4.3 Phonon Collection Efficiency	46
3.5 Sensor Physics	47
3.5.1 Calorimetry	47
3.5.2 Electrothermal Feedback	52
3.5.3 Transition Edge Sensor (TES)	54
3.5.4 Quasiparticle-Assisted TES (QET)	56
4 Optimal Substrates for Direct Detection	59
4.1 Carbon-Based Material	59
4.2 Heavy Fermion Material	63
5 Future Research	70
A Density Functional Theory	72
A.1 Hartree-Fock Method	73
A.2 Hohenberg-Kohn Theorems	74
A.3 Example Calculation with Quantum ESPRESSO	76
A.4 Additional Corrections to DFT	77
B Signal Theory and Optimal Filter	80
B.1 Maximum-Likelihood Estimation	81
B.2 Cramér-Rao Lower Bound	82
B.3 Translation Invariant Fourier Transform	84
B.4 Stationarity and Cyclostationarity	85
B.5 Templateless Optimal Filter	88
C Event Reconstruction with Machine Learning	90
C.1 Deep Convolutional Network	90
C.2 Neural Ordinary Differential Equations	92

List of Tables

3.1 Phonon transmission probabilities for phonons in different substrates (top row) crossing into various materials. The probability n_l (n_t) is the probability for a longitudinal (transverse) phonon incident on the interface from the substrate to get into a region made of another material (leftmost column). \bar{n} is the probability averaged by the density of states of the two modes. Note that the probability is not symmetric between two materials, e.g. the probability for a phonon in silicon crossing into germanium (0.84) is very different from that for a phonon in germanium crossing into silicon (0.39).	44
4.1 <i>First and second sections:</i> material properties of diamond, Si, and Ge (from Refs. [82, 130, 80] unless otherwise stated). <i>Last section:</i> Phonon figures of merit in the three materials at low temperatures ($\lesssim 30\text{mK}$) for a mm-scale crystal. Transmission probabilities \bar{n} from substrate to tungsten (W) and aluminium (Al) are calculated from acoustic mismatch model in chapter 3.	60
4.2 Bulk material properties of diamond, Si, and the SiC polymorphs considered in this work (measurements taken from Refs. [82, 100, 127, 27, 64, 137] unless otherwise stated). $\epsilon_{0,\infty\perp}$ ($\epsilon_{0,\infty\parallel}$) refer to relative permittivity perpendicular (parallel) to the crystal c-axis at low and high frequency, with values from [92]. Optical phonon energies and high-frequency permittivity are taken from [125]. E_{eh} values denoted by † are estimated using equation 3.7. Defect creation energies are from [98, 115, 21]. Due to the differing commercial availability/utility of different polytypes, more commonly used crystal polytypes are better characterized than less common ones, and thus for the least well-studied polytypes (2H, 8H, 15R) many experimentally determined values are unavailable. Quantities denoted as [calc] were calculated to fill in some of the holes in the literature.	62

List of Figures

1.1	DM abundance can be explained by thermal freeze-out relic assuming the existence of some pair annihilation process that allows DM particles (χ) and SM particles (f) to convert into each other, mediated by some boson V	2
1.2	Maximum elastic nuclear recoil in silicon, germanium, carbon and helium for varying DM masses. The dashed line indicates a detector threshold.	5
2.1	Differential rate spectra for two different DM masses: 100 MeV (left) and 1 GeV (right). The dashed line indicates a detector threshold at 1 eV.	13
2.2	Figure taken from [85]. (blue) Kinematically allowed regions for DM scattering (c.f. equation 1.5) are shown for $m_\chi = 10$ keV, 1 MeV, and 100 MeV. (yellow) Kinematic region detectable via nuclear recoil and multiphonon production. (purple & green) Kinematic region detectable via single phonon production given by phonon dispersion.	16
2.3	(left) Energy collected E_C as a function of energy deposited ω by the initial scattering event for a simple hard-threshold defect model. As long as ω goes beyond E_D we lost an amount of energy equal to E_D to defect formation which leads to a drop in E_C . (right) The event rate (eq. 2.52) under this defect model. Blue is the original spectrum without any defect formation and green is the modified observed spectrum with $E_D=10$ eV.	17
2.4	(left) An illustration of replacement collision sequence in alkali halide taken from [123]. The direction of the recoil velocity progressively aligns to the [100] direction. In this case the charges on the ions facilitates the formation of an RCS. (right) Formation of crowdion from an RCS. A crowdion is a linear interstitial defect that propagates along one of the axis of symmetry in the lattice. Crowdions can travel faster than the speed of sound in the material.	18

2.5	Accessible phase space of the scattering process bounded by equation 2.72 (blue solid) and equation 2.73 (black solid). The available phase space can be enlarged by having higher effective masses (blue dashed), as well as a lower band gap (blue dotted). The maxima of the black line is at $q = m_\chi(v_{\text{esc}} + v_E)$ while the minima of the blue line is at $q = k_g$	23
2.6	Figure taken from [85]. (left) Structure factor for a free electron gas with $\omega_p = 15$ eV, $k_F = 3.3$ keV, and taking the $\Gamma_p \rightarrow 0$ limit of equation 2.82. The plasmon resonance shows up as an infinitely narrow resonance indicated by the dotted line, while the rest of the support is interpreted as electron-hole excitations. (right) Structure factor for silicon based on the calculation in [95]. In both panels, the dashed line indicates $q = \omega v_{\text{max}}$ where v_{max} is the maximum DM speed on Earth, such that the kinematically-accessible region is below and to the right of the dashed line. As can be seen, the plasmon peaks of the structure factor are not accessible for our DM halo.	25
2.7	Figure taken from [61]. Projected reach at 95% C.L. for absorption of kinetically mixed dark photons (left) and axion-like particles (right). The expected reach assumes a kg-year exposure for all materials. Shaded regions represents parameter space excluded by various experimental and observational constraints. The allowed QCD axion region is colored in shaded gray in the right plot.	28
2.8	Tree-level Feynman diagrams illustrating the Compton-like process where a dark matter boson is converted to a photon via electron scattering.	28
2.9	Projected 90% C.L. reach for relic dark photons (left) and axion-like particles (right) with a 1 kg-year exposure and no background. The reach for absorption (dashed lines) and Compton-like processes (thin solid lines) is indicated along with the combined reach (thick solid lines), showing substantially improved capabilities at higher DM masses when dark Compton scattering begins to dominate over absorption. The vertical dotted line indicates the mass of the electron.	31
2.10	Feynman diagram for the inelastic nuclear recoil. The additional photon vertex adds a factor of α to the cross-section.	32
3.1	Ionization yield of Silicon and Germanium fitted against the modified Lindhard model described in [149]. The red curve is a separate phenomenological model proposed by SuperCDMS in [7].	36
3.2	Plots of the quantum yield ϵ_{eh} (left) and Fano factor F (right) taken from [144]. The various fits are generated from phenomenological model based on a one-parameter Beta distribution parameterized by α . For more details refer to [144].	37

3.3	An incident longitudinal (L) acoustic wave is both reflected and refracted into longitudinal and transverse (SV) modes in the two media. The various angles here satisfy geometric-optical relations such as law of reflection and Snell's law. Reproduced from [87].	42
3.4	Model of a simple calorimeter. Any energy deposit will result in an exponential pulse will decay time $\tau = C/G$	48
3.5	Figure taken from [110]. Electrothermal feedback in microcalorimeter can cause energy pulses to be significantly shorter than typical timescale of thermal fluctuation in the sensor. Thus with sufficient bandwidth the energy resolution of the microcalorimeter is not limited by the thermal fluctuation noise.	50
3.6	Power spectrum of the signal and TFN for a simple thermal detector. The TFN and the signal are in different units. Note that they have the same shape and thus the energy resolution is only constrained by bandwidth-limiting noise, such as the thermometer white noise (dotted) illustrated here.	51
3.7	Figure taken from [110]. Typical TES circuit including bias resistance R_b , shunt resistance R_s and the readout inductance L (usually coupled to a SQUID amplifier). The shunt resistance is usually chose to be small compared to the operating resistance of the TES to ensure that the TES is operating in the voltage-biased regime.	55
3.8	Figure taken from [168]. Current flowing through the TES due to the voltage bias keeps the electrons at an elevated temperature T_e that is different from the phonon temperature. The bias thermal power flows through the electron-phonon thermal conductance R_{ep} into the phonon system and then through the Kapitza resistance R_K between the sensor and the substrate into the substrate which acts as the thermal bath.	56
3.9	Illustration of a SuperCDMS QET. (top) Phonons entering the fin will generate quasi-particles that gets trapped in the lower energy-gap region created by the tungsten TES. Their energy gets converted back into phonons in the TES upon recombination. This effectively increases the phonon collection area, while maintaining a small active TES volume. (bottom) The variation of the energy gap across the junction. When the quasiparticle travels from a high gap (high T_c) material to a low gap (low T_c) material it loses energy and gets trapped in the low gap region.	58
3.10	Quasi-particle trap rate as a function of energy gap ratio of the two regions. See [146] for details.	58

4.1	Figure taken from [102]. Nuclear recoil projected reach at 95% C.L. for He (blue), Diamond (green), Si (red), and Xe (cyan) for energy thresholds of 1 eV (top) and 10 meV (bottom). The dashed lines are for a g-day exposure, while the dot-dashed lines are for a kg-year exposure. The yellow region indicates the neutrino floor for He [65], and the brown region the neutrino floor for C (computed according to the formalism in Ref. [28]). Also shown in grey are the current best limits on NR dark matter interactions from ν CLEUS [13], CRESST-III [38, 5], CDMSLite [156], Darkside-50 [158], and Xenon-1T [14] for comparison.	65
4.2	(top) Crystal structures of the polytypes of SiC considered in [61]. Si atoms are blue and C atoms are brown. (bottom) Phonon band structures calculated from first principles. For details of calculations, see [61].	66
4.3	Reach and daily modulation for DM interactions mediated by a scalar coupling to nucleons, assuming a massive mediator (top) and massless mediator (bottom). (left) Reach curves assuming kg-year exposure and zero background. For single phonon excitations relevant for $m_\chi \lesssim 10$ MeV, we show two representative thresholds of 1 meV (solid lines) and 80 meV (dotted) for the different SiC polytypes. We also show the reach for a superfluid He target [97]. The dashed lines show sensitivity to nuclear recoils assuming threshold of 0.5 eV. In the shaded region, it is expected that the dominant DM scattering is via multiphonons [34, 160]. (right) The daily modulation of the DM-phonon scattering rate as a function of DM mass, where the quantity shown corresponds exactly to the modulation amplitude for a purely harmonic oscillation. The modulation is much smaller for scattering into acoustic phonons $\omega > 1$ meV, so we only show scattering into optical phonons with $\omega > 80$ meV. The modulation amplitude is generally largest for 2H and smallest for 3C. The inset compares the phase of the modulation among the polymorphs for $m_\chi = 80$ keV.	67
4.4	(left) Hybridization between the conduction band (dotted) and d/f-orbital (dashed) results in two hybridized bands (solid) with a small band gap and large effective mass indicated by the flatness of the band minimum. (right) Projected 95% C.L reach of a 1 kg-yr exposure target for FeSi (blue), silicon (green) and diamond (red). The reach curves end due to the bandgap of the respective materials. FeSi ($E_g = 0.18$ eV) not only has the lowest mass reach but also more sensitivity to $\bar{\sigma}_e$ across the whole DM mass region.	68

- 4.5 Figures taken from [68]. (left) Schematic depiction of the relevant kinematics for sub-GeV DM scattering. The shaded purple parabolas represent the kinematically-allowed region of q and ω for the labelled DM masses. The blue and orange shaded regions represent the support of the plasmon peak of the ELF for typical materials and URu_2Si_2 . The tail extends into the DM region for materials such as Al and Si, while for heavy-fermion materials such as URu_2Si_2 , the plasmon peak lies within the accessible kinematic region. The range of support for the FEG ELF (equation 2.82) is shown in shaded gray, and can be used to approximate the rate in both superconductors and semiconductors over a limited range of ω . The dot-dashed vertical line indicates the size of the Brillouin zone ($q \approx 2.3$ keV) of Si, while the horizontal dashed line indicates the band gap above which electron scattering can produce ionization. (right) Projected 95% C.L reach of a 1 kg-yr exposure target of Al (orange), Si (purple), a Dirac material (red) and URu_2Si_2 (green), computed for a light mediator. The Dirac material is computed with density 10 g/cm^3 , gap $2\Delta = 20 \text{ meV}$, Fermi velocity $v_F = 4 \times 10^{-4}c$, background dielectric constant $\kappa = 40$, and Dirac band cutoff $\omega_{\max} = 0.5 \text{ eV}$. URu_2Si_2 has an effective mass of $m^* \simeq 6m_e$, $v_F \simeq 6.5 \times 10^{-5}c$, $\omega_p \simeq 6.5 \text{ meV}$ and a bandgap of $E_g \simeq 5 \text{ meV}$ [20]. 69
- A.1 By lumping together the nucleus and core electrons in the atoms, the resultant potential leads to a smoother wavefunction (hence fewer basis components are needed), and fewer degrees of freedom as we have dropped the core electrons from our wavefunction. 78
- A.2 Figure taken from [173]. Optical absorption coefficient of silicon at room temperature from experimental measurements (gray), DFT calculation with nuclei at their nominal positions (blue), and DFT calculation with nuclei displaced from their nominal positions according to the one-shot recipe (red). We can see that the one-shot method reproduces experimental measured values perfectly by including the contribution from phonons which is significant at sub-gap energies. 79
- B.1 (top) An example of chirp noise and the corresponding covariance matrix in the frequency domain. The chirp noise which is cyclostationary introduces plenty of non-diagonal entries in the covariance matrix. (bottom) An example of pure white noise and the corresponding covariance matrix in the frequency domain. The stationary white noise has only diagonal elements in its covariance matrix. In fact it is approximately an identity matrix. The covariance matrix is well-defined in both cases and thus OF is optimal regardless of whether the noise is stationary or cyclostationary. 87
- C.1 Channel map of the SuperCDMS HV detector. Shown colored are the 12 TES channels. 91

Chapter 1

Introduction

At the beginning of the the last century Lord Kelvin identified two problems which he referred to as “clouds” over the field of physics. The clearing of these clouds eventually led to fundamental revolutions in modern physics. Today we are facing a similar situation in particles physics, wherein the nature of dark matter and the mass of neutrino constitutes two of the most acute challenges to the established Standard Model of particle physics. Their resolution will without doubt lead to new and revolutionary insights.

I shall not delve too much into the history of the discovery of dark matter. Interested readers are referred to [25, 26, 148]. Suffice to say these days most of the community believes that it is made up of some yet undiscovered new particles. So far the only interaction we have observed between dark matter (DM) and ordinary matter (SM) is that of gravity. If gravity were the only interaction between DM and SM, however, we would have to accept the fact that the current relic abundance of dark matter (82% of all matter [6]) is a mere coincidence, which many physicists including myself find unsatisfactory. As such many have proposed that there are additional coupling between DM and SM, which can then be utilized to explain the current relic density of dark matter via early universe thermodynamics.

1.1 WIMP Dark Matter

The first such proposal is that DM is made up of weakly-interacting massive particles (WIMP). In this model the initial population of DM particles produced during the hot, early phase of Big Bang reduces in number as the temperature of the universe cools below the mass of the WIMP. The decline in number density is driven by a pair-annihilation process (figure 1.1) which eventually freezes out due to the expansion of the universe. The relic density can be expressed in terms of the

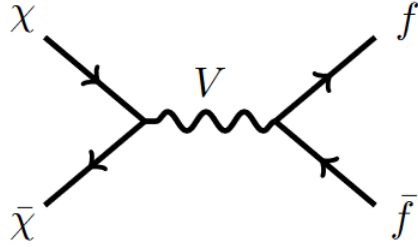


Figure 1.1: DM abundance can be explained by thermal freeze-out relic assuming the existence of some pair annihilation process that allows DM particles (χ) and SM particles (f) to convert into each other, mediated by some boson V .

cross-section of this annihilation process [109]:

$$\Omega h \approx 0.1 \times \left(\frac{10^{-9} \text{GeV}^{-2}}{\langle \sigma v \rangle} \right) \quad (1.1)$$

If we assume that the annihilation proceeds via weak interaction, in the non-relativistic limit the annihilation cross-section is roughly given by [109]

$$\langle \sigma v \rangle_{\text{WIMP}} \sim (G_F m)^2 \sim 10^{-10} \left(\frac{m}{\text{GeV}} \right)^2 \text{GeV}^{-2} \quad (1.2)$$

Combining equations 1.1 and 1.2, we can see that WIMP would produce the observed amount of relic dark matter ($\Omega h \sim 0.1$ [6]) if the mass of the WIMP is around GeV scale. A more thorough calculation shows that WIMP can reproduce the correct observed DM relic abundance as long as the mass of the WIMP is larger than about 2 GeV, which is referred to as the Lee-Weinberg bound [106].

An important implication of this model is that we are expected to be able to detect this interaction directly with some form of rare event detector similar to how we detect neutrinos. This has prompted decades-long experimental efforts to detect dark matter directly [151, 162, 109, 39], which so far have not been successful in finding dark matter. In light of these negative results, there has been a paradigm shift in recent years to diversify away from WIMP and to consider alternative dark matter models that circumvent the Lee-Weinberg bound and goes into the low-mass region of sub-GeV masses [18, 139, 76]. These models are broadly referred to as light dark matter (LDM) and will be the main focus of this thesis.

1.2 Light Dark Matter

To see how we can circumvent the Lee-Weinberg bound, let us take another look at eq 1.2:

$$\langle\sigma v\rangle_{\text{WIMP}} \sim (G_F m)^2 \quad (1.3)$$

If we do not limit ourselves to weak-interaction the coupling constant can in principle be anything we want. One possibility is that DM particles actually interact much more strongly among themselves while still interacting very weakly with SM particles. In that scenario the effective coupling for the pair annihilation could be larger than the Fermi constant and hence the mass of the DM particle can be much lower. This class of models has become widely-popular and generally requires introduction of a new light boson (fifth force) to act as a portal between the otherwise decoupled DM sector and SM sector [76].

The introduction of fifth force is also motivated by various other anomalies we have observed in particle physics that are not directly related to dark matter, such as the muon g-2 anomaly [90, 107, 24]. Therefore this class of models has the potential to kill many birds with one stone.

Apart from experimental and observational motivations, there is also a perhaps more direct theoretical argument for light dark matter from the quantization of gravity. Calmet et al. [32, 33] showed that starting from general relativity and integrating out fluctuations of gravitons we obtain an effective action from which we can then derive the poles of the Green's function. Interestingly they found that aside from the usual massless pole corresponding to the graviton, there are additional spin-0 and spin-2 massive degrees of freedom. They also produced a bound on the masses of these additional particles:

$$10^{-12} \text{ GeV} < M_0, M_2 < 0.16 \text{ GeV} \quad (1.4)$$

Once again we see that this seems to suggests the existence of new light boson.

1.3 Looking for Light Dark Matter

Let us consider the general kinematics of dark matter detection. The energy ω deposited by the dark matter in the detector via scattering is related to the momentum transfer \mathbf{q} via

$$\omega = \frac{1}{2} m_\chi v_\chi^2 - \frac{(m\mathbf{v} - \mathbf{q})^2}{2m_\chi^2} = \mathbf{q} \cdot \mathbf{v} - \frac{q^2}{2m_\chi} \quad (1.5)$$

where $v_\chi \sim 10^{-3}c$ is the speed of halo DM which is also equal to the speed of Earth relative to the galactic rest frame ¹.

For the simple case of elastic two-body scattering against a target particle of mass m initially at rest, the conservation laws give

$$\mathbf{q} \cdot \mathbf{v} = \frac{q^2}{2\mu}, \omega_{\max} = \frac{2\mu^2 v_\chi^2}{m} \quad (1.6)$$

where μ is the reduced mass of the DM and the target particle. If m_χ is small compared to m then $\mu \approx m_\chi$. Thus we will get a larger energy deposit ω_{\max} for if the mass of our target is lighter.

We can interpret this relation in another way. Suppose our detector has a detection threshold E_{th} which is the minimal amount of energy we can detect, then the lightest DM mass we can detect is given by

$$m_{\chi,\min} = \sqrt{E_{\text{th}} \frac{m}{2v_\chi^2}} = 100 \text{ MeV} \times \left(\frac{E_{\text{th}}}{1 \text{ eV}} \frac{m}{20 \text{ GeV}} \right)^{1/2} \quad (1.7)$$

Therefore for a fixed threshold a lighter m will allow us to probe a lighter DM mass m_χ .

The argument above is summarized in figure 1.2, we plot the maximum energy transfer (via elastic nuclear recoil) against DM mass for 4 different materials. Any energy transfer below E_{th} is invisible to our detector. As can be seen for a fixed detector threshold we will need lighter target mass to probe lighter DM mass.

For DM masses below around 100 MeV even the lightest nuclei might be too heavy and we can instead consider using electrons as our scattering targets. In various condensed matter systems there are even lighter excitations (for example optical phonons in solids) that can act as targets to detect even lower DM masses. The richness of excitations in solid state materials combined with their relative ease of handling compared to gas or liquid makes them extremely potent for DM direct detection. For a long time only a small subset of solid-state materials has been used as substrates for DM detection. This has started to change in recent years as the community began to develop a more systematic understanding of the relevant solid state physics and explore beyond familiar types of materials.

This thesis aims to provide a summary of these new developments, especially the ones which I have contributed to directly. We will begin with a survey of the solid state physics relevant to generating the primary interaction with DM (Chapter 2). Then we will discuss how the energy from the primary interaction gets propagated and collected into our sensor (Chapter 3). Finally we will discuss substrate optimization with respect to both the rate of primary interaction as well

¹It has been discovered recently that a significant fraction of DM in our galaxy is out of equilibrium and travelling at a higher speed than what is expected from the Standard Halo Model. See [128, 129].

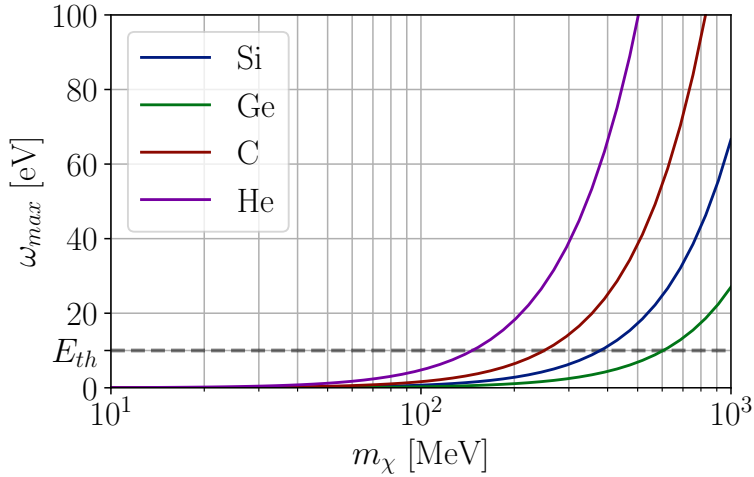


Figure 1.2: Maximum elastic nuclear recoil in silicon, germanium, carbon and helium for varying DM masses. The dashed line indicates a detector threshold.

as the collection efficiency (Chapter 4). Chapter 5 will be a discussion on future directions and research problems that remains to be solved.

Although this thesis is mostly about material optimization, during my PhD years I have also made various original contributions in the area of signal processing and machine learning applied to pulse and event reconstruction. These contributions are discussed in the Appendices in order to avoid interfering with the main thread of the thesis. However they carry as much weight as the main part of the thesis.

Chapter 2

DM Interaction with Matter

In this chapter we will go over the relevant condensed matter physics for detection of dark matter particles. We will be focusing on crystalline solids. Broadly speaking there are two systems to which the dark matter particles can deposit their energies - the lattice system made up of the atomic nuclei, and the electron system. Within each system there are various interaction channels via which the energy can go depending on the kinematics. For example in the lattice system the dark matter can produce phonons directly for low momentum transfer while for high momentum transfer a displaced nucleus may be the result. Some interaction channels may even simultaneously deposit energy in both the lattice and electron systems.

We will go over the physics for each interaction channel. The main tool for us to connect the theory (Hamiltonian of the interaction) to experiment (measured event rate) is Fermi's Golden Rule, which is the focus of the next section.

2.1 Fermi's Golden Rule

Consider an incoming dark matter particle with momentum \mathbf{p}_χ and energy E_χ being scattered by our substrate which is initially in some ground state $|0\rangle$ with energy E_0 . After the scattering, our substrate is now in a new final state $|f\rangle$ with energy E_f and the outgoing dark matter particle now has momentum \mathbf{p}'_χ and energy E'_χ . From perturbation theory the probability of such a scattering event occurring per unit time $\Gamma_{i\mathbf{p}_\chi \rightarrow f\mathbf{p}'_\chi}$ is given by Fermi's golden rule:

$$\Gamma_{0,\mathbf{p}_\chi \rightarrow f,\mathbf{p}'_\chi} = |\langle f, \mathbf{p}'_\chi | H_{\chi T} | 0, \mathbf{p}_\chi \rangle|^2 2\pi \delta(E_f + E'_\chi - E_0 - E_\chi) \quad (2.1)$$

where $H_{\chi T}$ is the perturbing Hamiltonian that describes the coupling between dark matter and

ordinary matter.

For most of our purposes we are interested in the total event rate regardless of the specific final states, thus we can sum and integrate over the phase space of all final states.

$$\Gamma_{0,\mathbf{p}_\chi} = \int \frac{V d^3 \mathbf{p}'_\chi}{(2\pi)^3} \sum_f \Gamma_{0,\mathbf{p}_\chi \rightarrow f, \mathbf{p}'_f} \quad (2.2)$$

$$= \int \frac{V d^3 \mathbf{p}'_\chi}{(2\pi)^3} \sum_f |\langle f, \mathbf{p}'_\chi | H_{\chi T} | 0, \mathbf{p}_\chi \rangle|^2 2\pi \delta(E_f + E'_\chi - E_0 - E_\chi) \quad (2.3)$$

The volume V comes from integrating over all positions this scattering can happen which is simply equal to the volume of the substrate.

Next we integrate over the distribution of dark matter initial momentum and energy which can be modelled by some velocity distribution $f(\mathbf{v})$:

$$\Gamma = \int d^3 \mathbf{v} f(\mathbf{v}) \Gamma_{0,\mathbf{p}_\chi} \quad (2.4)$$

$$= \int d^3 \mathbf{v} f(\mathbf{v}) \frac{V d^3 \mathbf{p}'_\chi}{(2\pi)^3} \sum_f |\langle f, \mathbf{p}'_\chi | H_{\chi T} | 0, \mathbf{p}_\chi \rangle|^2 2\pi \delta(E_f + E'_\chi - E_0 - E_\chi) \quad (2.5)$$

This equation gives the event rate per unit time per dark matter particle. In experiments we are interested in the total event rate per unit substrate mass. Thus we need to multiply by the total number of dark matter particles within our detector, which is given by $n_\chi = \rho_\chi V / m_\chi$ and then divide by the total mass of the substrate $\rho_T V$:

$$R = \frac{1}{\rho_T V} \frac{\rho_\chi V}{m_\chi} \Gamma \quad (2.6)$$

$$= \frac{1}{\rho_T} \frac{\rho_\chi}{m_\chi} \int d^3 \mathbf{v} f_\chi(\mathbf{v}) \frac{V d^3 \mathbf{p}'_\chi}{(2\pi)^3} \sum_f |\langle f, \mathbf{p}'_\chi | H_{\chi T} | 0, \mathbf{p}_\chi \rangle|^2 2\pi \delta(E_f + E'_\chi - E_0 - E_\chi) \quad (2.7)$$

where ρ_χ and m_χ are the local dark matter mass density and mass of the dark matter particle and ρ_T is the mass density of the substrate. R has the unit of Hz/kg.

We shall limit ourselves to velocity-independent interactions [53]. The Hamiltonian can be

written as a sum of potential between the DM and each target in the substrate:

$$H_{\chi T}(\mathbf{r}) = \sum_i \Phi(\mathbf{r}_\chi - \mathbf{r}_i) \quad (2.8)$$

$$= \sum_i \int \frac{d^3\mathbf{q}}{(2\pi)^3} e^{i\mathbf{q}\cdot(\mathbf{r}_\chi - \mathbf{r}_i)} \Phi(\mathbf{q}) \quad (2.9)$$

$$= \int \frac{d^3\mathbf{q}}{(2\pi)^3} e^{i\mathbf{q}\cdot\mathbf{r}_\chi} \Phi(\mathbf{q}) \left(\sum_i e^{i\mathbf{q}\cdot\mathbf{r}_i} \right) \quad (2.10)$$

All the target dependence is contained within the operator $\mathcal{O}_T = \sum_i e^{i\mathbf{q}\cdot\mathbf{r}_i}$ inside the bracket. The incoming and outgoing DM states are plane waves (e.g. $\langle \mathbf{r}_\chi | \mathbf{p}_\chi \rangle = e^{i\mathbf{p}_\chi \cdot \mathbf{r}_\chi} / \sqrt{V}$), thus

$$\langle f, \mathbf{p}'_\chi | H_{\chi T} | 0, \mathbf{p}_\chi \rangle = \int d^3\mathbf{r}_\chi \int \frac{d^3\mathbf{q}}{V(2\pi)^3} e^{i(\mathbf{q} + \mathbf{p} - \mathbf{p}') \cdot \mathbf{r}_\chi} \Phi(\mathbf{q}) \langle f | \mathcal{O}_T | 0 \rangle \quad (2.11)$$

$$= \frac{1}{V} \Phi(\mathbf{q}) \langle f | \mathcal{O}_T | 0 \rangle \quad (2.12)$$

where \mathcal{O}_T is the target-dependent part of the interaction Hamiltonian. By convention we usually rewrite $\Phi(\mathbf{q})$ as

$$\Phi(\mathbf{q}) = \sqrt{\frac{\pi\bar{\sigma}}{\mu_\chi^2}} F_\chi(\mathbf{q}) \quad (2.13)$$

The interaction strength $\bar{\sigma}$ has unit of cross-section and μ_χ is the reduced mass of the DM particle with scattering target. The interaction form factor $F_\chi(\mathbf{q})$ is unit-less and carries all the momentum dependence. For a Coulomb-like interaction mediated by a mediator particle with mass m_A , we have [152, 136]

$$F_\chi(q) = \frac{q_0^2}{q^2 + m_A^2}$$

where q_0 is some characteristic momentum that we choose to normalize our form factor. A different normalization is just equivalent to a different convention for the interaction strength. In this thesis, we almost exclusively focus on interaction form factor of this form.

We can also factorize the delta function by introducing the energy transfer ω and integrating over it:

$$\delta(E_f + E'_\chi - E_0 - E_\chi) = \int d\omega \delta(E_f - E_0 - \omega) \delta(\omega - E_\chi + E'_\chi) \quad (2.14)$$

Putting everything together, the rate per substrate mass now becomes

$$R = \frac{1}{\rho_T m_\chi} \int d^3\mathbf{v} f_\chi(\mathbf{v}) \int \frac{d^3\mathbf{q}}{(2\pi)^3} d\omega \delta(\omega - E_\chi + E'_\chi) \frac{\pi\bar{\sigma}}{\mu_\chi^2} |F_\chi(q)|^2 \left(\frac{2\pi}{V} \sum_f |\langle f | \mathcal{O}_T | 0 \rangle|^2 \delta(E_f - E_0 - \omega) \right) \quad (2.15)$$

The quantity in the bracket contains all the relevant information about substrate and is called the structure factor $S(\mathbf{q}, \omega)$:

$$S(\mathbf{q}, \omega) = \frac{2\pi}{V} \sum_f |\langle f | \mathcal{O}_T | 0 \rangle|^2 \delta(E_f - E_0 - \omega) \quad (2.16)$$

The other factors in equation 2.15 are inputs from astrophysics ($f(\mathbf{v})$) or DM theory ($F(\mathbf{q})$) which we have no control over when performing an experiment. However we can optimize the rate given these inputs by choosing the material with the optimal structure factor.

In the following sections we will calculate this structure factor for various interaction channels in our substrate.

2.2 Lattice System

First let us focus on the case of DM-nucleon scattering. If our substrate is just a single isolated atom and our DM particles scatters off its nucleus, then we can simply model the nucleus as a free particle and substitute the initial and final states by the initial and final states of our nucleus. This is essentially a two-body elastic scattering problem which is readily solvable. However in real materials, atoms bond with each other and create a lattice of interacting nuclei. Thus it is likely that scattering off one nucleus will simultaneously affect a neighbourhood of nearby nuclei. In this case the process becomes a many-body scattering.

Let us derive the condition that determines whether we can treat the process as two-body scattering versus many-body scattering. Since the nucleus is mostly at rest initially, the characteristic length scale of the interaction λ is set by the momentum of the incoming DM particle $q_\chi = m_\chi v_\chi$ via its de Broglie wavelength:

$$\lambda \sim \frac{1}{m_\chi v_\chi} \sim \left(\frac{1 \text{ GeV}}{m_\chi} \right) \left(\frac{10^{-3}}{v_\chi} \right) (0.1 \text{ nm})$$

If λ is significantly shorter than the lattice constant a of our material (i.e. the distance between adjacent nuclei) then treating the problem as a two-body process would be a good approximation. However if λ spans multiple lattice constants then we will need to combine the scattering effects from multiple nuclei. For typical materials $a \approx O(1\text{ nm})$, therefore for DM mass around and below 100 MeV, we have $\lambda \gtrsim a$ and we can no longer neglect many-body effects.

2.2.1 Elastic Nuclear Recoil

Let us first consider the case of elastic **nuclear recoil** (NR) where the scattering nucleus can be treated as a free body. The energy deposit ω must then be related to the momentum transfer q by

$$\omega = \frac{q^2}{2m_N}$$

Combining with equation 1.5 results in a minimum DM speed for this process to be possible:

$$\begin{aligned} \frac{q^2}{2m_N} &= \mathbf{q} \cdot \mathbf{v} - \frac{q^2}{2m_\chi} \\ |\mathbf{q}| |\mathbf{v}| \cos \theta &= \frac{q^2}{2\mu_{\chi N}} \\ v_{\min} &= \frac{q}{2\mu_{\chi N}} \end{aligned}$$

Now let us calculate the structure factor. The initial state and final states are simple plane waves with fixed momentum $|\mathbf{p}\rangle$. The target-dependent operator \mathcal{O}_T is simply given by $e^{i\mathbf{q} \cdot \mathbf{r}_N}$ which is just the momentum-shift operator. Therefore the structure factor (equation 2.16) is

$$S_{\text{single nucleus}}(\mathbf{q}, \omega) = \frac{2\pi}{V} \left(\sum_{\mathbf{p}_f} |\langle \mathbf{p}_f | e^{i\mathbf{q} \cdot \mathbf{r}_N} | 0 \rangle|^2 \right) \delta\left(\frac{q^2}{2m_N} - \omega\right) \quad (2.17)$$

$$= \frac{2\pi}{V} \left(\sum_{\mathbf{p}_f} |\langle \mathbf{p}_f | \mathbf{q} \rangle|^2 \right) \delta\left(\frac{q^2}{2m_N} - \omega\right) \quad (2.18)$$

$$= \frac{2\pi}{V} \delta\left(\frac{q^2}{2m_N} - \omega\right) \quad (2.19)$$

For a substrate with N nuclei in total we simply multiply this by N since we do not care which nucleus the DM particle scattered with, thus for a lattice of point-like nuclei we have

$$S_{\text{point NR}}(\mathbf{q}, \omega) = \frac{2\pi}{V} N \delta\left(\frac{q^2}{2m_N} - \omega\right) \quad (2.20)$$

In reality nuclei are not point particles but have internal degrees of freedom. If we instead

postulate that the contact potential is between the DM particle and the nucleons (protons and neutrons), we can sum over the nucleons labelled by α :

$$\mathcal{O}_T = \sum_{\alpha} e^{i\mathbf{q} \cdot (\mathbf{r}_N + \mathbf{r}_{\alpha})} \quad (2.21)$$

where \mathbf{r}_{α} denotes the position of the nucleons relative to the position of the entire nucleus. This leads to

$$S_{\text{NR}}(\mathbf{q}, \omega) = \frac{2\pi}{V} N A^2 |F_N(q)|^2 \delta\left(\frac{q^2}{2m_N} - \omega\right) \quad (2.22)$$

where A is the mass number and $F_N(q) = \langle N | \frac{1}{A} \sum_{\alpha} e^{i\mathbf{q} \cdot \mathbf{r}_{\alpha}} | N \rangle$ is the nuclear form factor. $|N\rangle$ describes the bound state of nucleons and contains all the internal degrees of freedom. The internal degrees of freedom are relevant when q is above 1-10 MeV. For sub-GeV DM particles we can approximately take $F_N(q) = 1$. The detailed modelling and computation of the nuclear form factor is not the focus of this thesis and we refer interested readers to [133, 73]. Furthermore the DM-nucleon interaction is not necessarily a contact interaction and we can introduce e.g. spin-dependent coupling which would make the above expression depend on additional spin degrees of freedom. For a survey of different types of possible operators for DM-nucleon coupling refer to [53, 150].

Combining the DM speed cutoff and the structure factor, we can write down the full integral for the total rate:

$$R = \frac{N}{\rho_T V} \frac{A^2 \bar{\sigma} \rho_{\chi}}{m_{\chi} \mu_{\chi}^2} \int \frac{d^3 \mathbf{q}}{4\pi} |F_{\chi}(q)|^2 |F_N(q)|^2 \int_{v_{\min} = \frac{q}{2\mu_{\chi}}}^{\infty} d^3 \mathbf{v} f_{\chi}(\mathbf{v}) \delta\left(\frac{q^2}{2m_N} - \omega(\mathbf{q}, \mathbf{v})\right) \quad (2.23)$$

$$= \frac{N}{\rho_T V} \frac{A^2 \bar{\sigma} \rho_{\chi}}{2m_{\chi} \mu_{\chi}^2} \iint q^2 dq d(\cos \theta) |F_{\chi}(q)|^2 |F_N(q)|^2 \int_{v_{\min}}^{\infty} d^3 \mathbf{v} f_{\chi}(\mathbf{v}) \delta\left(\frac{q^2}{2m_N} - \left(qv \cos \theta - \frac{q^2}{2m_{\chi}}\right)\right) \quad (2.24)$$

$$= \frac{N}{\rho_T V} \frac{A^2 \bar{\sigma} \rho_{\chi}}{2m_{\chi} \mu_{\chi}^2} \int q^2 dq |F_{\chi}(q)|^2 |F_N(q)|^2 \int_{v_{\min}}^{\infty} d^3 \mathbf{v} f_{\chi}(\mathbf{v}) \int d(\cos \theta) \delta\left(\frac{q^2}{2m_N} - \left(qv \cos \theta - \frac{q^2}{2m_{\chi}}\right)\right) \quad (2.25)$$

$$= \frac{N}{\rho_T V} \frac{A^2 \bar{\sigma} \rho_{\chi}}{2m_{\chi} \mu_{\chi}^2} \int q dq |F_{\chi}(q)|^2 |F_N(q)|^2 \left(\int_{v_{\min}}^{\infty} d^3 \mathbf{v} \frac{f_{\chi}(\mathbf{v})}{v} \right) \quad (2.26)$$

The quantity in the bracket in the last line is usually written as $\eta(v_{\min})$ and referred to as the **mean inverse speed**. For WIMP the mediator is assumed to be at weak-scale (100GeV) which is very heavy ($m_A \gg q$) and thus we can simply take $F_{\chi}(q) = 1$. We will also take $F_N = 1$ for

low-mass DM. Also note that $qdq = m_N d\omega$, therefore we have

$$\frac{dR}{d\omega} = \frac{A^2 \bar{\sigma} \rho_\chi}{2m_\chi \mu_\chi^2} \eta(v_{\min}) \quad (2.27)$$

Remember that the unit of R is event per unit time per unit substrate mass, thus $dR/d\omega$ has unit of event per unit time per substrate mass per unit nuclear recoil energy. This is called the **differential rate unit** (dru) for short.

What remains is to simply calculate the mean inverse speed η . We assume a simple truncated Maxwell-Boltzmann distribution for the DM velocity around Earth [49]:

$$f(\mathbf{v}) = \frac{1}{K} e^{-|\mathbf{v} + \mathbf{v}_E|^2/v_0^2} \Theta(v_{\text{esc}} - |\mathbf{v} + \mathbf{v}_E|) \quad (2.28)$$

where K is a normalization factor given by

$$K = v_0^3 \pi \left(\sqrt{\pi} \operatorname{erf} \left(\frac{v_{\text{esc}}}{v_0} \right) - \frac{2v_{\text{esc}}}{v_0} e^{-v_{\text{esc}}^2/v_0^2} \right) \quad (2.29)$$

and v_0 is the typical scale of DM velocity, \mathbf{v}_E is Earth's velocity in the galactic rest frame and v_{esc} is the galactic escape velocity.

Performing the integration over inverse speed gives [49]:

$$\eta = \begin{cases} \frac{\pi v_0^2}{2N_0} \left(\sqrt{\pi} \frac{v_0}{v_e} \left[\operatorname{erf} \left(\frac{v_{\min} + v_e}{v_0} \right) - \operatorname{erf} \left(\frac{v_{\min} - v_e}{v_0} \right) \right] - 4 \exp \left(-\frac{v_{\text{esc}}^2}{v_0^2} \right) \right) & , \text{if } v_{\min} < v_{\text{esc}} - v_e \\ \frac{\pi v_0^2}{2N_0} \left(\sqrt{\pi} \frac{v_0}{v_e} \left[\operatorname{erf} \left(\frac{v_{\text{esc}}}{v_0} \right) - \operatorname{erf} \left(\frac{v_{\min} - v_e}{v_0} \right) \right] - 2 \frac{v_{\text{esc}} - v_{\min} + v_e}{v_e} \exp \left(-\frac{v_{\text{esc}}^2}{v_0^2} \right) \right) & , \text{if } v_{\text{esc}} - v_e < v_{\min} < v_{\text{esc}} + v_e \\ 0 & , \text{otherwise} \end{cases} \quad (2.30)$$

In figure 2.1 we have plotted the recoil energy spectra for 4 different elements. For heavier DM masses we prefer heavier nuclei for the A^2 enhancement. For light DM however, unless our detector threshold can be reduced indefinitely, lighter nuclei will net us a higher total rate since their spectra extends to higher recoil energies. This is essentially just a restatement of the argument we presented in section 1.3.

2.2.2 Phonon Production

So far we have been assuming that our nucleus can be considered as a free particle. As the momentum transfer becomes softer this assumption would need to be relaxed. The next simplest

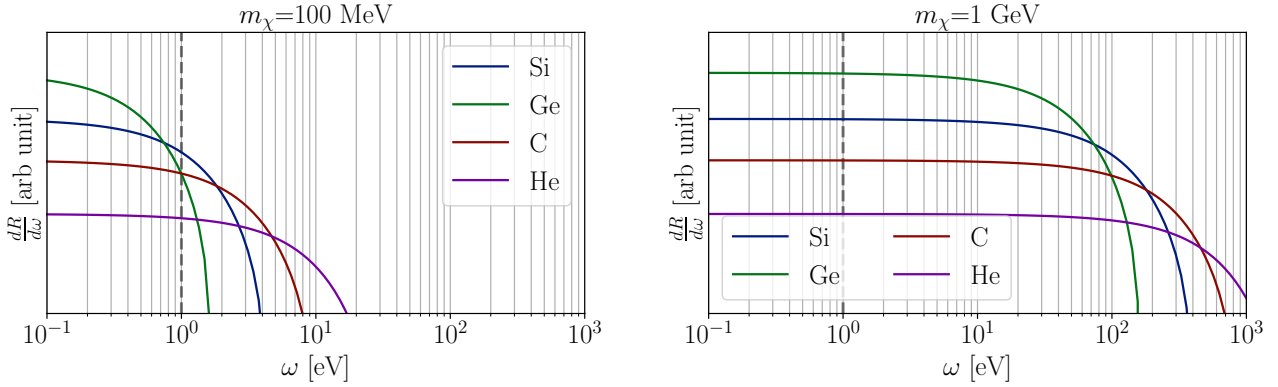


Figure 2.1: Differential rate spectra for two different DM masses: 100 MeV (left) and 1 GeV (right). The dashed line indicates a detector threshold at 1 eV.

model is of course that of a simple harmonic oscillator. In other words we evoke the “ball and spring” model and treat our nucleus as a simple harmonic oscillator around its equilibrium position (ground state). This was done in [96, 85] which we will reproduce in this section.

Mathematically this implies that instead of using plane waves as our initial and final states for our nucleus, we should replace them by harmonic oscillator eigenstates and calculate products of the form $\langle n | e^{i\mathbf{q} \cdot \mathbf{r}_N} | 0 \rangle$ which are matrix elements of the momentum shift operator. To this end we first solve the simple harmonic oscillator in momentum representation:

$$\frac{\mathbf{p}^2}{2m_N} - \frac{m_N\omega_0^2}{2}\nabla_{\mathbf{p}}^2\phi_n(\mathbf{p}) = E_n\phi_n(\mathbf{p}) \quad (2.31)$$

The solutions are separable $\phi_n(\mathbf{p}) = \phi_i(p_x)\phi_j(p_y)\phi_k(p_z)$ with $E_n = E_i + E_j + E_k$ and solutions for each component satisfy

$$\phi_n(p_i) = A_n \exp\left(-\frac{p_i^2}{2m_N\omega_0}\right) H_n\left(\frac{p_i}{\sqrt{m_N\omega_0}}\right) \quad (2.32)$$

where $A_n = \frac{(m_N\omega_0\pi)^{1/4}}{\sqrt{2^n n!}}$ and H_n is the n -th Hermite polynomial.

Thus the matrix elements that we want to calculate is given by [85]

$$\langle n_x, n_y, n_z | e^{i\mathbf{q} \cdot \mathbf{r}_N} | 0 \rangle = \int d^3\mathbf{p} \phi_n^*(\mathbf{p}) \phi_0(\mathbf{p} - \mathbf{q}) \quad (2.33)$$

$$= \int dp_x dp_y dp_z \phi_{n_x}^*(p_x) \phi_{n_y}^*(p_y) \phi_{n_z}^*(p_z) \phi_0(p_x - q_x) \phi_0(p_y - q_y) \phi_0(p_z - q_z) \quad (2.34)$$

$$= [2^n (n_x! n_y! n_z!)]^{-1/2} \exp\left(\frac{-q^2}{4m_N \omega_0}\right) \left(\frac{q}{\sqrt{m_N \omega_0}}\right)^n (\sin \theta \cos \phi)^{n_x} (\sin \theta \sin \phi)^{n_y} (\cos \theta)^{n_z} \quad (2.35)$$

Squaring and summing over all possible combinations of $n = n_x + n_y + n_z$ gives:

$$|\langle n | e^{i\mathbf{q} \cdot \mathbf{r}_N} | 0 \rangle|^2 = \sum_{n=n_x+n_y+n_z} \frac{1}{n_x! n_y! n_z!} \exp\left(\frac{-q^2}{q_0^2}\right) \left(\frac{q}{q_0}\right)^{2n} (\sin \theta \cos \phi)^{2n_x} (\sin \theta \sin \phi)^{2n_y} (\cos \theta)^{2n_z} \quad (2.36)$$

$$= \exp\left(\frac{-q^2}{q_0^2}\right) \left(\frac{q}{q_0}\right)^{2n} \frac{1}{n!} \sum_n \frac{n!}{n_x! n_y! n_z!} (\sin \theta \cos \phi)^{2n_x} (\sin \theta \sin \phi)^{2n_y} (\cos \theta)^{2n_z} \quad (2.37)$$

$$= \exp\left(\frac{-q^2}{q_0^2}\right) \left(\frac{q}{q_0}\right)^{2n} \frac{1}{n!} [(\sin \theta \cos \phi)^2 + (\sin \theta \sin \phi)^2 + (\cos \theta)^2]^n \quad (2.38)$$

$$= \exp\left(\frac{-q^2}{q_0^2}\right) \left(\frac{q}{q_0}\right)^{2n} \frac{1}{n!} \quad (2.39)$$

$$= P(n; (q/q_0)^2) \quad (2.40)$$

where $q_0 = \sqrt{2m_N \omega_0}$, and $P(x; \lambda)$ denotes the Poisson distribution function with mean λ . Thus we see that the structure factor is given by a Poisson distribution:

$$S_{\text{phonon}}(\mathbf{q}, \omega) = \frac{2\pi}{V} \sum_n P(n; (q/q_0)^2) \delta(n\omega_0 - \omega) \quad (2.41)$$

Following a similar calculation as in equation 2.26, we have

$$R = \frac{NA^2}{\rho_T V} \frac{\rho_\chi \bar{\sigma}}{2m_\chi \mu_\chi^2} \int q dq |F_\chi(q)|^2 \sum_n P(n; (q/q_0)^2) \eta(v_{\min}(n)) \quad (2.42)$$

where the minimum speed is given by

$$v_{\min}(n) = \frac{n\omega_0}{q} + \frac{q}{2m_\chi} \quad (2.43)$$

We can check that this reduces to equation 2.26 when $q \gg q_0$ (elastic limit). In this case the Poisson distribution is sharply peaked at $\bar{n} = (q/q_0)^2$ and thus all the probability is concentrated in the $n = \bar{n}$ term:

$$R = \frac{NA^2}{\rho_T V} \frac{\rho_\chi \bar{\sigma}}{2m_\chi \mu_\chi^2} \int q dq |F_\chi(q)|^2 \eta(v_{\min}(\bar{n})) \quad (2.44)$$

and

$$v_{\min}(\bar{n}) = \frac{q}{2m_N} + \frac{q}{2m_\chi} \quad (2.45)$$

$$= \frac{q}{2\mu_\chi} \quad (2.46)$$

which is exactly the same as what we had before.

In the $q \approx q_0$ regime, the standard deviation is of the same order as the mean thus we produce multiple phonons per event. This is called the multi-phonon regime and typically occurs at around $q \sim 10 - 100$ keV. In the low q limit single-phonon production ($n = 1$) dominates and the rate is suppressed by an additional factor of $e^{-(q/q_0)^2}$:

$$R \approx \frac{NA^2}{\rho_T V} \frac{\rho_\chi \bar{\sigma}}{2m_\chi \mu_\chi^2} \int q dq |F_\chi(q)|^2 e^{-(q/q_0)^2} \left(\frac{q}{q_0} \right)^2 \eta(v_{\min}) \quad (2.47)$$

$$v_{\min} = \frac{\omega_0}{q} + \frac{q}{2m_\chi} \quad (2.48)$$

In the single-phonon limit the simple harmonic oscillator model breaks down and we should consider the proper phonon dispersion. The structure factor is given by [85]

$$S_{\text{phonon}}(\mathbf{q}, \omega) = \frac{2\pi}{V} \sum_\nu \frac{|F_\nu(\mathbf{q})|^2}{\omega_{\nu, \mathbf{q}}} \delta(\omega_{\nu, \mathbf{q}} - \omega) \quad (2.49)$$

where $F_\nu(\mathbf{q})$ is the phonon form factor for the phonon mode labelled by ν and $\omega_{\nu, \mathbf{q}}$ is the corresponding energy dispersion. We shall not delve into the details of the phonon form factor. Interested reader should refer to [85]. Figure 2.2 summarizes the kinematics of various nuclear recoil regimes.

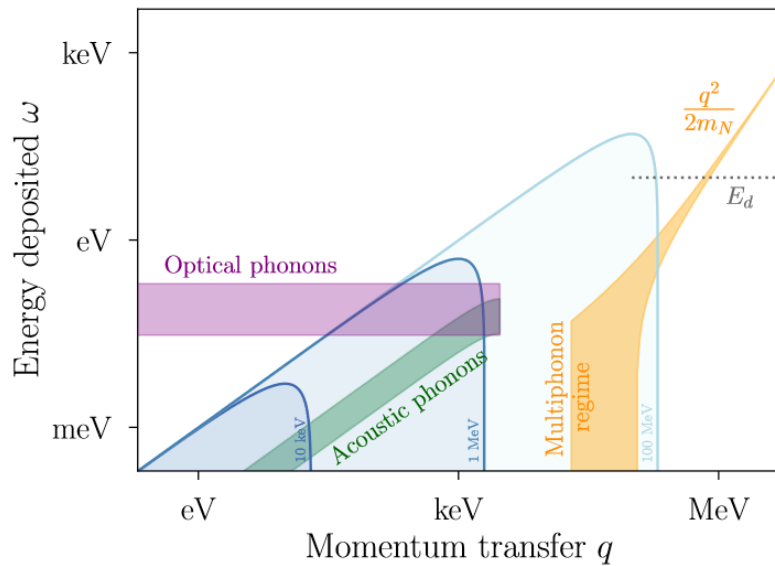


Figure 2.2: Figure taken from [85]. (blue) Kinematically allowed regions for DM scattering (c.f. equation 1.5) are shown for $m_\chi = 10 \text{ keV}$, 1 MeV , and 100 MeV . (yellow) Kinematic region detectable via nuclear recoil and multiphonon production. (purple & green) Kinematic region detectable via single phonon production given by phonon dispersion.

2.2.3 Stable Defect Formation

Scattering events of sufficiently high energy can lead to formation of stable defects that are long-lived at cryogenic temperatures as defect relaxation time generally follows an Arrhenius trend [22, 114, 117, 166, 55]. This leads to some interesting consequences as well as alternative experimental techniques.

Stable long-lived defects formed by scattering can store a certain amount of “lost” energy that is not collected by e.g. sensors that we attach to the substrate. This leads to additional edge-like features in e.g. the nuclear recoil spectrum. I refer to these as “defect edges”. To see why, let us consider a simple defect model where if $\omega \geq E_D$ then one and only one permanent defect is formed that stores an energy of amount E_D . If $\omega < E_D$ then no defect is formed and the full recoil energy is collected. E_D is referred to as the **displacement energy** or **defect energy**.

In this model, the energy collected E_C is equal to ω minus the energy lost to defect which is a step function:

$$E_C(\omega) = \omega - E_D \Theta(\omega - E_D) \quad (2.50)$$

where Θ denotes the Heaviside step function.

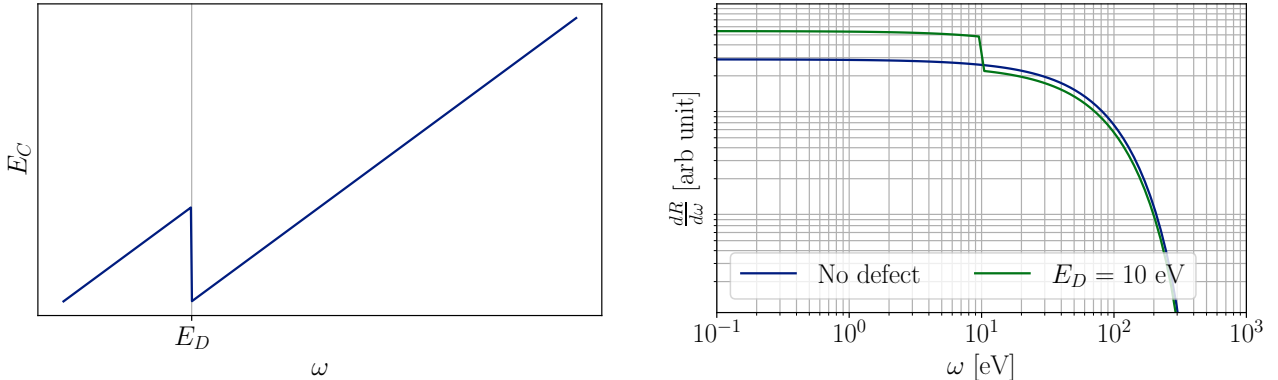


Figure 2.3: (left) Energy collected E_C as a function of energy deposited ω by the initial scattering event for a simple hard-threshold defect model. As long as ω goes beyond E_D we lost an amount of energy equal to E_D to defect formation which leads to a drop in E_C . (right) The event rate (eq. 2.52) under this defect model. Blue is the original spectrum without any defect formation and green is the modified observed spectrum with $E_D=10$ eV.

Now since we do not observe ω directly but rather E_C , the spectrum that we measure experimentally will be modified:

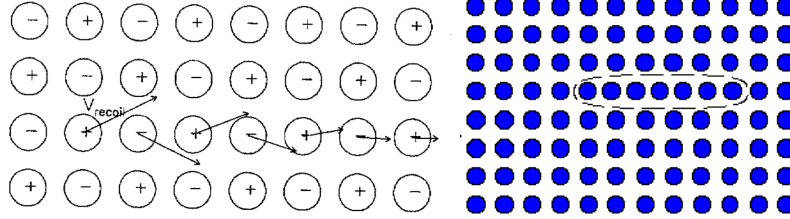


Figure 2.4: (left) An illustration of replacement collision sequence in alkali halide taken from [123]. The direction of the recoil velocity progressively aligns to the [100] direction. In this case the charges on the ions facilitates the formation of an RCS. (right) Formation of crowdion from an RCS. A crowdion is a linear interstitial defect that propagates along one of the axis of symmetry in the lattice. Crowdions can travel faster than the speed of sound in the material.

$$\frac{dR}{dE_C}(\omega) = \int \frac{dR}{d\omega}(\omega') \delta(E_C(\omega') - \omega) d\omega' \quad (2.51)$$

$$= \begin{cases} \frac{dR}{d\omega}(\omega + E_D) & \omega > E_D \\ \frac{dR}{d\omega}(\omega) + \frac{dR}{d\omega}(\omega + E_D) & \omega < E_D \end{cases} \quad (2.52)$$

Thus we can see that the spectrum has a jump at $\omega = E_D$ of magnitude $\frac{dR}{d\omega}(E_D)$ (figure 2.3).

For real materials, the defect formation is less abrupt and thus $E_C(\omega)$ would be a smoother function. However it remains true that energy loss due to defect formation produces edge-like features at the relevant characteristic energy. More detailed calculations of this effect for real materials can be performed via molecular dynamics simulations [84].

Apart from modifying our measured spectra, we can also try to look for long-lived defects or crystal damages directly with microscopy [143, 44] in order to search for DM. This class of techniques is referred to as “defect spectroscopy” and can produce very competitive bounds on high-mass DM.

2.2.4 Crowdion

In crystal systems that have a high degree of symmetry, the primary knock-on atom can trigger a **replacement collision sequence** (RCS) if it was scattered at the right angle. An RCS is similar to what happens in a Newton’s cradle where the incident nucleus transfer all its momentum to the next nucleus and “replace” its position in the lattice. This is perhaps easiest to visualize with a cubic lattice (figure 2.4).

The RCS can be modelled by a solitary wave that travels faster than the speed of sound in the material called the **crowdion** [140]. As such, it will produce Cherenkov phonons via the acoustic

Cherenkov effect [123, 140]. A further discussion of acoustic Cherenkov can be found in section 3.3. If the existence of solitonic excitations in the lattice system is verified then in principle we shall be able to recover directional information of the incident DM particle on a per-event basis, given that our phonon sensor is sufficiently sensitive. We shall return to this discussion in Chapter 3.

2.3 Electron System

Let us now turn our attention to the electron system. We will focus on electrons in solid-state systems with a periodic structure. For discussion on excitation of atomic or molecular electrons refer to e.g. [49, 50, 85].

2.3.1 Bloch Wavefunctions

In order to calculate the rate we need to first know how to describe the states of electrons inside a periodic material. In periodic structures the delocalized valence electrons can be described by wavefunctions $\Psi_{i\mathbf{k}}(\mathbf{r})$ labelled by a discrete index i called the band index and some pseudo-momentum \mathbf{k} . According to Bloch's theorem we have

$$\Psi_{i\mathbf{k}}(\mathbf{r}) = e^{i\mathbf{k}\cdot\mathbf{r}} u_{i\mathbf{k}}(\mathbf{r}) \quad (2.53)$$

where $u_{i\mathbf{k}}(\mathbf{r})$ is some periodic function with the same periodicity as the crystal, i.e. $u_{i\mathbf{k}}(\mathbf{r}+\mathbf{R}) = u_{i\mathbf{k}}(\mathbf{r})$ for any \mathbf{R} that is a lattice vector. Any such periodic function can be written as a Fourier expansion of the form:

$$u_{i\mathbf{k}}(\mathbf{r}) = \sum_{\mathbf{G}} e^{i\mathbf{G}\cdot\mathbf{r}} u_{i\mathbf{k}\mathbf{G}} \quad (2.54)$$

where \mathbf{G} are the reciprocal lattice vectors with the property $\mathbf{G}\cdot\mathbf{R} = 2n\pi$ for some integer n . It is easy to verify that functions of this form indeed has the same periodicity as the crystal.

In other words the wavefunctions are completely specified by the coefficients $u_{i\mathbf{k}\mathbf{G}}$ via

$$\Psi_{i\mathbf{k}}(\mathbf{r}) = \frac{1}{\sqrt{V}} \sum_{\mathbf{G}} e^{i(\mathbf{k}+\mathbf{G})\cdot\mathbf{r}} u_{i\mathbf{k}\mathbf{G}} \quad (2.55)$$

where we have also introduced the normalization factor $1/\sqrt{V}$ such that we have $\sum_{\mathbf{G}} |u_{i\mathbf{k}\mathbf{G}}|^2 =$

1. We use the word wavefunction to refer to $\Psi_{i\mathbf{k}}(\mathbf{r})$ or $u_{i\mathbf{k}\mathbf{G}}$ interchangeably since they carry exactly the same information.

For any particular material we will need to solve for the wavefunctions $u_{i\mathbf{k}\mathbf{G}}$ and their corresponding energy eigenvalues $E_{i\mathbf{k}}$. This is a highly non-trivial calculation since the system consists of $O(10^{23})$ interacting electrons. The standard approach to solving such a system is using density functional theory (DFT) which is on its own a vast subject. We defer the discussion of DFT to appendix A and for now simply assume that we are handed these wavefunctions and energy eigenvalues for any material of interest.

2.3.2 Electron Transition

We can now proceed to write down the structure factor for **electron recoil** (ER) where an electron originally in the valence band is promoted to conduction band via scattering with the DM particle. Recall that the target-dependent operator is given by $\mathcal{O}_T = \sum_i e^{i\mathbf{q} \cdot \mathbf{r}_i}$ which sums over all the electrons in the system. The matrix element $\langle f | \mathcal{O}_T | 0 \rangle$ is a highly non-trivial object due to interactions between electrons. One simplification we can make is to assume that the electrons are independent, then the total matrix element can be written as the sum of single-electron matrix elements. For example let us consider the case where an electron originally in state $\Psi_{i\mathbf{k}}$ is promoted to another state $\Psi_{i'\mathbf{k}'}$, the matrix element $f_{i\mathbf{k} \rightarrow i'\mathbf{k}'}$ is given by

$$f_{i\mathbf{k} \rightarrow i'\mathbf{k}'} = \int d^3\mathbf{r} \Psi_{i'\mathbf{k}'}(\mathbf{r}) e^{i\mathbf{q} \cdot \mathbf{r}} \Psi_{i\mathbf{k}}(\mathbf{r}) \quad (2.56)$$

$$= \frac{1}{V} \sum_{\mathbf{G}, \mathbf{G}'} \int d^3\mathbf{r} e^{i(\mathbf{k} + \mathbf{G} - \mathbf{k}' - \mathbf{G}' + \mathbf{q}) \cdot \mathbf{r}} u_{i'\mathbf{k}'\mathbf{G}'}^* u_{i\mathbf{k}\mathbf{G}} \quad (2.57)$$

$$= \frac{(2\pi)^3}{V} \sum_{\mathbf{G}, \mathbf{G}'} \delta^{(3)}(\mathbf{k} + \mathbf{G} - \mathbf{k}' - \mathbf{G}' + \mathbf{q}) u_{i'\mathbf{k}'\mathbf{G}'}^* u_{i\mathbf{k}\mathbf{G}} \quad (2.58)$$

$$= \frac{(2\pi)^3}{V} \sum_{\mathbf{G}'} \delta^{(3)}(\mathbf{q} - (\mathbf{k}' - \mathbf{k} + \mathbf{G}')) \sum_{\mathbf{G}} u_{i'\mathbf{k}'(\mathbf{G}' + \mathbf{G})}^* u_{i\mathbf{k}\mathbf{G}} \quad (2.59)$$

where in the last line we have simply relabelled $\mathbf{G}' - \mathbf{G}$ to \mathbf{G}' . Taking the square gives

$$|f_{i\mathbf{k} \rightarrow i'\mathbf{k}'}|^2 = \left(\frac{(2\pi)^3}{V}\right)^2 \sum_{\mathbf{G}'\mathbf{g}'} \delta^{(3)}(\mathbf{q} - (\mathbf{k}' - \mathbf{k} + \mathbf{G}')) \delta^{(3)}(\mathbf{q} - (\mathbf{k}' - \mathbf{k} + \mathbf{g}')) \sum_{\mathbf{G},\mathbf{g}} u_{i'\mathbf{k}'(\mathbf{G}'+\mathbf{G})}^* u_{i\mathbf{k}\mathbf{G}} u_{i'\mathbf{k}'(\mathbf{g}'+\mathbf{g})}^* u_{i\mathbf{k}\mathbf{g}} \quad (2.60)$$

$$= \frac{(2\pi)^3}{V} \sum_{\mathbf{G}'} \delta^{(3)}(\mathbf{q} - (\mathbf{k}' - \mathbf{k} + \mathbf{G}')) \left| \sum_{\mathbf{G}} u_{i'\mathbf{k}'(\mathbf{G}'+\mathbf{G})}^* u_{i\mathbf{k}\mathbf{G}} \right|^2 \quad (2.61)$$

$$= \frac{(2\pi)^3}{V} \sum_{\mathbf{G}'} \delta^{(3)}(\mathbf{q} - (\mathbf{k}' - \mathbf{k} + \mathbf{G}')) |f_{[i\mathbf{k}i'\mathbf{k}'\mathbf{G}']}|^2 \quad (2.62)$$

where we have used the fact that the product of delta functions is only non-zero when $G' = g'$ and $\delta^{(3)}(0) = (\text{total number of allowed states}) = \frac{V}{(2\pi)^3}$.

Under the independent electron assumption the total structure factor is simply given by the summation

$$S(\mathbf{q}, \omega) = 2 \times \frac{2\pi}{V} \sum_{ii'} \int_{BZ} \frac{V d^3\mathbf{k}}{(2\pi)^3} \frac{V d^3\mathbf{k}'}{(2\pi)^3} |f_{i\mathbf{k} \rightarrow i'\mathbf{k}'}|^2 \delta(E_{i'\mathbf{k}'} - E_{i\mathbf{k}} - \omega) \quad (2.63)$$

$$= 2(2\pi)^4 \sum_{ii'\mathbf{G}'} \int_{BZ} \frac{d^3\mathbf{k}}{(2\pi)^3} \frac{d^3\mathbf{k}'}{(2\pi)^3} |f_{[i\mathbf{k}i'\mathbf{k}'\mathbf{G}']}|^2 \delta^{(3)}(\mathbf{q} - (\mathbf{k}' - \mathbf{k} + \mathbf{G}')) \delta(E_{i'\mathbf{k}'} - E_{i\mathbf{k}} - \omega) \quad (2.64)$$

The additional factor of 2 is there to account for the electron spin. Note that we assume that in the ground state the valence band is completely filled and so i runs over valence bands only and i' runs over conduction bands only.

Once again this result assumes the electrons are independent and the total state is simply a direct product of single electron states. Electron correlation and screening (in-medium effects) are not included in this calculation. For cases with heavy mediators or high momentum transfer, these effects does not contribute significantly and thus the above equation is a good approximation. In section 2.3.4 we will present a more complete treatment that includes all the many-electron effects. But for now we shall continue with this model and further our physical intuition.

2.3.3 Nearly Free Electron Model

In the case of nuclear recoil we have identified some important criteria for effective detection, e.g. mass matching. For electron recoil we would like to do the same but it is not immediately obvious how to proceed since the wave-functions are obtained computationally and doesn't seem to have a simple relation to other physical properties of the material. We can sidestep this difficulty by

adopting the **nearly free electron approximation** (NFEG). Under this approximation we assume the wavefunctions $u_{i\mathbf{k}\mathbf{G}}$ only depend on the momentum very weakly and so $|u_{i\mathbf{k}\mathbf{G}}| \approx u_0$ where u_0 is some material-independent constant.

This approximation is justified because a typical electron scattering event has $q \sim O(10)$ keV and $\omega \sim O(10)$ eV. This is significantly higher than typical bandgap with $k_g \sim O(1)$ keV and $E_g \sim O(1)$ eV. Thus the typical electron transition occurs far away from the band edge and can be approximated by free electrons.

Under NFEG the structure factor now becomes a purely kinematic quantity and only depends on the band structure:

$$S(\mathbf{q}, \omega) = 2(2\pi)^4 u_0^2 \sum_{ii'\mathbf{G}} \int_{BZ} \frac{d^3\mathbf{k}}{(2\pi)^3} \frac{d^3\mathbf{k}'}{(2\pi)^3} \delta^{(3)}(\mathbf{q} - (\mathbf{k}' - \mathbf{k} + \mathbf{G})) \delta(E_{i'\mathbf{k}'} - E_{i\mathbf{k}} - \omega) \quad (2.65)$$

$$= 4\pi u_0^2 \sum_{ii'\mathbf{G}} \int_{BZ} \frac{d^3\mathbf{k}}{(2\pi)^3} \delta(E_{i'\mathbf{k}+\mathbf{q}-\mathbf{G}} - E_{i\mathbf{k}} - \omega) \quad (2.66)$$

$$= 2\pi u_0^2 J(\mathbf{q}, \omega) \quad (2.67)$$

where $J(\mathbf{q}, \omega)$ is the **joint density-of-state** (JDOS) of the material and is defined as

$$J(\mathbf{q}, \omega) = 2 \sum_{ii'\mathbf{G}} \int_{BZ} \frac{d^3\mathbf{k}}{(2\pi)^3} \delta(E_{i'\mathbf{k}+\mathbf{q}-\mathbf{G}} - E_{i\mathbf{k}} - \omega) \quad (2.68)$$

The JDOS can be calculated explicitly for a two-band model with parabolic dispersion relations:

$$E_c(k) = \frac{E_g}{2} + \frac{k^2}{2m_c} \quad (2.69)$$

$$E_v(k) = -\frac{E_g}{2} - \frac{(k - k_g)^2}{2m_v} \quad (2.70)$$

where E_g is the energy gap and $m_{c,v}$ are the effective masses. The corresponding JDOS is [43]

$$J(q, \omega) \propto \left(\omega - E_g - \frac{(q - k_g)^2}{2(m_c + m_v)} \right)^{3/2} \quad (2.71)$$

which is non-zero only if

$$\omega - \frac{(q - k_g)^2}{2(m_c + m_v)} > E_g \quad (2.72)$$

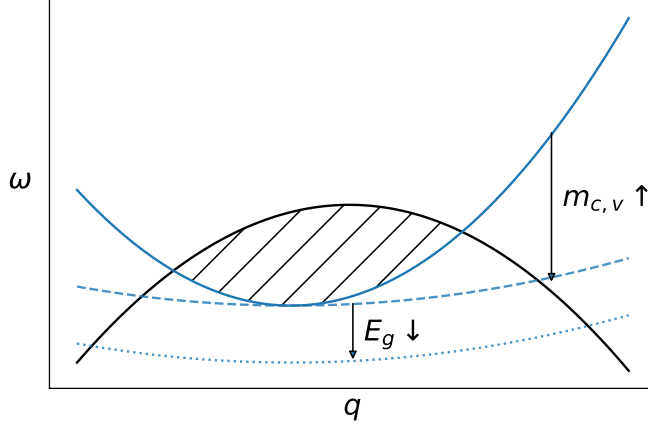


Figure 2.5: Accessible phase space of the scattering process bounded by equation 2.72 (blue solid) and equation 2.73 (black solid). The available phase space can be enlarged by having higher effective masses (blue dashed), as well as a lower band gap (blue dotted). The maxima of the black line is at $q = m_\chi(v_{\text{esc}} + v_E)$ while the minima of the blue line is at $q = k_g$.

Additionally, we note from its definition that $\eta(v_{\min})$ is non-zero only if

$$\frac{q}{2m_\chi} + \frac{\omega}{q} < v_{\text{esc}} + v_e \quad (2.73)$$

The accessible phase space is thus bounded by the two constraints given by equations 2.72 and 2.73. The area of this region is maximal when

$$k_g \approx m_\chi(v_{\text{esc}} + v_e), \quad m_c + m_v \rightarrow \infty, \quad E_g \rightarrow 0 \quad (2.74)$$

The situation is illustrated in figure 2.5. Thus under the nearly free electrons assumption, materials with flat bands and small energy gaps are best-suited for detection of dark matter-electron scattering. We will consider a class of materials with these properties in section 4.2.

2.3.4 Dielectric Formulation

Let us now return to the issues of many-electron effects. In many materials the electrons cannot be viewed as independent nor weakly-interacting especially in the low momentum transfer regime where we are most interested as we want to detect light dark matter. Modelling all the correlation and interaction from first principles would be a daunting task. Fortunately it is possible to encapsulate

all the many-body effects into a single function called the dielectric function, which in principle can also be directly measured via experimental techniques. In this section we are going to present a formulation of the structure factor in terms of the more experimentally accessible dielectric function (more precisely the energy-loss function) instead of the electron wavefunctions.

Recall that the target-dependent operator is given by

$$\mathcal{O}_T(\mathbf{q}) = \sum_i e^{i\mathbf{q} \cdot \mathbf{r}_i} \quad (2.75)$$

$$= \int d^3\mathbf{r} \left(\sum_i \delta^{(3)}(\mathbf{r} - \mathbf{r}_i) \right) e^{i\mathbf{q} \cdot \mathbf{r}} \quad (2.76)$$

$$= \rho(\mathbf{q}) \quad (2.77)$$

The quantity inside the bracket in the second line is simply the electron density. Thus the target-dependent operator is equal to the electron density operator ρ in momentum representation.

The matrix element of ρ is related to the dielectric function via a result from linear-response theory [59, 132]:

$$\text{Im} \left(-\frac{1}{\epsilon(\mathbf{q}, \omega)} \right) = \frac{\pi e^2}{q^2 V} \sum_f |\langle f | \rho(q) | 0 \rangle|^2 \delta(E_f - E_0 - \omega) \quad (2.78)$$

We can see that the right-hand side has the exact same form as the structure factor. Thus we can write:

$$S(\mathbf{q}, \omega) = \frac{2q^2}{e^2} \text{Im} \left(-\frac{1}{\epsilon(\mathbf{q}, \omega)} \right) \quad (2.79)$$

$$= \frac{2q^2}{e^2} \mathcal{W}(\mathbf{q}, \omega) \quad (2.80)$$

where $\mathcal{W}(\mathbf{q}, \omega) = \text{Im} \left(-\frac{1}{\epsilon(\mathbf{q}, \omega)} \right)$ is called the **energy-loss function** (ELF) of the material. This formula is more complete than 2.64 as it takes into account all the various many-body effects such as screening and plasmon. In particular unlike the wavefunctions the ELF can be experimentally measured and thus allow us to directly calibrate the electron recoil rate against ELF measurements. There are also analytical models of dielectric functions that can be used to understand the qualitative features of DM electron scattering [85], for example under the free-electron gas approximation

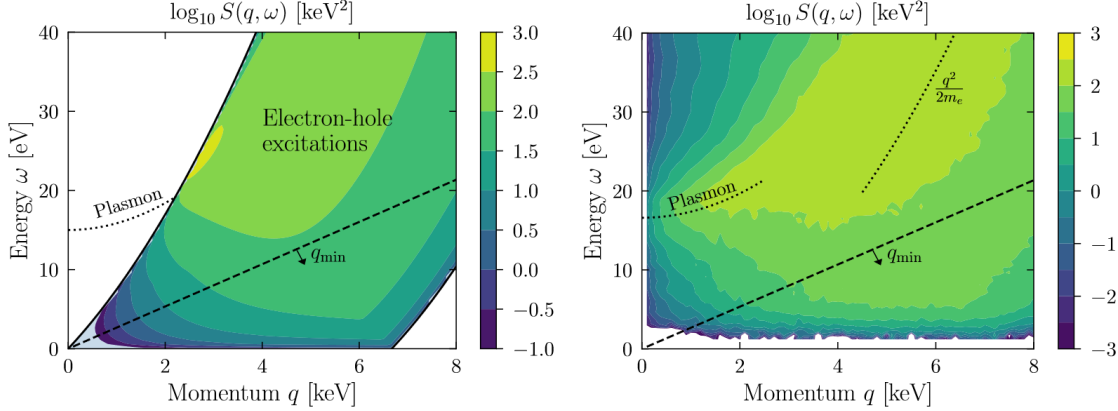


Figure 2.6: Figure taken from [85]. (left) Structure factor for a free electron gas with $\omega_p = 15$ eV, $k_F = 3.3$ keV, and taking the $\Gamma_p \rightarrow 0$ limit of equation 2.82. The plasmon resonance shows up as an infinitely narrow resonance indicated by the dotted line, while the rest of the support is interpreted as electron-hole excitations. (right) Structure factor for silicon based on the calculation in [95]. In both panels, the dashed line indicates $q = \omega v_{\max}$ where v_{\max} is the maximum DM speed on Earth, such that the kinematically-accessible region is below and to the right of the dashed line. As can be seen, the plasmon peaks of the structure factor are not accessible for our DM halo.

we have [42]:

$$\epsilon_{\text{FEG}}(\mathbf{q}, \omega) = 1 + \lim_{\eta \rightarrow 0} \frac{3\omega_p^2}{q^2 v_F^2} \left[\frac{1}{2} + \frac{k_F}{4q} \left(1 - \left(\frac{q}{k_F} - \frac{\omega + i\eta}{qv_F} \right)^2 \right) \log \left(\frac{\frac{q}{2k_F} - \frac{\omega + i\eta}{qv_F} + 1}{\frac{q}{2k_F} - \frac{\omega + i\eta}{qv_F} - 1} \right) \right] \quad (2.81)$$

$$\left. \frac{k_F}{4q} \left(1 - \left(\frac{q}{k_F} + \frac{\omega + i\eta}{qv_F} \right)^2 \right) \log \left(\frac{\frac{q}{2k_F} + \frac{\omega + i\eta}{qv_F} + 1}{\frac{q}{2k_F} + \frac{\omega + i\eta}{qv_F} - 1} \right) \right] \quad (2.82)$$

We have plotted the resulted structure factor in figure 2.6.

The ELF formulation also allows us to derive general bounds on the structure factor via various sum rules [104]. This is especially powerful since it allows us to derive general results on the DM detection rate without knowing any material-specific details.

2.3.5 Optical Interactions

If the DM sector contains a boson that couples to the electron, which is the case for **dark photon** (DP) and **axion-like particle** (ALP), the incident DM particle can interact with electrons in ways that are analogous to photon interactions such as photoelectric effect and Compton scattering. The cross-sections of these optical interactions for DM have simple relations to the photon cross-sections in the material.

Absorption DM absorption process is completely analogous to the familiar photoelectric effect which dominates the photon interaction cross-section at energies below around 50 keV [67].

For dark photon the coupling to electron is generated via kinetic mixing [75] which results in the following Lagrangian:

$$\mathcal{L} \supset -\frac{1}{4}F'^{\mu\nu}F'_{\mu\nu} - \frac{\kappa}{2}F^{\mu\nu}F'_{\mu\nu} + \frac{1}{2}m_{A'}A'^{\mu}A'_{\mu} + eJ_{\text{EM}}^{\mu}A_{\mu} \quad (2.83)$$

where κ is the DP mixing parameter, $F_{\mu\nu}$ and $F'_{\mu\nu}$ are the field strengths for the photon and dark photon respectively, A'_{μ} is the dark photon vector potential and J_{EM}^{μ} is the electromagnetic current (i.e. electrons). After diagonalizing the fields we can see that the dark photon effectively couples to the EM current with a reduced charge [51]:

$$\mathcal{L}' \supset -\frac{1}{4}F'^{\mu\nu}F'_{\mu\nu} + \frac{1}{2}m_{A'}A'^{\mu}A'_{\mu} + \kappa e J_{\text{EM}}^{\mu}A'_{\mu} \quad (2.84)$$

Mathematically this is just massive QED. In a dielectric material it is important to also include the renormalization of the photon propagator due to interaction with the medium (in-medium effect). The result of this renormalization is equivalent to replacing the mixing parameter κ with an effective mixing parameter κ_{eff} [11, 121]:

$$\kappa_{\text{eff}}^2(\omega) = \kappa^2 \frac{m_{A'}^4}{[m_{A'}^2 - \text{Re } \Pi(\omega)]^2 + [\text{Im } \Pi(\omega)]^2} \quad (2.85)$$

where $\Pi(\omega)$ is the magnitude of the photon self-energy tensor (polarization tensor). One can think of this as a form of charge screening by the medium.

To leading order the DP absorption rate $\Gamma_{\text{DP}}(m_{A'})$ for DP of mass $m_{A'}$ is then simply related to the photon absorption rate $\Gamma_{\text{PE}}(\omega)$ via

$$\Gamma_{\text{DP}}(m_{A'}) = \kappa_{\text{eff}}^2 \Gamma_{\text{PE}}(\omega = m_{A'}) \quad (2.86)$$

Here we are assuming that the DP is approximately at rest, which is valid for halo DM. The photon absorption rate is related to the photon self-energy $\Pi(\omega)$ via [10, 11]

$$\Gamma_{\text{PE}}(\omega) = -\frac{\text{Im } \Pi(\omega)}{\omega} \quad (2.87)$$

The photon self-energy can be related to the complex conductivity $\sigma(\omega)$ via [71]:

$$\Pi(\omega) = -i\sigma(\omega)\omega \quad (2.88)$$

Therefore the rate is given by [70, 72]

$$R = \frac{1}{\rho_T} \frac{\rho_\chi}{m_{A'}} \Gamma_{\text{DP}} \quad (2.89)$$

$$= \frac{1}{\rho_T} \frac{\rho_\chi}{m_{A'}} \kappa_{\text{eff}}^2 \Gamma_{\text{PE}}(m_{A'}) \quad (2.90)$$

$$= \frac{1}{\rho_T} \frac{\rho_\chi}{m_{A'}} \kappa_{\text{eff}}^2 \text{Re } \sigma(m_{A'}) \quad (2.91)$$

For DM that has a pseudo-scalar coupling to the electron, such is the case for ALP, the relevant interaction is described by [70]

$$\mathcal{L} \supset \frac{g_{aee}}{2m_e} (\partial_\mu a) \bar{\psi} \gamma^\mu \gamma^5 \psi \quad (2.92)$$

where ψ denotes the electron Dirac field and a is the pseudo-scalar field. In the non-relativistic limit, the ALP absorption rate can again be related to the photon absorption rate via [138]

$$\Gamma_{\text{ALP}}(\omega) = \frac{3m_a^2}{4m_e^2} \frac{g_{aee}^2}{e^2} \Gamma_{\text{PE}}(\omega = m_a) \quad (2.93)$$

and thus we have the rate for ALP absorption:

$$R = \frac{1}{\rho_T} \frac{\rho_\chi}{m_a} \frac{3m_a^2}{4m_e^2} \frac{g_{aee}^2}{e^2} \text{Re } \sigma(m_a) \quad (2.94)$$

Figure 2.7 shows the limit plots for DP and ALP absorption calculated from the above rates.

Compton Scattering When the mass of the bosonic DM becomes larger than 100 keV or so the corresponding photon cross-section is dominated by Compton scattering instead of photo-electric effect. As such we need to consider instead the process of **dark Compton scattering** [72] (see figure 2.8) for DP/ALP mass in the 100 keV to 1 MeV range.

The dark Compton scattering rate for DP and ALP are easy to compute if we adopt the free-electron approximation (FEA). The use of the FEA is justified here since the rate of dark Compton scattering will only be significant compared to the absorption rate of the dark bosons when the mass of DM is large ($m_{\text{DM}} \gtrsim 100$ keV). In this regime, the energy received by the electron in the event is larger than most atomic binding energies and can thus the electron can be treated as approximately

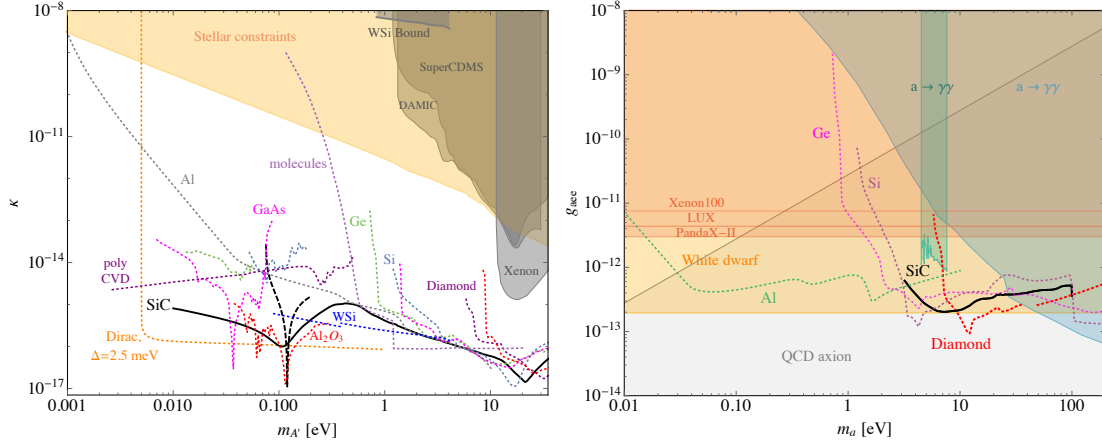


Figure 2.7: Figure taken from [61]. Projected reach at 95% C.L. for absorption of kinetically mixed dark photons (left) and axion-like particles (right). The expected reach assumes a kg-year exposure for all materials. Shaded regions represent parameter space excluded by various experimental and observational constraints. The allowed QCD axion region is colored in shaded gray in the right plot.

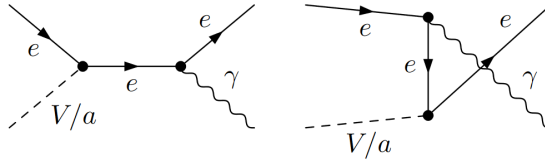


Figure 2.8: Tree-level Feynman diagrams illustrating the Compton-like process where a dark matter boson is converted to a photon via electron scattering.

free [142].

From energy-momentum conservation we can calculate the energy of the emitted photon ω_γ to be

$$\omega_\gamma = \frac{m_{V/a}^2 + 2m_e\omega_{V/a}}{2(m_e + \omega_{V/a} - \sqrt{\omega_{V/a}^2 - m_{V/a}^2} \cos \theta)} \quad (2.95)$$

where $\omega_{V/a}$ is the energy of the incoming dark boson, m_e is the mass of the electron, $m_{V/a}$ is the mass of the incoming DP or ALP and θ is the angle of the emitted photon. If the DM is

slow-moving, such is the case for halo DM, then $\omega_{V/a} \rightarrow m_{V/A}$ and we have

$$\omega_\gamma = \frac{m_{V/A}(m_{V/A} + 2m_e)}{2(m_e + m_{V/A})} \quad (2.96)$$

and the electron recoil energy ω is given by

$$\omega = \omega_{V/a} - \omega_\gamma = \frac{m_{V/a}^2}{2(m_e + m_{V/a})} \quad (2.97)$$

Note that there is no angular dependence, and thus unlike in the case of ordinary Compton scattering where the energy spectrum has a broad support, the energy spectrum of the dark Compton scattering is a delta function centered around a single energy!

The differential cross-section for dark Compton scattering is given by

$$d\sigma = \frac{1}{4m_e\omega_{V/a} v} d\Pi_{\text{LIPS}} \langle |\mathcal{M}|^2 \rangle \quad (2.98)$$

where v is the speed of halo DM and $d\Pi_{\text{LIPS}}$ is the Lorentz invariant phase space:

$$\int d\Pi_{\text{LIPS}} = \int \frac{d\cos\theta}{8\pi} \frac{\omega_\gamma}{\omega_{V/a} + m_e - \sqrt{\omega_{V/a}^2 - m_{V/a}^2} \cos\theta}. \quad (2.99)$$

For DP the matrix element is given by

$$\begin{aligned} \langle |\mathcal{M}|^2 \rangle &= \frac{e^4 \kappa^2}{6} \left(\frac{2m_e^2 + m_V^2}{\omega_\gamma^2} + \frac{4m_e\omega_\gamma}{2m_e\omega_V + m_V^2} \right. \\ &\quad + \frac{4(2m_e^2 + m_V^2)(m_e^2 + 2m_e\omega_V + m_V^2)}{(2m_e\omega_V + m_V^2)^2} \\ &\quad \left. + \frac{m_V^4 + 4m_e^2(\omega_V^2 - m_V^2) - 8m_e^3(\omega_V + m_e)}{m_e\omega_\gamma(2m_e\omega_V + m_V^2)} \right). \end{aligned} \quad (2.100)$$

Here we do not need to include in-medium effect as they are insignificant in the DM mass regime [70] that we are considering.

Converting the cross-section to an event rate (per unit time per unit mass) via

$$R = \frac{1}{\rho_T} \frac{\rho_{\text{DM}}}{m_V} n_e \sigma v \quad (2.101)$$

gives

$$\frac{dR}{d\cos\theta} = \frac{n_e \rho_{\text{DM}}}{\rho_T m_V} \frac{e^4 \kappa^2 \omega_\gamma}{48\pi m_e \omega_V (\omega_V + m_e - \sqrt{\omega_V^2 - m_V^2} \cos\theta)} \times \\ \left(\frac{2m_e^2 + m_V^2}{\omega_\gamma^2} + \frac{4m_e \omega_\gamma}{2m_e \omega_V + m_V^2} \right. \\ + \frac{4(2m_e^2 + m_V^2)(m_e^2 + 2m_e \omega_V + m_V^2)}{(2m_e \omega_V + m_V^2)^2} \\ \left. + \frac{m_V^4 + 4m_e^2(\omega_V^2 - m_V^2) - 8m_e^3(\omega_V + m_e)}{m_e \omega_\gamma (2m_e \omega_V + m_V^2)} \right). \quad (2.102)$$

Note that this expression does not exactly reduce to the Klein-Nishina formula [94] for SM photons in the $m_V \rightarrow 0$ limit since the dark photon, being a massive vector boson, has one more degree of freedom than the SM photon.

The total dark Compton rate for a slow-moving DM flux is found through integration and setting $\omega \approx m_V$, yielding

$$R = \frac{n_e \rho_{\text{DM}}}{\rho_T m_V} \frac{e^4 \kappa^2}{24\pi m_e^2} \frac{(m_V + 2m_e)(m_V^2 + 2m_e m_V + 2m_e^2)}{(m_V + m_e)^3} \quad (2.103)$$

$$\approx \frac{n_e \rho_{\text{DM}}}{\rho_T m_V} \frac{e^4 \kappa^2}{24\pi m_e^2} \times \begin{cases} 1 & \text{for } m_V \gg m_e \\ 4 & \text{for } m_V \ll m_e \end{cases} \quad (2.104)$$

For ALP the matrix element is given by

$$\langle |\mathcal{M}|^2 \rangle = \frac{e^2 g_{aee}^2}{4} \left(\frac{m_a^2}{\omega_\gamma^2} + \frac{m_a^4 - 4m_a^2 m_e^2 + 4m_e^2 \omega_a^2}{m_e \omega_\gamma (m_a^2 + 2m_e \omega_a)} \right. \\ \left. + \frac{4m_a^2 m_e^2}{(m_a^2 + 2m_e \omega_a)^2} + \frac{4m_e \omega_\gamma - 8m_e \omega_a}{m_a^2 + 2m_e \omega_a} \right), \quad (2.105)$$

and the differential rate is

$$\frac{dR}{d\cos\theta} = \frac{n_e \rho_{\text{DM}}}{\rho_T m_a} \frac{e^2 g_{aee}^2 \omega_\gamma}{32\pi m_e \omega_a (\omega_a + m_e - \sqrt{\omega_a^2 - m_a^2} \cos\theta)} \times \\ \left(\frac{m_a^4 - 4m_a^2 m_e^2 + 4m_e^2 (\omega_a - \omega_\gamma)^2}{m_e \omega_\gamma (m_a^2 + 2m_e \omega_a)} \right. \\ \left. + \frac{m_a^2}{\omega_\gamma^2} + \frac{4m_a^2 m_e^2}{(m_a^2 + 2m_e \omega_a)^2} \right) \quad (2.106)$$

For a slow-moving DM flux, we have

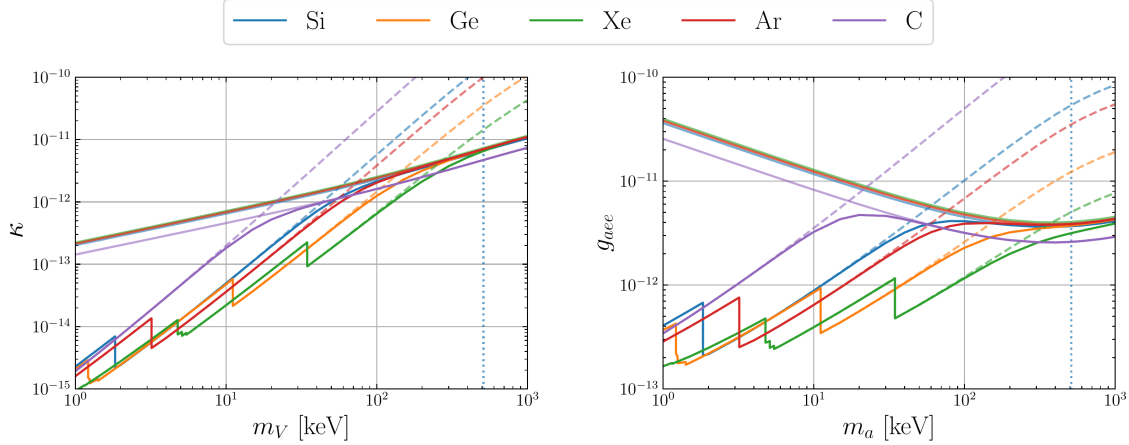


Figure 2.9: Projected 90% C.L. reach for relic dark photons (left) and axion-like particles (right) with a 1 kg-year exposure and no background. The reach for absorption (dashed lines) and Compton-like processes (thin solid lines) is indicated along with the combined reach (thick solid lines), showing substantially improved capabilities at higher DM masses when dark Compton scattering begins to dominate over absorption. The vertical dotted line indicates the mass of the electron.

$$R = \frac{n_e \rho_{\text{DM}}}{\rho_T} \frac{e^2 g_{aee}^2 m_a (m_a + 2m_e)^2}{16\pi m_e^2 (m_a + m_e)^4} \quad (2.107)$$

$$\approx \frac{n_e}{\rho_T} \frac{\rho_{\text{DM}}}{m_a} \frac{e^2 g_{aee}^2}{16\pi m_e^2} \times \begin{cases} 1 & \text{for } m_a \gg m_e \\ 4m_a^2/m_e^2 & \text{for } m_a \ll m_e \end{cases} \quad (2.108)$$

The photon emitted from the dark Compton scattering may get absorbed by the detector depending on the material and thickness of the substrate. If the energy of the photon is fully absorbed back into the substrate, the total energy deposited will be equal to the full mass of the dark boson and the event will look like an absorption event. In this case the energy spectrum will qualitatively look like an absorption spectrum except that the rate would be significantly higher. For more discussion on detector considerations for dark Compton events please refer to [72].

2.4 Mixed Channels

Apart from interacting solely with the lattice or the electron system, there are also interactions which simultaneously puts energy into both system. We briefly discuss several examples of this kind of interaction channels without delving into the details. Interested reader should consult the

relevant references cited.

2.4.1 Phonon-Assisted Electron Transition

The dielectric functions used for ER calculation are either based on electron gas (neglecting the lattice) or some form of DFT calculation where the nuclei are clamped [95]. However in reality the electron transition can be accompanied by a simultaneous absorption or emission of a phonon, producing both a ER and a single phonon. This additional phonon opens up some otherwise inaccessible phase space and can significantly change the structure factor near the band gap.

A quick way to include the effect of phonon co-production in the existing DFT calculation of the dielectric function is via the semi-classical algorithm described in [173, 174] (see also section A.4). What is particularly interesting is that instead of needing to perform a thermal average over many calculations as one would expect, they found that if the positions of the nuclei in the lattice are adjusted according to a particular superposition of the normal modes, then no sampling/averaging is required and the calculation can be done in one shot. In other words, we can include the effect of the phonons without additional computation cost.

2.4.2 Inelastic Nuclear Recoil (Bremsstrahlung)

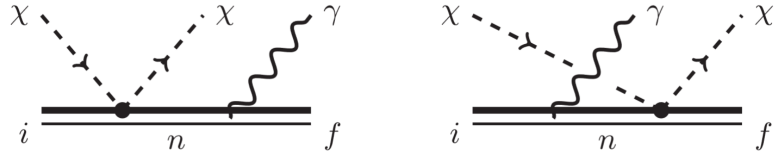


Figure 2.10: Feynman diagram for the inelastic nuclear recoil. The additional photon vertex adds a factor of α to the cross-section.

Apart from elastic nuclear recoil it is possible for the recoiling nuclei to simultaneously emit a photon [99]:

$$\chi + N \rightarrow \chi + N(E_R) + \gamma(\omega) \quad (2.109)$$

This turns the two-body scattering into a 2-3 scattering (figure 2.10) and opens up the phase space. The photon emitted can carry up to energy of $\omega_{\max} = \frac{\mu_{\chi N} v^2}{2} \approx 0.5 \text{ keV}$ which then goes on to generate a large ER signal, making it much easier to detect compared to a NR signal of similar energy. However the additional interaction vertex also lead to a suppression in the vertex. See [9, 83, 99] for more discussions.

2.4.3 Migdal Effect

The Migdal effect, similar to Bremsstrahlung, is a ER signal generated by a nuclear scattering. Instead of co-production of photon, co-production of electron recoil is involved [86]:

$$\chi + N \rightarrow \chi + N(E_R) + e(E_r) \quad (2.110)$$

Determination of the magnitude of the Migdal effect in solids is both a theoretical and an experimental challenge. Interestingly for low mass dark matter it is found that the Migdal rate can be related to photoabsorption cross-section $\sigma_{PE}(\omega)$ via [113]

$$\frac{dR}{dE_R E_r} = \frac{A^2 \mu_\chi^2 m_e^2 \bar{\sigma}}{v_\chi^2} F_\chi(q) \frac{E_R}{E_r} \frac{\sigma_{PE}(E_r)}{4\pi^2 \alpha} \quad (2.111)$$

For more discussion on Migdal effect please refer to [86, 96, 108].

Chapter 3

Detector Response

In the previous chapter we have discussed various ways that a dark matter particle can interact with the particles in our condensed matter system. The initial interaction generates a primary excitation (e.g. a primary phonon or an electron-hole pair) which then continues to interact with the material as it propagates and potentially decays or relaxes into secondary excitations. The detailed physics of how the energy of e.g. a recoiling nucleus gets converted into other excitations can be quite complicated. We instead take a more phenomenological approach and model the final partition of energy into phonons and electron-hole pairs (ionization) with a function called the **ionization yield**. In SuperCDMS-style detectors where we only collect phonons, we also convert much of the ionization energy into phonons via a process called **Neganov-Trofimov-Luke effect** (NTL). Because of this we will only focus on phonon transport in this chapter. For discussion on charge transport refer to [101, 155].

Towards the end of this chapter we will also discuss phonon collection into the sensors and the physics of **transition-edge sensors** (TES).

3.1 Lindhard Model

Let us first consider the case for nuclear recoil. After the initial collision with the DM particle, the target nucleus gained an energy ω . Part of this energy U will go into breaking the atomic bound (given ω is sufficiently large) and the remainder will become the kinetic energy E_R of the recoiling nucleus:

$$\omega = E_R + U \tag{3.1}$$

The recoiling nucleus will go on to scatter other nuclei and electrons in the material. When the dust settles, E_R will be partitioned into energy that went into ionization E_{eh} and energy that went into motions of the nuclei (phonons) E_{ph} . Usually this partition is specified via a ratio called the **ionization yield or quenching factor** (QF):

$$Y(\omega) = E_{eh}/E_R = E_{eh}/(\omega - U) \quad (3.2)$$

where again ω is the initial energy deposited by the DM scattering.

The ionization loss can be modeled by a (screened) heavy ion moving across free electron gas. This results in what is referred to as the **Lindhard yield** [111, 149]:

$$Y(\omega) = 1 - \frac{1}{1 + kg(\omega)} \quad (3.3)$$

$$g(\omega) = 3\omega^{0.15} + 0.7\omega^{0.6} + \omega \quad (3.4)$$

This model is based on five simplifying assumptions:

1. $U=0$
2. No contribution to atomic motion due to electrons
3. Energy loss to electrons is small compared to energy transferred to recoiling ions
4. Effects of electrons and atomic collisions can be treated separately
5. Energy transferred per atomic collision is small compared to initial energy

In the low DM mass regime, ω is small and thus the validity of some of these assumptions is challenged. In particular the atomic binding energy, usually around a few eV, becomes comparable to the recoil energy as we go to lower DM masses (10-100 MeV) and can no longer be neglected. Sarkis et al.[149] introduced a modified Lindhard function that includes a constant non-zero U at low energy:

$$Y(\omega) = 1 - \frac{1}{1 + kg(\omega)} - C_0\omega^{-0.5} - C_1\omega^{-1} \quad (3.5)$$

where C_0, C_1 are fitted constants. Note that this expression is ill-behaved when $\omega \rightarrow 0$ because if U is non zero there is a hard cut-off at $\omega = U$ where no recoil is produced.

However, the slope of this modified model no longer matches the Lindhard model in the high ω regime. This is fixed by numerically interpolating between the Lindhard model in high ω regime

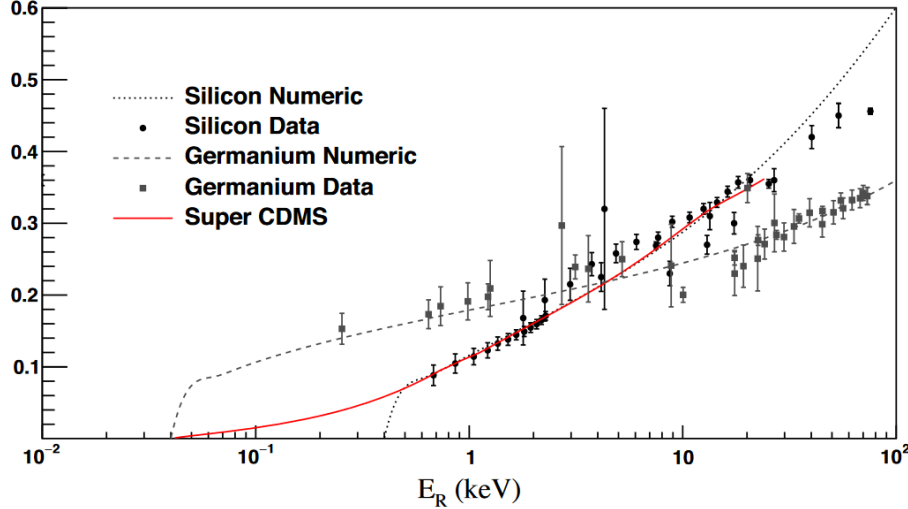


Figure 3.1: Ionization yield of Silicon and Germanium fitted against the modified Lindhard model described in [149]. The red curve is a separate phenomenological model proposed by SuperCDMS in [7].

and the constant U model in the low ω regime [149]. The final result fitted to measured data of silicon and germanium is shown in figure 3.1.

3.2 Electron Recoil Ionization Yield

In the case of electron transition the primary interacting electron receives the entire energy deposit. The initial hot carrier quickly transfer energies to other electrons and create more electron-hole pairs via a process called **impact ionization**. For electron recoil we are not so much interested in the ratio of energies but rather the number of electron-hole pairs we produce at the end, i.e. the **quantum yield**. The quantum yield is usually written as

$$n(\omega) = \frac{E_{eh}}{\epsilon_{eh}(\omega)} = Y(\omega) \frac{E_R}{\epsilon_{eh}(\omega)} \quad (3.6)$$

The average energy ϵ_{eh} required to create each additional electron-hole pair is usually significantly greater than the gap energy due to co-production of phonons in order to conserve both momentum and energy. An empirical formula for ϵ_{eh} is given by [35]

$$\epsilon_{eh} = A \cdot E_g + E_{ph} \quad (3.7)$$

where E_g is the band gap of the material, E_{ph} takes on values from 0.25 to 1.2 eV, and A is found to be ~ 2.2 to 2.9 [93].

In the high energy limit ($\omega > 50$ eV), ϵ_{eh} is a constant but in low energy regime it is a strong function of the electron energy ω [144]. The variance of the number of electron-hole pairs produced follows a Fano distribution with a Fano factor that is also a function of ω [144]. See figure 3.2 for data and fit to silicon.

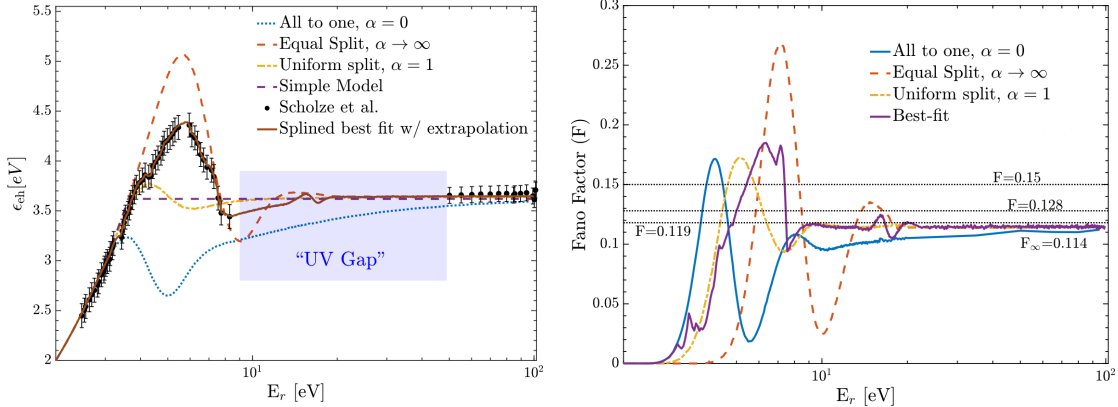


Figure 3.2: Plots of the quantum yield ϵ_{eh} (left) and Fano factor F (right) taken from [144]. The various fits are generated from phenomenological model based on a one-parameter Beta distribution parameterized by α . For more details refer to [144].

3.3 Neganov-Trofimov-Luke Effect

The redistribution of the initial energy deposit into ionization and phonons in accordance to the quenching factor takes place in a relatively short time frame ($\sim \mu\text{s}$) and confined to the neighborhood ($\sim \text{mm}$) of the initial scattering site. For large substrate we can effectively think of the initial scattering site as a point source of electron-hole pairs and phonons. This complicates the design of our detector because if we want to collect both excitations we will need to place both charge sensors and phonon sensors onto the substrate. Although doing so may have advantages such as event type discrimination, the two type of sensors are competing for space on the surface of the substrate which can affect their performance (e.g. phonons may get collected at charge sensors and become lost energy). Having two types of sensors also complicates event reconstruction and calibration.

In the latest iteration of SuperCDMS detectors we only place phonon sensors onto the surface of the substrate and optimize everything for phonon collection. As such we need a way to convert

the ionization energy into phonons to recover the full energy. This is achieved via a process called **Neganov-Trofimov-Luke** (NTL) amplification.

The NTL effect is essentially a form of acoustic Cherenkov effect. In the optical Cherenkov effect, if a charged particle travels through a medium at a speed higher than the in-medium speed of light, the particle will lose its energy by radiating photons (Cherenkov radiation). The acoustic Cherenkov effect is the acoustic analog of the optical Cherenkov effect in which the particle travelling faster than the speed of sound c_s loses energy by shredding phonons. In principle both charged and uncharged particles will be able to produce “Cherenkov phonons” if their speeds are high enough [161]. However in a typical DM scattering event the recoiling energy is not sufficiently high to make this happen ($v_{\text{recoil}} \sim 10 \text{ m/s}$ versus $c_s \sim 1000 \text{ m/s}$). We can increase the speeds of the electron-hole pairs by applying a voltage across the substrate which accelerates the charges and thus induce shredding of phonons. These additional phonons generated by accelerating the ionization charges are called NTL phonons.

The total phonon energy generated is given by

$$E_{ph}(\omega) = E_R + n(\omega)V \quad (3.8)$$

$$= E_R \left(1 + \frac{Y(\omega)}{\epsilon_{eh}(\omega)} V \right) \quad (3.9)$$

where V is the voltage applied across the substrate for producing the NTL amplification, also called the bias voltage. For SuperCDMS detectors operating in the high-voltage mode the bias voltage can go to as high as 100V. Thus the phonon energy is significantly boosted for events that produce any charge at all.

In solids the transverse speed of sound is usually significantly lower than the longitudinal speed of sound, e.g. in silicon the transverse speed of sound is 5340 m/s versus the longitudinal speed of sound which is around 9000 m/s. This leads to the interesting consequence that the NTL phonons are predominately transverse phonons [177]. This could be utilized for event identification in the future if we have phonon sensors with single-phonon resolution. We will revisit this in section 3.4.2.

3.4 Phonon Transport

Not all phonons that are generated can necessarily reach our sensors as phonons can decay and be scattered by point defects as well as the boundary of the substrate and thermalize before reaching the sensors on the surface. Understanding the transport of phonon across the substrate as well as across the material interface between the substrate and the phonon sensor (usually made of aluminium and tungsten) is thus important in order to properly model the final resolution of the

detector.

In this section we will first introduce the **Callaway model** of phonon mean free path that will allow us to estimate how far our phonons can travel in the substrate. Then we will introduce the **acoustic mismatch model** for surface resistance that will allow us to estimate how much phonons will be able to cross the material interface between the substrate and the sensor. We will combine the two model to estimate the overall phonon collection efficiency of our detector.

3.4.1 Callaway Model

As a high frequency phonon is travelling through the substrate it can undergo various types of physical processes that leads to partial loss of energy or decaying/splitting into lower frequency phonons. The phonon mean free path ℓ is the average distance that the phonon can travel without losing any energy via any of these processes.

Callaway presented a rather comprehensive and easy to use model of the phonon mean free path ℓ (or equivalently the scattering rates τ^{-1}) that takes into account the most important phonon scattering processes: [31, 78]

Anharmonic Decay The inter-atomic force in the lattice system does not actually strictly follow that of an ideal spring and can generate cubic couplings in the phonon Hamiltonian. This allows for the possibility for a single phonon to decay into two phonons (**Normal process**), and vice versa. Sometimes the crystal as a whole can also be involved in this scattering (**Umklapp process**) which results in a slightly different momentum conservation condition. In any case the original phonon now becomes two new phonons and each carries part of the original energy. Note that kinematically this process can only proceed for longitudinal phonon into a longitudinal phonon plus a transverse phonon ($L \rightarrow L+T$) or into two transverse phonons ($L \rightarrow T+T$). Thus the phonons produced via NTL effect which are predominately transverse are protected against this kind of decay, especially at very low temperature.

The rate is given by

$$\tau_N^{-1} = A_N \omega^n T^m \quad (3.10)$$

$$\tau_U^{-1} = A_U \omega^p T^r e^{-T_D/\alpha T} \quad (3.11)$$

where A_N , A_U , α are phenomenological parameters, n, m, p, r are fitted integers, T_D is the Debye temperature of the material, ω is the energy of the initial phonon and T is the temperature.

Point Defect Scattering Even in very high-purity crystals there are a small amount of isotopic impurity or other types of point defects. These point defects act as scattering centers as phonons propagate through the crystal and the rate is given by

$$\tau_{pd}^{-1} = A_{pd}\omega^4 \quad (3.12)$$

where A_{pd} is a parameter related to the concentration of point defects and isotropic impurities as well as the difference of their effective masses from the normal atomic mass [78].

Boundary Scattering If the substrate is pure and at a very low temperature it becomes likely that the phonons will be able to reach the boundary of the substrate before scattering via the above processes (unless the dimensions of the substrate is excessively large). In this situation then the boundary scattering will dominate the rate and becomes the limiting factor of the mean free path of the phonon. We can model the rate by

$$\tau_b^{-1} = \frac{c_s}{L} \frac{1 - P}{1 + P} \quad (3.13)$$

where c_s is the speed of sound, L is an effective dimension of the substrate and P is the probability of specular reflection ($P = 1$ means the phonon does not lose any energy, and $P = 0$ means that phonons reflect diffusively and thermalize at the boundary). The probability can be further parametrized by

$$P = \exp \left[- \left(\frac{2\eta_{\text{eff}}\omega}{c_s} \right)^2 \right] \quad (3.14)$$

where η_{eff} is an effective surface roughness parameter [78].

The above scattering rates can be combined to give the thermal conductivity via

$$\kappa = GT^3 \left(\langle \tau_C \rangle + \frac{\langle \tau_C / \tau_N \rangle^2}{\langle \tau_C / (\tau_N \tau_R) \rangle} \right) \quad (3.15)$$

where $G = \frac{k_B^4}{2\pi^2 \hbar^3 c_s}$, $\tau_C^{-1} = \tau_N^{-1} + \tau_R^{-1}$ and $\tau_R^{-1} = \tau_U^{-1} + \tau_b^{-1} + \tau_{pd}^{-1}$. The angled bracket denotes the following operation:

$$\langle f \rangle = \int_0^{T_D/T} \frac{x^4 e^x}{(e^x - 1)^2} f(x) dx \quad (3.16)$$

where $x = \frac{\hbar\omega}{k_B T}$.

At very low temperatures ($T \rightarrow 0$), an approximate expression can be obtained (to leading order

in T and assuming $P = 0$) [31]:

$$\kappa = \frac{2k_B\pi^2}{15} \frac{L^2}{c_s^2} \left(\frac{k_B T}{\hbar} \right)^3 \left[1 - \left(\frac{2\pi k_B T}{\hbar} \right)^4 \frac{A_{pd} L}{c_s} \right] \quad (3.17)$$

$$\sim c_s^{-2} \quad (3.18)$$

Once we have the thermal conductivity, we can relate it back to the mean free path via a simple relation [16]:

$$\kappa = \frac{1}{3} C_V c_s \ell \quad (3.19)$$

where C_V is the volume specific heat of the material and c_s is the speed of sound averaged over directions and modes.

In the Debye model we have the specific heat $C_V \sim c_s^{-3}$, thus from equation 3.18 we have $\ell \sim c_s$. In other words a higher speed of sound will in general lead to a longer mean free path (bounded by size and surface quality of the substrate).

3.4.2 Interface Matching

To be detected by our phonon sensor the phonons also need to be able to cross the interface between the substrate material (e.g. silicon) and the sensor material (e.g. aluminium or tungsten). Any interface that separates two mediums with different speeds of sound would reflect and/or refract passing phonons. We can model this using an analog to geometric optics. The resultant model is called the **Acoustic Mismatch Model** (AMM) [87] which we shall present in this section.

An exemplary situation is illustrated by figure 3.3. An longitudinal wave is propagating in the $x - z$ plane with the interface between medium 1 and medium 2 situated along the x -axis. The incoming wave can be reflected and refracted into both longitudinal and co-planar transverse mode (but not the transverse mode parallel to y -axis). The various angles are related via laws of geometric optics. For example, we have

$$\frac{\sin \theta_1}{c_{l1}} = \frac{\sin \theta_2}{c_{l2}} = \frac{\sin \gamma_1}{c_{t1}} = \frac{\sin \gamma_2}{c_{t2}} \quad (3.20)$$

where c denotes the speed of sound with subscripts denoting the polarization and the medium. We assume isotropy and do not include any angular dependence in the speed of sounds.

In order to calculate the transmission coefficient we assume all our waves are plane waves with

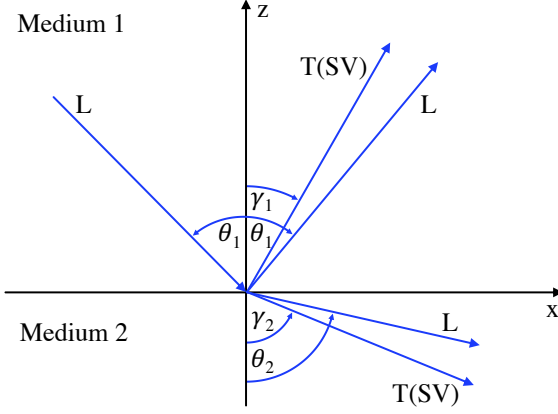


Figure 3.3: An incident longitudinal (L) acoustic wave is both reflected and refracted into longitudinal and transverse (SV) modes in the two media. The various angles here satisfy geometric-optical relations such as law of reflection and Snell's law. Reproduced from [87].

various amplitudes. For example the incident wave can be written as

$$v_{inc} = B \exp(i\mathbf{k}_{inc} \cdot \mathbf{r}) = B \exp(-i\beta z + i\sigma x) \quad (3.21)$$

where v_{inc} denotes the velocity of the oscillating nuclei due to the incident acoustic wave, B is the amplitude of the incident wave, $\beta = \omega/c_{l1} \cos \theta_1$ and $\sigma = \omega/c_{l1} \sin \theta_1$.

We can relate the various amplitudes using 4 boundary conditions:

1. The sum of normal (tangential) components of the velocities at the boundary should be continuous:

$$v_{1\perp} = v_{2\perp}, v_{1\parallel} = v_{2\parallel} \quad (3.22)$$

2. The sum of normal (tangential) components of the mechanical stress at the boundary should be continuous:

$$\rho_1 c_1^2 \frac{\partial v_1}{\partial z} = \rho_2 c_2^2 \frac{\partial v_2}{\partial z}, \text{etc.} \quad (3.23)$$

Writing these boundary conditions and combining with Eqs. 3.20 and 3.21 would produce a system of linear equations for the various amplitudes which can be solved to obtain the transmission coefficient η as a function of incident angle. The phonon transmission probability n across the

boundary is then defined as the angular average of the transmission coefficient:

$$\begin{aligned} n &= \int_0^{\pi/2} \eta(\theta_1) \sin(2\theta) d\theta \\ &= \int_0^{\theta_c} \eta(\theta_1) \sin(2\theta) d\theta \end{aligned}$$

where θ_c is the critical angle. For detailed derivation see the appendix of [87].

Table 3.1 contains a collection of transmission probabilities calculated in this manner.

Substrate	Si			Diamond			Ge			3C-SiC			4H/6H-SiC		
	n_l	n_t	\bar{n}	n_l	n_t	\bar{n}	n_l	n_t	\bar{n}	n_l	n_t	\bar{n}	n_l	n_t	\bar{n}
Sensor Material															
Al	0.98	0.89	0.91	0.72	0.63	0.65	0.61	0.83	0.72	0.85	0.95	0.94	0.86	0.82	0.83
Al ₂ O ₃	0.76	0.61	0.64	0.96	0.88	0.90	0.40	0.22	0.31	0.90	0.32	0.35	0.95	0.97	0.96
Diamond	0.30	0.11	0.15	1.00	1.00	1.00	0.13	0.05	0.09	0.42	0.06	0.08	0.61	0.29	0.34
Ga	0.97	0.89	0.90	0.67	0.58	0.61	0.92	0.83	0.87	0.84	0.90	0.89	0.84	0.79	0.80
Ge	0.90	0.83	0.84	0.90	0.82	0.84	1.00	1.00	1.00	0.87	0.90	0.89	0.94	0.91	0.91
In	0.97	0.89	0.90	0.68	0.59	0.61	0.92	0.83	0.88	0.88	0.90	0.90	0.86	0.79	0.80
Ir	0.47	0.36	0.38	0.84	0.76	0.78	0.63	0.54	0.58	0.63	0.37	0.38	0.70	0.55	0.58
Nb	0.83	0.74	0.75	0.93	0.85	0.87	0.89	0.94	0.92	0.92	0.86	0.86	0.97	0.88	0.89
Si	1.00	1.00	1.00	0.79	0.71	0.73	0.45	0.32	0.39	0.86	0.48	0.51	0.89	0.85	0.85
Sn	0.94	0.85	0.86	0.84	0.76	0.78	0.98	0.89	0.93	0.90	0.87	0.87	0.94	0.89	0.89
Ta	0.65	0.54	0.56	0.95	0.87	0.89	0.79	0.76	0.77	0.80	0.58	0.59	0.88	0.76	0.78
Ti	0.95	0.90	0.91	0.86	0.77	0.79	0.75	0.98	0.86	0.91	0.95	0.95	0.95	0.89	0.90
W	0.51	0.41	0.43	0.88	0.80	0.82	0.68	0.62	0.65	0.67	0.42	0.44	0.75	0.61	0.64
Zn	0.91	0.81	0.82	0.90	0.81	0.83	0.98	0.96	0.97	0.89	0.87	0.87	0.95	0.90	0.90

Table 3.1: Phonon transmission probabilities for phonons in different substrates (top row) crossing into various materials. The probability n_l (n_t) is the probability for a longitudinal (transverse) phonon incident on the interface from the substrate to get into a region made of another material (leftmost column). \bar{n} is the probability averaged by the density of states of the two modes. Note that the probability is not symmetric between two materials, e.g. the probability for a phonon in silicon crossing into germanium (0.84) is very different from that for a phonon in germanium crossing into silicon (0.39).

One interesting feature of the transmission probabilities $n_{l,t}$ is that they exhibit **mode selectivity**. For example, an titanium film on germanium substrate will preferentially absorb more transverse ($n_t = 0.98$) than longitudinal ($n_l = 0.75$) phonons, while a iridium film will preferentially absorb more longitudinal ($n_l = 0.63$) than transverse ($n_t=0.54$).

We can fabricate a germanium device where half of the sensors have titanium films as phonon absorbers and half of the sensors have iridium films instead. This potentially will allow us to not only reconstruct the total phonon energy E_{ph} , but also the transverse phonon energy E_T and longitudinal phonon energy E_L separately via

$$E_{\text{ph}} = E_L + E_T \quad (3.24)$$

$$E_{\text{Ti}} = 0.75 \times E_L/2 + 0.98 \times E_T/2 \quad (3.25)$$

$$E_{\text{Ir}} = 0.63 \times E_L/2 + 0.54 \times E_T/2 \quad (3.26)$$

$$(3.27)$$

where E_{Ti} is the energy collected by the titanium films and E_{Ir} is the energy collected by the iridium films. Here we assume that the geometry is symmetric between the two types of sensors so there is an equal (1/2) chance that any phonon will hit either sensor type.

For processes that are indifferent to the phonon mode, the mode of the phonon produced will follow the equilibrium mode distribution which is usually around 90% transverse and 10% longitudinal phonons [141]. We can define the **mode ratio** ξ as

$$\xi = \frac{E_L}{E_T} \approx 0.1 \quad (3.28)$$

However as we have pointed out before, phonons emitted via acoustic Cherenkov effects (e.g. NTL phonons, crowdion-emitted phonons) are predominately transverse due to the significantly lower transverse speed of sound. Therefore when these effects are present, we will have a significantly higher proportion of transverse phonons and ξ will become very close to zero. For the case of NTL amplification, this can potentially be as an additional way to discriminiate nuclear recoil and electron recoil as in electron recoil much more energy is deposited into ionization which is then converted to transverse phonons via NTL effect. For the case of crowdion emission, we can detect the presence of crowdion by looking at the mode ratio which in turn will give us information on the **direction** of the incoming DM particle because crowdions are usually produced only when the incoming DM particle hit the crystal along particular axes of symmetry [123]. The ability to separate phonon modes translates into **ER/NR discrimination** and **direction reconstruction**.

3.4.3 Phonon Collection Efficiency

Let us now put together the results from the previous sections and estimate the overall phonon collection efficiency from production at primary interaction site to getting into sensor material on the surface.

The phonon lifetime τ_{life} can be estimated from the mean free path ℓ via a simple conversion:

$$\tau_{\text{life}} = \ell/c_s \quad (3.29)$$

where c_s is the average speed of sound.

The time constant for phonon collection at the sensor interface is given by [71]

$$\tau_{\text{collection}} = \frac{4V_{\text{crystal}}}{Ac_s\bar{n}} \quad (3.30)$$

where V_{crystal} is the volume of the crystal, A is the surface area of the sensor or phonon absorber, c_s is the average speed of sound and \bar{n} is the transmission probability across the crystal-sensor interface. If there are multiple different sensor materials then the denominator is summed over all materials present.

The phonon can either decay and become thermalized, or get absorbed into the sensor. The portion that gets absorbed into the sensor, which is the efficiency we want to calculate, is given by

$$\eta_{\text{collection}} = \frac{\tau_{\text{life}}}{\tau_{\text{life}} + \tau_{\text{collection}}} \quad (3.31)$$

$$= \frac{A\bar{n}\ell}{A\bar{n}\ell + 4V} \quad (3.32)$$

$$= \frac{\rho_{\text{coverage}}\bar{n}\ell}{\rho_{\text{coverage}}\bar{n}\ell + 4h} \quad (3.33)$$

where in the last equality we divide by the surface area of the crystal A_{crystal} , $\rho_{\text{coverage}} = A/A_{\text{crystal}}$ is the sensor coverage percentage and $h = V_{\text{crystal}}/A_{\text{crystal}}$ is the volume-to-area ratio (“thickness”) of the crystal. Thus to optimize collection efficiency, we want large sensor area/coverage, long phonon mean free path, acoustically well-matched (high \bar{n}) material, and small substrate.

For **quasi-particle assisted transition-edge sensors** (QET), which are the standard sensors for SuperCDMS detectors, the phonons collected are supposed to break Cooper pairs in the absorber (usually aluminium fins) and create quasi-particles. The quasi-particles traverse the absorbed and finally get trapped in the main body of the transition-edge sensor (usually tungsten) which produces the signal. Thus the overall efficiency needs to include the quasi-particle conversion and collection efficiencies as well:

$$\eta = \eta_{\text{collection}} \times \eta_{\text{conversion}} \times \eta_{\text{trapping}} \quad (3.34)$$

From past experiments it is estimated that $\eta_{\text{conversion}}$ is approximately 52% and η_{trapping} is approximately 62% [101] for SuperCDMS-style detectors. Thus the upper limit for the overall efficiency is around 32%. We will delve into the quasi-particle trapping efficiency a little deeper in the next section.

3.5 Sensor Physics

We now turn our focus to the physics of the phonon sensors. In SuperCDMS detectors we use a type of thermal sensor called **quasi-particle assisted transition-edge sensor** (QET). The main goal of this section is to give a pedagogical presentation of the conceptual development of QET, starting from the most basic thermal sensor and gradually adding additional various components.

3.5.1 Calorimetry

The main advantage of using thermal sensor (calorimeter) is that unlike in e.g. charge sensors, there is no fundamental physical limit to the energy resolution of an ideal thermal detector.

As an example, let us consider an ionization detector made of silicon. Assuming all energy goes into creation of electron-hole pairs, the number of electrons N generated by an energy deposit E is given by the simple relation $N = E/\varepsilon$, where ε is the energy needed to create a single electron-hole pair. The variance ΔN is given by

$$\Delta N = \sqrt{FN} \quad (3.35)$$

where F is the Fano factor of the material. Converting to energy, we obtain the following fundamental limit in the energy resolution:

$$\Delta E = \varepsilon \Delta N = \sqrt{\varepsilon EF} \quad (3.36)$$

For silicon, this corresponds to an energy resolution of around 110 eV FWHM at $E=6$ keV. On the other hand, TES-based thermal sensors can achieve 2 eV FWHM resolution for the same energy [126, 124], which is orders of magnitude beyond the Fano limit.

To understand how thermal sensors is able to achieve such seemingly impossible energy resolution, let us now consider a simple thermal detector model. We will show that such detectors are

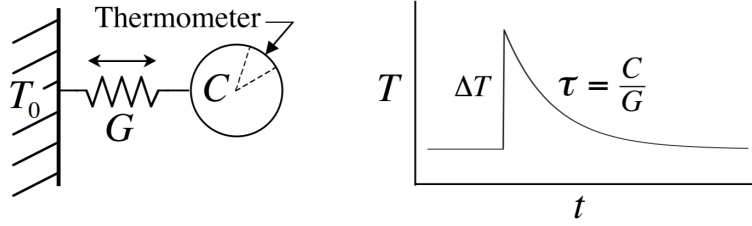


Figure 3.4: Model of a simple calorimeter. Any energy deposit will result in an exponential pulse will decay time $\tau = C/G$.

bandwidth-limited and in principle have no intrinsic limit in energy resolution.

The simplest set-up for a thermal detector is a calorimeter that consists of an absorber, in which the incoming energy is deposited, and a thermometer which reads the temperature of the absorber. The absorber is weakly coupled to a thermal bath at some fixed temperature T_b so that it can recover to its initial state over time.

By energy conservation, we have the following equation for the temperature T of the detector:

$$P = G(T - T_b) + C \frac{dT}{dt} \quad (3.37)$$

where P is the power absorbed by the absorber, G is the thermal conductance between the absorber and the thermal bath and C is the heat capacitance of the detector.

For an instantaneous energy deposit we have $P = E_0 \delta(t)$, the solution is given by

$$T = \begin{cases} Ae^{-t/\tau} + T_b & t > 0 \\ T_b & t < 0 \end{cases} \quad (3.38)$$

where $\tau = C/G$. The amplitude can be obtained by integrating equation 3.37 in the vicinity of the origin:

$$\begin{aligned} E_0 &= \int_{0^-}^{0^+} P dt = C(T(0^+) - T(0^-)) = CA \\ A &= E_0/C \end{aligned} \quad (3.39)$$

We can also solve for the temperature of the detector in bolometer mode, i.e. the case where

$P = \text{const.}:$

$$T = \frac{P\tau}{C}(1 - e^{-t/\tau}) + T_b \quad (3.40)$$

Thus the temperature shifts from T_b to a new baseline determined by the added power with the same time constant τ .

In thermal detectors, instead of Fano noise our intrinsic noise is due to thermal fluctuation, which can be derived using the canonical ensemble assuming the detector is in equilibrium with the bath:

$$(\Delta E)^2 = \langle E^2 \rangle - \langle E \rangle^2 \quad (3.41)$$

$$= \frac{\sum_i E_i^2 e^{-E_i/k_B T_b}}{Z} - \left(\frac{\sum_i E_i e^{-E_i/k_B T_b}}{Z} \right)^2 \quad (3.42)$$

$$= \frac{1}{Z} \frac{\partial^2 Z}{\partial \beta^2} - \left(\frac{1}{Z} \frac{\partial Z}{\partial \beta} \right)^2 \quad (3.43)$$

$$= \frac{\partial}{\partial \beta} \left(\frac{1}{Z} \frac{\partial Z}{\partial \beta} \right) \quad (3.44)$$

$$= -\frac{\partial E}{\partial \beta} \quad (3.45)$$

$$= k_B T_b^2 \frac{\partial E}{\partial T} \quad (3.46)$$

$$= k_B T_b^2 C \quad (3.47)$$

However, unlike Fano noise this **thermal fluctuation noise** (TFN) does not fundamentally limit the energy resolution of our detector. The reason being that the rise of the temperature pulse is infinitely sharp and thus if our ability to “zoom in” on the onset of the pulse is unlimited, we will always be able to resolve the pulse amplitude from the background fluctuation (see figure 3.5).

This can be seen more quantitatively by going to the frequency domain. Let $\mathcal{T} = T - T_b$. The Fourier transform of equation 3.37 can be written as

$$\begin{aligned} i\omega \tilde{\mathcal{T}} &= \frac{\tilde{P}}{C} - \frac{\tilde{\mathcal{T}}}{\tau} \\ \tilde{\mathcal{T}} &= \frac{\tilde{P}/G}{1 + i\omega\tau} \end{aligned} \quad (3.48)$$

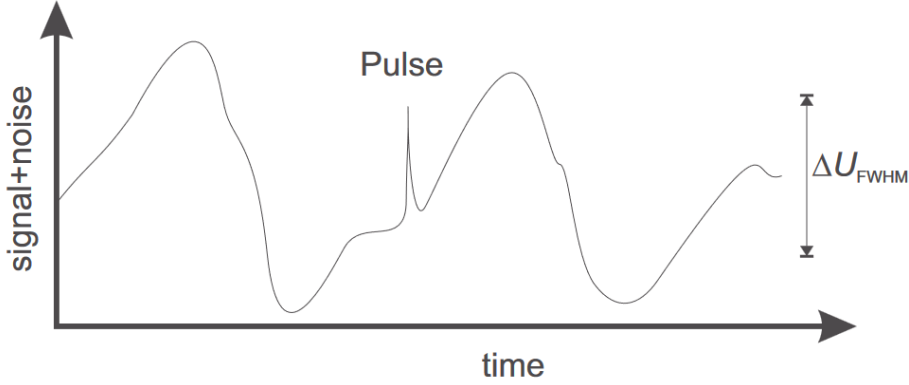


Figure 3.5: Figure taken from [110]. Electrothermal feedback in microcalorimeter can cause energy pulses to be significantly shorter than typical timescale of thermal fluctuation in the sensor. Thus with sufficient bandwidth the energy resolution of the microcalorimeter is not limited by the thermal fluctuation noise.

The signal spectral density is given by the modulus:

$$S_{\text{signal}}(\omega) = |\tilde{\mathcal{T}}|^2 = \frac{(E_0/G)^2}{1 + \omega^2\tau^2} \quad (3.49)$$

Note that the spectrum extends indefinitely to arbitrarily high frequencies. Thus in principle we can measure an infinite number of frequency bins to obtain an arbitrarily fine energy measurement.

To see that this is indeed the case, we compare the signal power to intrinsic noise power due to random thermal fluctuation, which is referred to as **thermal fluctuation noise** (TFN). Physically the TFN can be interpreted as power fluctuations due to random phonon exchange across the thermal conductance. The noise spectral density is then given by the fluctuation-dissipation theorem [165]:

$$\begin{aligned} S_{\text{TFN}}(\omega) &= \frac{4\langle \mathcal{T}^2 \rangle C/G}{1 + \omega^2\tau^2} \\ &= \frac{4k_B T_b^2 / G}{1 + \omega^2\tau^2} \end{aligned} \quad (3.50)$$

where we have used equation 3.47 to obtain $\langle \mathcal{T}^2 \rangle = (\Delta T)^2 = k_B T_b^2 / C$. Note that this expression is only valid when the temperature of the detector doesn't deviate too much from the equilibrium, otherwise the expression needs to be modified by some multiplicative factor [119].

In any case the signal and the noise spectra have exactly the same shape and the signal-to-noise ratio is constant across all frequency bins. The situation is illustrated in figure 3.6.

In practice, of course, this is not the whole story - our readout bandwidth is always finite,

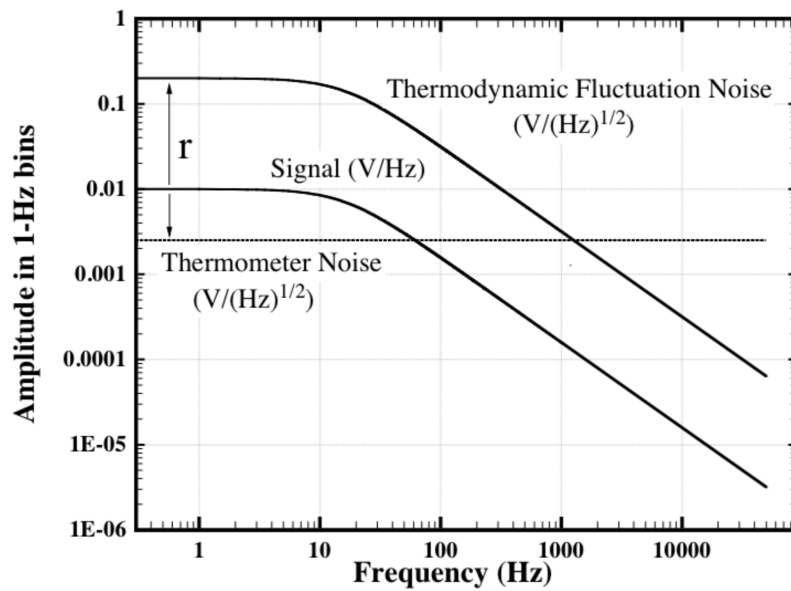


Figure 3.6: Power spectrum of the signal and TFN for a simple thermal detector. The TFN and the signal are in different units. Note that they have the same shape and thus the energy resolution is only constrained by bandwidth-limiting noise, such as the thermometer white noise (dotted) illustrated here.

and there will be other noise sources from our set-up. Additionally, if the energy is not absorbed instantaneously or the thermalization time of the thermometer is not negligible, the temperature pulse will have a rise time and the signal power will fall off faster than noise.

In fact let us see how the energy resolution scales with the bandwidth. The OF resolution is given by the ratio of the noise spectrum to the template (signal when $E_0=1$) spectrum via (see Appendix B)

$$\sigma_E^2 = \left[\int_0^{f_{\max}} \frac{S_{\text{signal}}}{S_{\text{TFN}}} df \right]^{-1}$$

Evaluating gives

$$\sigma_E^2 \propto \frac{k_B T^2 G}{f_{\max}} = \frac{(\Delta E)^2}{f_{\max} \tau} \quad (3.51)$$

where $\Delta E = k_B T^2 C$ is the thermodynamic energy fluctuation. Again one can see that the energy resolution will become arbitrarily small if f_{\max} is unbounded. In this scenario our detector is bandwidth-limited.

3.5.2 Electrothermal Feedback

The thermometer is implemented by measuring some temperature-dependent property of the thermometer, with the most common choice being the electrical resistance which leads to what is called a **thermistor**.

At first glance the thermistor seems to be a bad candidate for the thermometer in our calorimeter. It adds additional white noise (Johnson noise) as well as additional power dissipation which heats up the detector to create even more TFN. However, we will see that power dissipation from the thermistor actually provides a feedback mechanism that significantly improves the performance of the detector. This **electrothermal feedback** (ETF) is essential to the performance of TES.

With the addition of the resistive heating term, the power balance equation becomes

$$P + P_R = G(T - T_b) + C \frac{dT}{dt} \quad (3.52)$$

where P_R is the power due to resistive heating. We can write P_R in one of the two forms, depending on whether we keep the voltage or the current constant across our thermistor:

$$\text{Current-biased: } P + I^2 R(T) = G(T - T_b) + C \frac{dT}{dt} \quad (3.53)$$

$$\text{Voltage-biased: } P + V^2/R(T) = G(T - T_b) + C \frac{dT}{dt} \quad (3.54)$$

Let us further assume for the time-being that the resistance is a simple linear function in temperature $R(T) = AT + R_c$. The current-biased case will result in a device that is very difficult to operate because any rise in temperature will lead to an increase in the Joule heating and further warm up the detector, causing a thermal runaway. We can see this more clearly by inspecting equation 3.53 for $P = 0$:

$$C \frac{dT}{dt} = (AI^2 - G)T + I^2 R_c + GT_b \quad (3.55)$$

We see that this has two immediate effect. First the baseline or the quiescent temperature is now no longer equal to T_b but shifted to (by setting $dT/dt = 0$) $T_0 = \frac{I^2 R_c + GT_b}{G - AI^2}$. Note that if $G < AI^2$, this temperature is negative and so the detector will never reach thermal balance and will warm up indefinitely. Second, assuming the system does not run away, the time constant of the temperature pulse becomes $C/(G - AI^2)$, which leads to a slower response and thus limits the performance of the detector. Both of these disadvantages disappear when we switch to voltage bias, which is the standard practice nowadays.

The equation for the voltage-biased case is more difficult to solve due to the awkward $1/R$ term. We proceed by linearizing around the quiescent temperature:

$$\begin{aligned} P + \frac{V^2}{R_0} \left(1 - \frac{A}{R_0} \mathcal{T}\right) &= G(T_0 - T_b) + G\mathcal{T} + C \frac{d\mathcal{T}}{dt} \\ P &= G\mathcal{T} + \frac{AV^2}{R_0^2} \mathcal{T} + C \frac{d\mathcal{T}}{dt} \end{aligned} \quad (3.56)$$

where $R_0 = R(T_0)$ and $\mathcal{T} = T - T_0$.

The quiescent temperature is given by a quadratic equation:

$$\begin{aligned} AGT_0^2 + GR_c T_0 - (V^2 + GT_b) &= 0 \\ T_0 = -\frac{R_c}{2A} \pm \sqrt{\left(\frac{R_c}{2A}\right)^2 + \frac{V^2 + GT_b}{AG}} \end{aligned} \quad (3.57)$$

We see that there is always a real positive solution as long as A is positive. Thus by voltage biasing we not only avoid the issue of thermal runaway but also obtain a faster response time $\tau_{\text{eff}} = C/(G + AV^2/R_0)$.

What about the energy resolution? At first glance it seems that the faster response time might lead to worse energy resolution (equation 3.51). However, the ETF in fact also suppresses the wide-band Johnson noise which in turn increases the maximum bandwidth f_{\max} . Thus the overall

energy resolution is actually improved by strong ETF. This can be seen from equation 3.56. If we write $P_0 = V^2/R_0$ and assume $G \ll AP_0/R_0$ so we can drop the $G\mathcal{T}$ term, we have

$$\tilde{P} = \frac{AP_0}{R_0}(1 + i\omega\tau_{\text{eff}})\tilde{\mathcal{T}}$$

Now the Johnson noise is given by $\tilde{P} = I_0\tilde{V} = I_0\sqrt{4k_B T_0 R_0}$. Thus the Johnson temperature noise $S_{\text{Johnson}} = \langle \mathcal{T}^2 \rangle$ is suppressed by $1/A^2$. The overall scaling in energy resolution ΔE is given by $1/\sqrt{A}$ (equation 3.51) since f_{\max} scales as A^2 and the τ is proportional to $1/A$.

3.5.3 Transition Edge Sensor (TES)

We see that strong ETF provides many benefits in the previous section. Thus we should look for resistances with very steep temperature dependence. The most ideal candidate is superconductor at the transition edge which to zeroth order should have $A = \infty$. Thermal detectors utilizing the sharp transition edge of superconductors are called Transition Edge Sensors (TES).

In the transition region the TES can be thought of as a weak-link or a Josephson junction ($SS'S$). The resistance across the TES is thus function of both temperature and current. Two popular models for $R_{\text{TES}}(I, T)$ are the two-fluid model and the RSJ model [23]:

$$R_{\text{two-fluid}}(I, T) = c_R R_n \left[1 - c_I \frac{I_c(T)}{I} \right] \quad (3.58)$$

$$R_{\text{RSJ}}(I, T) = R_n \left[1 - \left(\frac{I_c(T)}{I} \right)^2 \right]^{1/2} \quad (3.59)$$

where c_R and c_I are the resistive fraction and the super-fluid fraction respectively, and R_n is the normal resistance. $I_c(T)$ is the critical current which is a function of temperature. In Ginzburg-Landau theory the critical current near the transition is described by

$$I_c(T) = I_{c0} \left(1 - \frac{T}{T_c} \right)^{3/2} \quad (3.60)$$

Since now we have two independent variables (I,T) instead of one, we need an additional equation other than equation 3.56. This comes from analyzing the TES circuit (figure 3.7). The system of equations then becomes

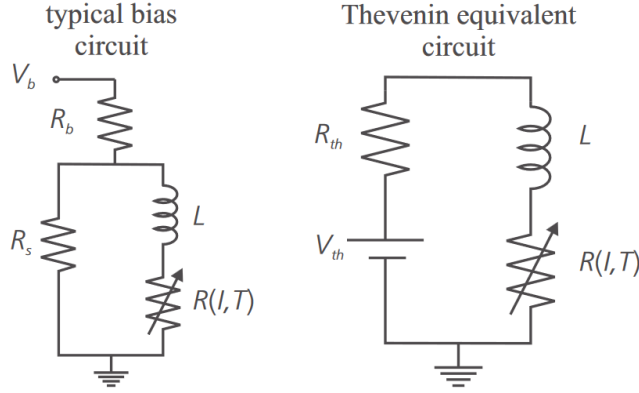


Figure 3.7: Figure taken from [110]. Typical TES circuit including bias resistance R_b , shunt resistance R_s and the readout inductance L (usually coupled to a SQUID amplifier). The shunt resistance is usually chosen to be small compared to the operating resistance of the TES to ensure that the TES is operating in the voltage-biased regime.

$$L \frac{dI}{dt} = V_{th} - I(R_{th} + R(I, T)) \quad (3.61)$$

$$C \frac{dT}{dt} = -P_{\text{bath}} + I^2 R(I, T) + P \quad (3.62)$$

where $P_{\text{bath}} = G(T - T_b)$ is power flow to the absorber. In practice we usually lock the operating point of the TES via a negative feedback loop, as such it is usually sufficient to analyse the behavior of the TES near a small neighborhood of the operating point (also called quiescent point) using the linearized version of the above equations [101]:

$$L \frac{d\delta I}{dt} = \delta V - (R_{th} + (1 + \beta)R_0)\delta I - \frac{\alpha I_0 R_0}{T_0} \delta T \quad (3.63)$$

$$C \frac{d\delta T}{dt} = I_0 R_0 (2 + \beta) \delta I - \left(G - \alpha \frac{I_0^2 R_0}{T_0} \right) \delta T + \delta P \quad (3.64)$$

where we have substituted $R(I, T) \approx R_0 \left(1 + \alpha \frac{\delta T}{T_0} + \beta \frac{\delta I}{I_0} \right)$ and expand around the quiescent point (R_0, I_0, T_0) . For detailed analysis of the noise and dynamics of the TES, please refer to [110, 101, 141, 79]. The important result for our purpose is that the resolution is given by

$$\sigma_E^2 = \frac{2k_B T_c^2 G}{\eta^2} \left(\tau_{\text{pulse}} + \frac{2}{5} \tau_{\text{TES}} \right) \quad (3.65)$$

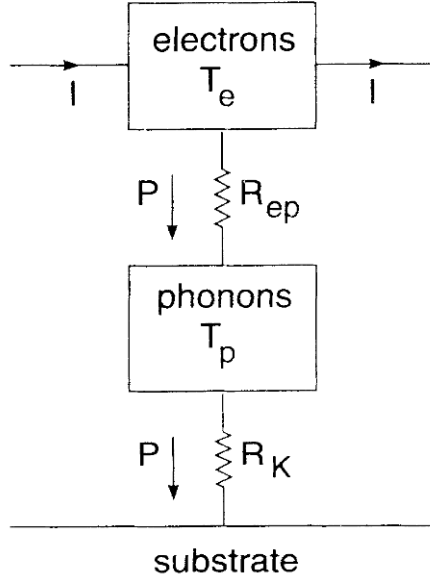


Figure 3.8: Figure taken from [168]. Current flowing through the TES due to the voltage bias keeps the electrons at an elevated temperature T_e that is different from the phonon temperature. The bias thermal power flows through the electron-phonon thermal conductance R_{ep} into the phonon system and then through the Kapitza resistance R_K between the sensor and the substrate into the substrate which acts as the thermal bath.

where η is the overall energy collection efficiency (equation 3.34), τ_{pulse} is the phonon collection time given by $\tau_{\text{pulse}}^{-1} = \tau_{\text{life}}^{-1} + \tau_{\text{collection}}^{-1}$ (equation 3.29 and 3.30) and $\tau_{\text{TES}} = \frac{C}{G\mathcal{L}}$ is the TES time constant with $\mathcal{L} = \frac{\alpha I_0^2 R_0}{GT_0}$. Again the TES time constant is shorter than C/G due to strong electrothermal feedback. The quantity \mathcal{L} is a dimensionless parameter called the loop gain and typically lies somewhere between 10 to 100.

3.5.4 Quasiparticle-Assisted TES (QET)

One subtlety that we have glanced over in the above discussion is that there are actually two separate temperatures in the TES - the electron temperature T_e and the phonon temperature T_p . The situation is illustrated in figure 3.8. The thermal power through the two resistances can be written as [168]:

$$P_{\text{ep}} = \Sigma V_{\text{TES}} (T_e^5 - T_p^5) \quad (3.66)$$

$$P_{\text{Kapitza}} = \sigma A_{\text{TES}} (T_p^4 - T_0^4) \quad (3.67)$$

The temperature T that we are measuring via change in electrical current I is the electron temperature T_e . Thus in our formulation of the TES dynamics all the variables are that of the electron system in the TES. The phonon system of the TES should be treated as part of the absorber or the thermal bath and thus

$$P_{\text{bath}} = P_{\text{ep}} = \Sigma V_{\text{TES}} (T_e^5 - T_p^5) \quad (3.68)$$

$$G = \frac{dP_{\text{bath}}}{dT_e} = 5\Sigma V_{\text{TES}} T_0^4 \quad (3.69)$$

where the second line gives G near the quiescent point.

From equation 3.65 we see that it is advantageous to have a small conductance G which means we want a TES with a small active volume V_{TES} . On the other hand, the same equation also tells us that we want a large phonon collection efficiency η and thus a large surface area A for coverage (equation 3.34). These criteria are in tension with each other. SuperCDMS solved this dilemma by the addition of phonon collection fins that are made of superconducting material with a much higher T_c , forming what is called a **quasi-particle assisted TES** (QET).

Figure 3.9 shows a side-view of a QET. The small TES volume is held at its transition temperature and is electrically active. The phonon collection fin (typically aluminium) has a much higher transition temperature. It stays in superconducting state and is thermally inactive. Thus the addition of the fin does not increase the active volume of the TES. However phonons entering into the fin are still able to be funneled into the TES via a process quasi-particle trapping. The incident phonons will break Cooper pairs in the fin and create quasi-particles. The quasi-particles diffuse along the fin and preferentially get trapped into the TES due to the difference in the energy gap. Upon recombination the energy in the quasi-particles will be converted back into phonons inside the TES. Effectively this increases the phonon collection area, while allowing the TES volume to stay small.

The dynamics of quasi-particle trapping is described in [146]. Intuitively we would expect the trapping effect would be stronger if we employ a large energy gap difference. However if the gap difference is too dramatic the trapping rate actually drops to zero (see figure 3.10). The optimal energy gap ratio is somewhere between 0.2 and 0.4 (such as aluminium and titanium). For a complete discussion on various considerations on optimization of the fin length and geometry please refer to [101, 141, 146]. Since our main goal is to optimize the substrate material we shall not delve into too much details of fin optimization which is itself a vast topic with a lot of room left for further research.

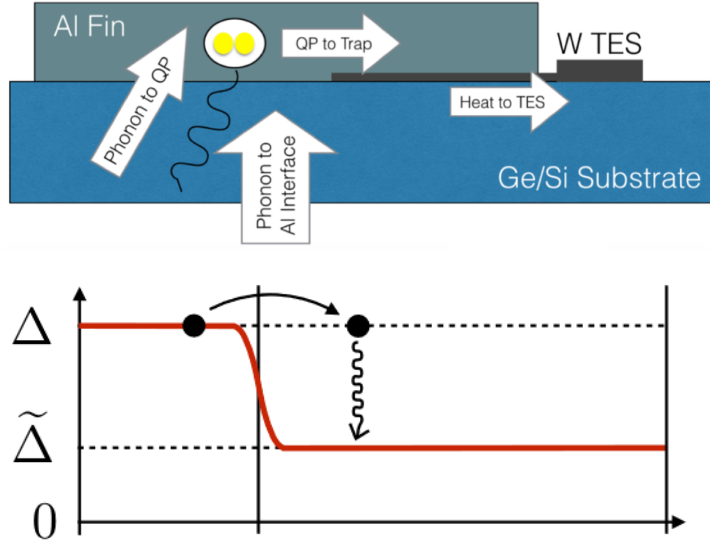


Figure 3.9: Illustration of a SuperCDMS QET. (top) Phonons entering the fin will generate quasi-particles that gets trapped in the lower energy-gap region created by the tungsten TES. Their energy gets converted back into phonons in the TES upon recombination. This effectively increases the phonon collection area, while maintaining a small active TES volume. (bottom) The variation of the energy gap across the junction. When the quasiparticle travels from a high gap (high T_c) material to a low gap (low T_c) material it loses energy and gets trapped in the low gap region.

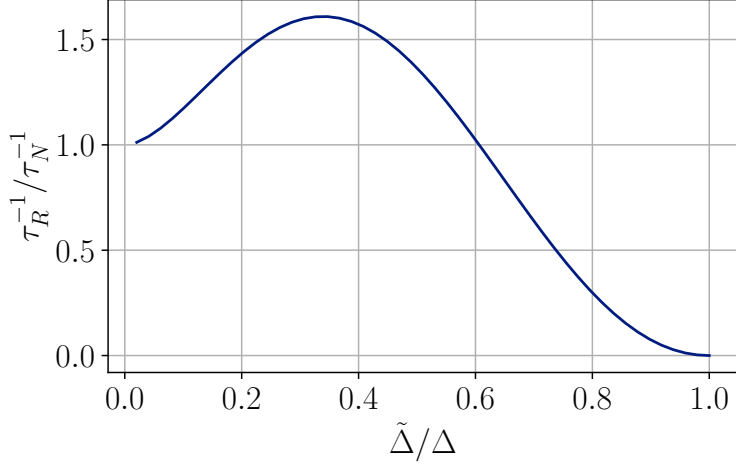


Figure 3.10: Quasi-particle trap rate as a function of energy gap ratio of the two regions. See [146] for details.

Chapter 4

Optimal Substrates for Direct Detection

Now that we have a good overall understanding of everything that affects the performance of the detector from the primary interaction in the substrate to phonon transport to sensor dynamics, we are ready to discuss specific materials and why their properties are ideal for DM detection in the context of energy resolution as well as other features. We will mainly focus on two broad classes of materials - carbon-based material (diamond and SiC) and heavy fermion material. The former is optimized towards nuclear recoil and phonon channels, while the latter is optimized towards electron transition.

4.1 Carbon-Based Material

From the previous chapters we have seen the criteria for optimizing the detection rate for nuclear recoil events in terms of the properties of the substrate:

1. Low nuclear mass for better kinematic matching
2. High speed of sound for better phonon collection efficiency and thus resolution

In terms of nuclear mass the lightest material we can use is obviously hydrogen and helium. However these are gaseous and liquid respectively at low temperatures and thus would require very different treatment than a solid substrate. They also do not have a high speed of sound. The next three elements in the periodic table - lithium, beryllium, and boron - are difficult to handle in terms of brittleness and material strength. Thus carbon is the best practical solid substrate we can use for

Parameter	Description	Diamond (C)	Si	Ge
Z	Atomic number	6	14	32
A	Average atomic mass	12.01	28.09	72.64
	Stable isotopes	12,13	28,29,30	70,72,73,74
	Natural radioactive isotopes	14	32	76
a (Å)	Lattice spacing	3.567	5.431	5.658
N (cm^{-3})	Number density	1.76×10^{23}	5×10^{22}	4.42×10^{22}
E_g (eV)	Bandgap Energy	5.47	1.12	0.54
ϵ_{eh} (eV)	Average energy per e^-h^+ pair	~ 13 [178]	3.6-3.8 [178, 7]	3.0 [7]
ϵ_r	Relative permittivity	5.7	11.7	16.0
Θ_{Debye} (K)	Debye temperature	2220	645	374
$\hbar\omega_{\text{Debye}}$ (meV)	Debye energy	190	56	32
$\hbar\omega_{\text{TO}}$ (meV)	Transverse optical phonon energy	141	59	-
$\hbar\omega_{\text{LO}}$ (meV)	Longitudinal optical phonon energy	163	63	37
c_s (m/s)	Average phonon speed	13360	5880	3550
$v_{d,sat}, e^-$ (m/s)	Electron saturation velocity	$\sim 2 \times 10^5$	1.35×10^5	1.2×10^5
E_{Bd} (MV/cm)	Dielectric breakdown field	> 20 [103]	0.3	0.1
ℓ (cm)	Phonon mean free path	25.6	11.4	6.9
τ_{life} (μs)	Phonon Lifetime	19.2	19.4	19.5
\bar{n}_W	Phonon Transmission (W)	80.6%	42.1%	62.6%
$c_s \bar{n}_W$ (m/s)	Effective speed (W)	10773	2473	2221
\bar{n}_{Al}	Phonon Transmission (Al)	63.7%	90.0%	80.9%
$c_s \bar{n}_{\text{Al}}$ (m/s)	Effective speed (Al)	8513	5290	2872

Table 4.1: *First and second sections:* material properties of diamond, Si, and Ge (from Refs. [82, 130, 80] unless otherwise stated). *Last section:* Phonon figures of merit in the three materials at low temperatures ($\lesssim 30\text{mK}$) for a mm-scale crystal. Transmission probabilities \bar{n} from substrate to tungsten (W) and aluminium (Al) are calculated from acoustic mismatch model in chapter 3.

DM detector. In additional, carbon, especially in the diamond form, also has the highest speed of sound among all solid elements. This makes it the perfect substrate for detection of nuclear recoil and phonon production events.

Table 4.1 summarizes all the relevant material properties of diamond compared to silicon and germanium. Apart from the low atomic mass and high speed of sound there are several other features worth noting. First of all is the high bandgap energy and the high dielectric breakdown field. The high bandgap energy means that the energy threshold for electron recoil is significantly higher. While this is not desirable for detecting low mass dark matter via electron recoil, it does imply a wider ER-free region in our energy spectrum where we do not need to worry about ER/NR discrimination. Furthermore the high breakdown field means that we can apply a significantly higher electric field across our substrate to achieve a very high NTL gain. This allows us to further widen the ER-free region in our spectrum and potentially achieve near perfect separation of ER and NR events. The high bandgap energy combined with the fact that diamond impurity levels are deep

with the bandgap [130] also means that we should expect a low dark current when operating at moderate voltages.

Secondly the phonon energy is high in diamond. This coupled with the fact that the energy resolution can potentially reach around or below 100 meV means that we can potentially make a single-phonon resolution detection based on diamond. This enables us to perform interesting studies such as phonon mode separation described in section 3.4.2 and look into previously unmeasured physics of phonon mode distribution and possibly soliton physics.

There are some potential drawbacks with diamond especially regarding to backgrounds. The efficacy for detecting low mass DM particle also translates to efficacy for detecting slow neutrons. The neutron scattering cross-section for thermal neutrons on carbon atoms is about 2.5 times higher than for silicon atoms [153]. This means that there will be both a higher rate and larger energy dispersion, making neutrons a more insidious background for carbon-based detectors. Helium, in comparison, has a 4 times lower cross section, despite having a higher energy transfer efficiency [65]. Detector housing and other support structures must be carefully assayed and designed to reduce this background to an acceptable level. It might also be able to perform background rejection via vetoing with neutron detectors or multiple diamond detectors forming an array.

Cosmogenic ^{14}C is another source of significant background. This isotope decays by β^- with a broad energy distribution with a mean energy of 48 keV and a maximum energy at 160 keV [8], with a half life of about 5700 years. The natural abundance of ^{14}C , around 1 part per trillion ($^{14}\text{C}/\text{C} \sim 10^{-12}$) [112], therefore implies an event rate of around 0.2 Hz/g. The vast majority of these events will be outside the energy range of interest; we only care about events with energies below about 100 eV, which will occur at a rate of about 100 $\mu\text{Hz}/\text{g}$, equivalent to about 10 events per gram-day. This concentration of ^{14}C would limit diamond detectors to gram-day exposures.

The ^{14}C concentration can be greatly reduced, however, by employing sources of carbon with a large overburden which prevents cosmogenic production of ^{14}C , which therefore have a much smaller abundance of the radioisotope. Underground sources of carbon, such as methane deposits, have been shown to have natural abundances of $^{14}\text{C}/\text{C} \sim 10^{-18}$, and mass spectroscopy methods promise to reduce the $^{14}\text{C}/\text{C}$ ratio even further, to $^{14}\text{C}/\text{C} \lesssim 10^{-21}$ [112]. These improved abundances would correspond to only about 10 events per kg-year and 1 event for 100 kg-years respectively, which allow for background-free searches for the exposures considered in this paper. Sourcing high-purity methane for the seed crystal of CVD diamond, it is likely that CVD diamonds with much lower than natural abundance of ^{14}C can be made.

An interesting way to circumvent the difficulties with cosmogenic and neutron backgrounds is to use silicon carbide as the substrate [61]. The advantage of silicon carbide lies in its polytypism (see figure 4.2). The high degree of anisotropy in the crystal structure translates into anisotropies into both the phonon and electron band structures. This allows us to perform directional detection

via e.g. daily modulation in the signal rate (figure 4.3) and thus circumvent the issue of having cosmogenic or neutron backgrounds which should have a steady event rate. Table 4.2 contains a summary of properties of various SiC polytypes.

Polytype	3C	8H	6H	4H	2H	15R
Crystal Structure	cubic		hexagonal		rhombohedral	
ρ (g cm ⁻³)			~3.2 [64, 27]			
N (10 ²³ cm ⁻³)			0.96			
n_e (10 ²³ cm ⁻³)			1.95			
$\hbar\omega_p$ (eV)			22.1[17]			
a (c) (Å)	4.36	3.07 (20.15)	3.08 (15.12)	3.07 (10.05)	3.07 (5.04)	3.07 (37.80)
E_g (eV)	2.39	2.7	3.02	3.26	3.33	3.0
ϵ_{eh} (eV)	~ 5.7 – 7.7 [†]	6.4 – 8.7 [†]	6.7 [105]	7.7 – 7.8 [81, 27]	7.8 – 10.5 [†]	7.1 – 9.6 [†]
E_{defect} (eV)	19 (C), 38 (Si)		22 (C)	22–35 [127]		17–30 (C)
$\epsilon_{0\perp}$	9.7		9.67	9.76		
$\epsilon_{0\parallel}$	9.7		10.03	10.32		
$\epsilon_{0\perp}^{[\text{calc}]}$	10.40	10.40	10.39	10.36	10.24	10.38
$\epsilon_{0\parallel}^{[\text{calc}]}$	10.40	10.80	10.90	11.06	11.41	10.96
$\epsilon_{\infty\perp}$	6.5		6.6	6.6	6.5	6.5
$\epsilon_{\infty\parallel}$	6.5		6.7	6.8	6.8	6.7
$\epsilon_{\infty,\perp}^{[\text{calc}]}$	7.07	7.10	7.11	7.10	7.03	7.11
$\epsilon_{\infty,\parallel}^{[\text{calc}]}$	7.07	7.31	7.36	7.41	7.40	7.38
Θ_{Debye} (K)	1430		1200	1200		
$\hbar\omega_{\text{Debye}}$ (meV)	122		103	103		
$\hbar\omega_{\text{TO}}$ (meV)	98.7		97.7, 98.8	97.0, 98.8	95.3, 99.0	98.9
$\hbar\omega_{\text{LO}}$ (meV)	120.5		119.7, 120.3	119.5, 120.0	120.0, 120.7	119.6
c_s (m/s)	12600		13300	13730		
c_s (m/s) ^[\text{calc}]	13200	16300	14300	14300	15500	11900
$v_{d,\text{sat}}, e^-$ (10 ⁵ m/s)	2		2	2		
E_{Bd} (MV/cm)	1.2		2.4	2.0		

Table 4.2: Bulk material properties of diamond, Si, and the SiC polymorphs considered in this work (measurements taken from Refs. [82, 100, 127, 27, 64, 137] unless otherwise stated). $\epsilon_{0,\infty\perp}$ ($\epsilon_{0,\infty\parallel}$) refer to relative permittivity perpendicular (parallel) to the crystal c-axis at low and high frequency, with values from [92]. Optical phonon energies and high-frequency permittivity are taken from [125]. E_{eh} values denoted by [†] are estimated using equation 3.7. Defect creation energies are from [98, 115, 21]. Due to the differing commercial availability/utility of different polytypes, more commonly used crystal polytypes are better characterized than less common ones, and thus for the least well-studied polytypes (2H, 8H, 15R) many experimentally determined values are unavailable. Quantities denoted as [calc] were calculated to fill in some of the holes in the literature.

4.2 Heavy Fermion Material

For electron recoil the set of criteria is given by equation 2.74:

1. Small indirect bandgap ($E_g \rightarrow 0$)
2. The bandgap momentum should match DM momentum ($k_g \sim q_\chi$)
3. High effective electron mass ($m_c + m_v \rightarrow \infty$)

Once we include many-body effects via the ELF formulation we also see that we want the support of the ELF to lie within the allowed kinematic region as much as possible (see figure 2.6). The plasmon peak “takes up” the majority of the total ELF bounded by the sum rules [104] and DM particles can only access the tail of the plasmon peak. In view of this we also want

4. Low plasmon energy ω_p

We also want the plasmon peak to be broad so that the tail extends further into the allowed kinematic region. The intrinsic broadening of the plasmon peak is due to Landau damping which leads to a decay rate of the form [30]

$$\Gamma \propto \omega_p \left(\frac{k_D}{k} \right)^3 e^{-k_D^2/k^2} \quad (4.1)$$

where $k_D = \omega_p/v_F$ is the Debye momentum and v_F is the Fermi velocity of the electrons. Γ is maximized when $k \sim k_D \implies \omega_p \sim kv_F$. For electron recoil in a typical material, $k \sim 10$ keV and $\omega_p \sim 10$ eV. Therefore we want

5. Slow Fermi velocity ($v_F \sim 10^{-3}c \approx v_\chi$)

There are many different approaches towards attaining these criteria. Some of the most interesting examples include Dirac materials [69, 57] that has a very small bandgap and slow Fermi velocity, heavily doped semiconductor [45] where the high number dopant levels essentially “fill in” the bandgap as well as modifies the Fermi velocity. Yet another class of material that satisfies many of the above criteria is the heavy fermion material (Kondo insulator) [145, 37], which is characterized by having very high effective masses (10-100 times electron mass), and a small indirect bandgap (meV). Some heavy fermion material such as URu_2Si_2 also has low plasmon energy and slow Fermi velocity [68], which makes it almost the perfect material for detecting electron recoil.

The origin of the small band gap and high effective mass in heavy fermion material is the hybridization of d or f orbitals of the transition metal or rare earth metal atoms (impurities) and the conduction band of the crystal. The simplest example is FeSi [134], also called renormalized

silicon. The d-orbital electrons in the iron impurities remain localized to the iron atoms, forming a lattice of magnetic impurities. Electrons in the material can hop between the delocalized bands and the localized d-orbitals. We can model this situation via a simplified periodic Anderson model which neglects the spin degree of freedom:

$$H = \sum_k \epsilon(k) c_k^\dagger c_k + \sum_i \epsilon_d d_i^\dagger d_i + \sum_{i,k} V(e^{-ik \cdot R_i} d_i^\dagger c_k + h.c.) \quad (4.2)$$

The first and second terms are the Hamiltonian of the conduction band electrons and the impurity atoms respectively. The third term describes electron hopping between the orbitals of the impurity atoms and the conduction band, which leads to band hybridization.

We can Fourier transform the orbital operators and further simplify the Hamiltonian:

$$H = \sum_k \left[\epsilon(k) c_k^\dagger c_k + \epsilon_d d_k^\dagger d_k + V(d_k^\dagger c_k + c_k^\dagger d_k) \right] \quad (4.3)$$

which can be exactly diagonalized to give

$$E_\pm(k) = \frac{1}{2} \left[\epsilon(k) + \epsilon_d \pm \sqrt{(\epsilon(k) - \epsilon_d)^2 + 4V^2} \right] \quad (4.4)$$

The results in a direct gap of size $\approx 2V$ and an extremely small indirect gap (figure 4.4). In reality the size of the indirect gap is set by the Kondo temperature ($T_K \sim \mathcal{O}(\text{meV})$) of the material. For more discussions on the theory of heavy fermion systems we refer the readers to [12, 37, 43, 66, 68] and references therein. Figure 4.4 and 4.5 shows projected reach of FeSi and URu₂Si₂.

One significant drawback with heavy fermion materials is that the transport properties of charge and phonons is rather poor due to high concentration of impurities and various localization effects [77, 145]. It remains unclear whether the conventional TES detector would work for this type of substrate or some radical redesign of the sensor is required.

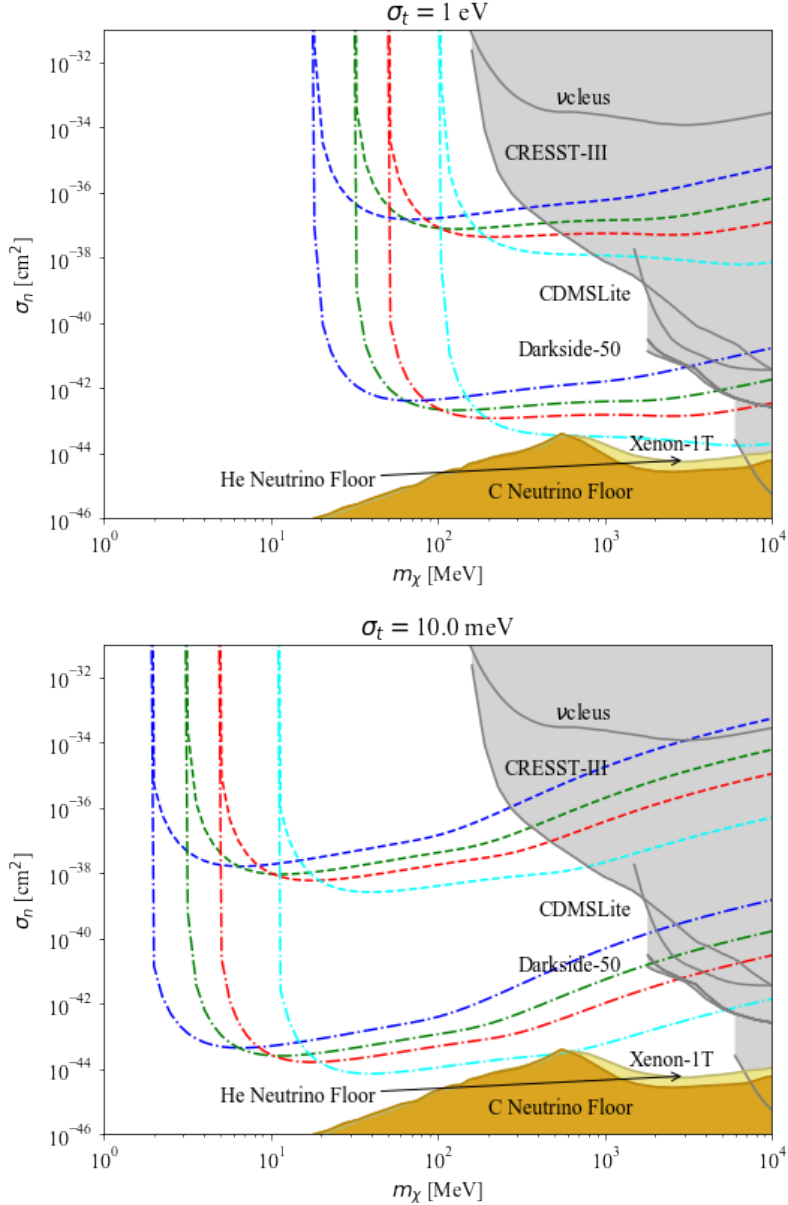


Figure 4.1: Figure taken from [102]. Nuclear recoil projected reach at 95% C.L. for He (blue), Diamond (green), Si (red), and Xe (cyan) for energy thresholds of 1 eV (top) and 10 meV (bottom). The dashed lines are for a g-day exposure, while the dot-dashed lines are for a kg-year exposure. The yellow region indicates the neutrino floor for He [65], and the brown region the neutrino floor for C (computed according to the formalism in Ref. [28]). Also shown in grey are the current best limits on NR dark matter interactions from ν CLEUS [13], CRESST-III [38, 5], CDMSLite [156], Darkside-50 [158], and Xenon-1T [14] for comparison.

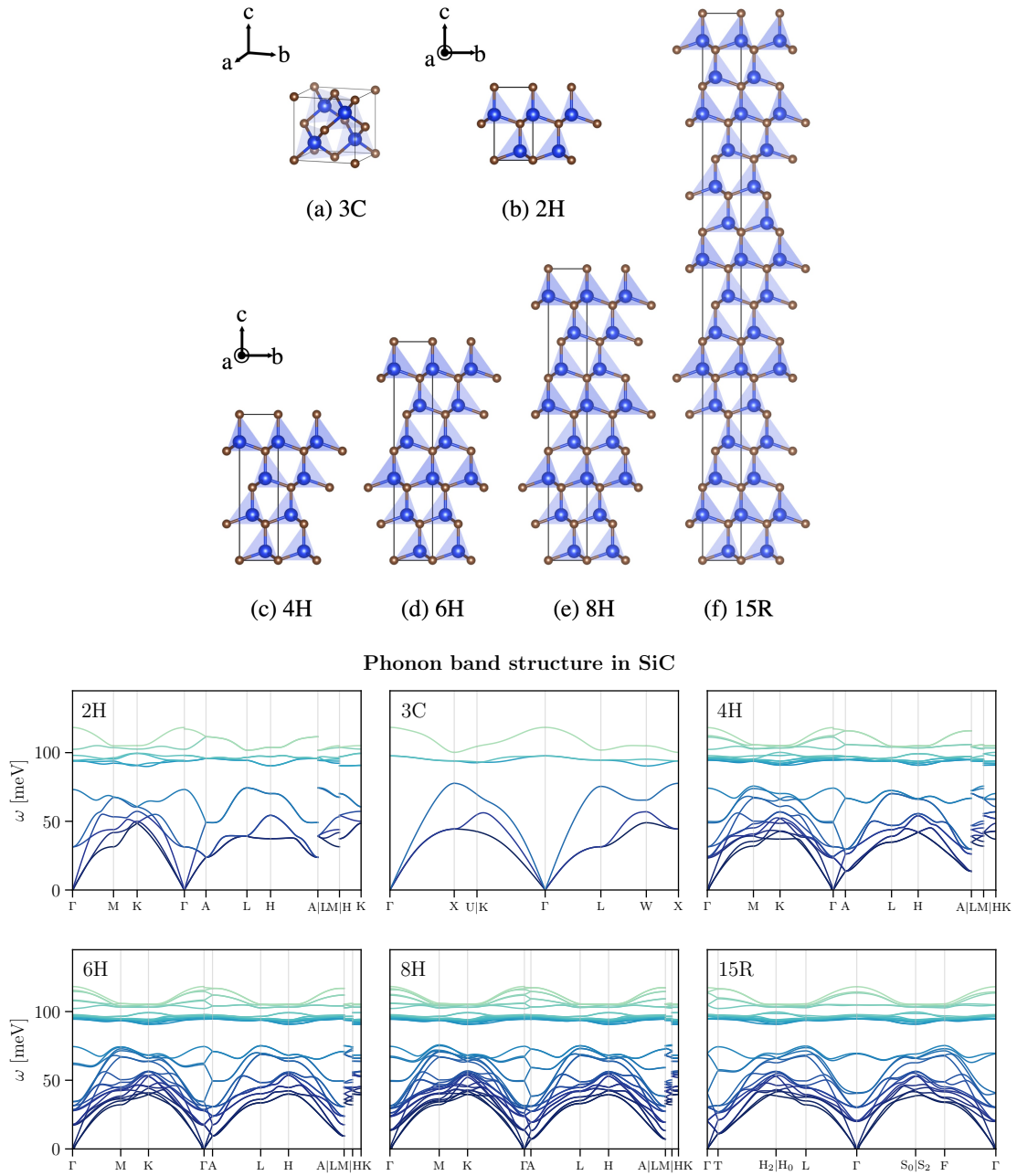


Figure 4.2: (top) Crystal structures of the polytypes of SiC considered in [61]. Si atoms are blue and C atoms are brown. (bottom) Phonon band structures calculated from first principles. For details of calculations, see [61].

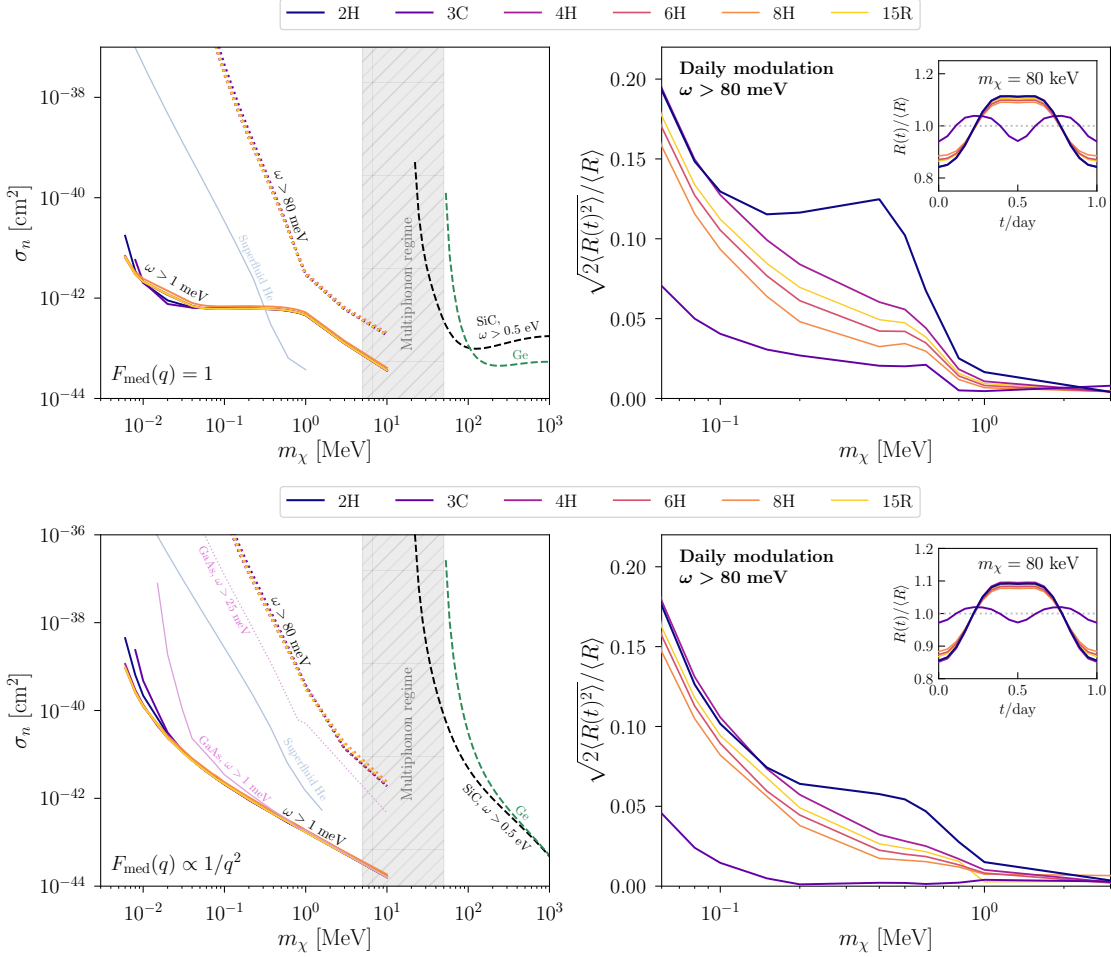


Figure 4.3: Reach and daily modulation for DM interactions mediated by a scalar coupling to nucleons, assuming a massive mediator (top) and massless mediator (bottom). (left) Reach curves assuming kg-year exposure and zero background. For single phonon excitations relevant for $m_\chi \lesssim 10$ MeV, we show two representative thresholds of 1 meV (solid lines) and 80 meV (dotted) for the different SiC polytypes. We also show the reach for a superfluid He target [97]. The dashed lines show sensitivity to nuclear recoils assuming threshold of 0.5 eV. In the shaded region, it is expected that the dominant DM scattering is via multiphonons [34, 160]. (right) The daily modulation of the DM-phonon scattering rate as a function of DM mass, where the quantity shown corresponds exactly to the modulation amplitude for a purely harmonic oscillation. The modulation is much smaller for scattering into acoustic phonons $\omega > 1$ meV, so we only show scattering into optical phonons with $\omega > 80$ meV. The modulation amplitude is generally largest for 2H and smallest for 3C. The inset compares the phase of the modulation among the polymorphs for $m_\chi = 80$ keV.

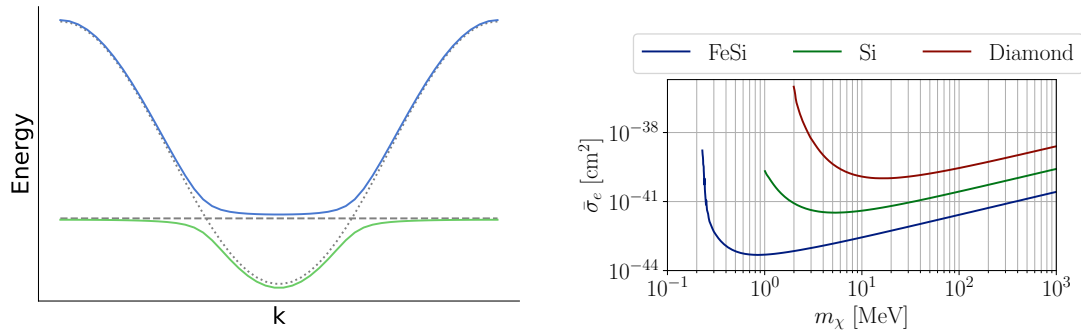


Figure 4.4: (left) Hybridization between the conduction band (dotted) and d/f-orbital (dashed) results in two hybridized bands (solid) with a small band gap and large effective mass indicated by the flatness of the band minimum. (right) Projected 95% C.L. reach of a 1 kg-yr exposure target for FeSi (blue), silicon (green) and diamond (red). The reach curves end due to the bandgap of the respective materials. FeSi ($E_g = 0.18$ eV) not only has the lowest mass reach but also more sensitivity to $\bar{\sigma}_e$ across the whole DM mass region.

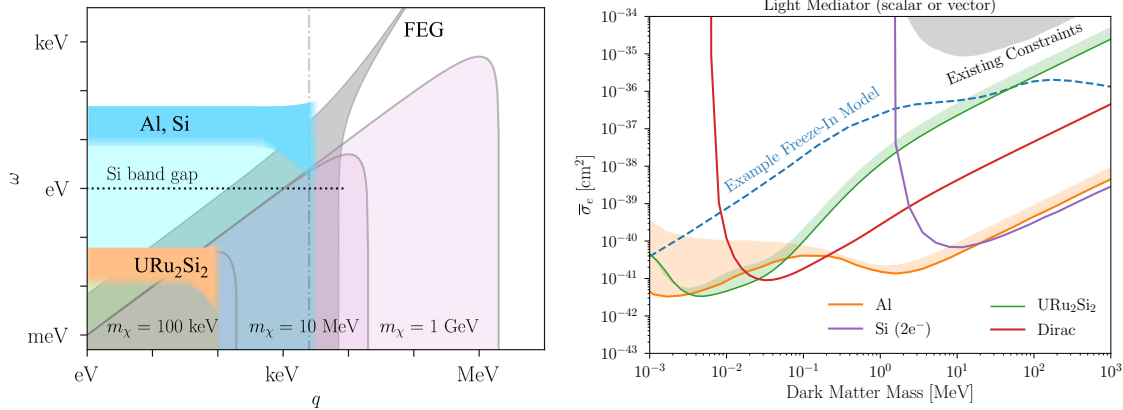


Figure 4.5: Figures taken from [68]. (left) Schematic depiction of the relevant kinematics for sub-GeV DM scattering. The shaded purple parabolas represent the kinematically-allowed region of q and ω for the labelled DM masses. The blue and orange shaded regions represent the support of the plasmon peak of the ELF for typical materials and URu₂Si₂. The tail extends into the DM region for materials such as Al and Si, while for heavy-fermion materials such as URu₂Si₂, the plasmon peak lies within the accessible kinematic region. The range of support for the FEG ELF (equation 2.82) is shown in shaded gray, and can be used to approximate the rate in both superconductors and semiconductors over a limited range of ω . The dot-dashed vertical line indicates the size of the Brillouin zone ($q \approx 2.3$ keV) of Si, while the horizontal dashed line indicates the band gap above which electron scattering can produce ionization. (right) Projected 95% C.L. reach of a 1 kg-yr exposure target of Al (orange), Si (purple), a Dirac material (red) and URu₂Si₂ (green), computed for a light mediator. The Dirac material is computed with density 10 g/cm^3 , gap $2\Delta = 20 \text{ meV}$, Fermi velocity $v_F = 4 \times 10^{-4}c$, background dielectric constant $\kappa = 40$, and Dirac band cutoff $\omega_{\max} = 0.5 \text{ eV}$. URu₂Si₂ has an effective mass of $m^* \simeq 6m_e$, $v_F \simeq 6.5 \times 10^{-5}c$, $\omega_p \simeq 6.5 \text{ meV}$ and a bandgap of $E_g \simeq 5 \text{ meV}$ [20].

Chapter 5

Future Research

We have outlined a broad spectrum of DM interaction channels with solids and from our calculations derived various criteria for choosing optimal substrate for direct detection of sub-GeV DM. I proposed two novel classes of material that are optimal for nuclear and electron interactions respectively and calculated their project reach for light DM.

However this work is far from definitive and there are still much richer condensed matter physics to be explored. I shall list below some of the topics that I have fiddled with but still require further research:

Dynamics of Defects The dynamics of defects is usually neglected in most treatment of nuclear recoil. However as we have shown in chapter 2, long-lived defects can potentially modify the observed event spectrum and could be important for low mass DM detection. A proper study of defect formation rate and their dynamics in various substrates in the kinematic region relevant to DM detection is yet to be completed.

Exotic Quasi-particles We have pointed out that the potential creation of crowdions from nuclear recoil can emit additional phonons. Some preliminary results regarding crowdion formation and crowdion-phonon interaction can be found in [123] and [140]. However more experimental and theoretical study is still needed to confirm the existence of crowdion and to understand its dynamics. Due to the directional nature of crowdion formation it might be possible to utilize it to extract per-event directional information.

Apart from crowdion, other exotic quasi-particles such as phonon polaritons and magnons also have the potential to be used for detection of DM [120]. A full survey of all the different kinds of quasi-particles that can be found in solid-state systems is yet to be completed.

Mixed Channels Most of the focus of this work has been on single-mode channels, i.e. interactions that involve production of only a single type of excitation. Although we have listed some examples of mixed channels, the list is not exhaustive and many of the examples we have listed are still not completely understood or verified experimentally. Mixed channels potentially covers a significant amount of new parameter space beyond that single-mode channels. Simultaneous co-production of multiple types of excitations relaxes the stringent kinematics of two-body scattering and opens up the phase space. Proper treatments of mixed channels are often theoretically challenging, and more work is yet to be done.

TES Chaos In chapter 3 we have written down the equations governing the dynamics of TES (equation 3.62). Although we immediately proceeded to linearize these equations around the operating point, as is commonly done in the field, the full non-linear dynamics of the system without any linearization remains an open problem. Under the RSJ model the TES is similar to a Josephson junction which is known to be a chaotic system [40]. As such the full non-linear dynamics of TES should also exhibit chaotic behavior. Given that chaotic systems are highly sensitive to any perturbations, however small, it might be possible to reap benefits by controlling the TES chaos in a manner similar to that described in [52]. A study of TES chaos via chaos control theory [175] and machine learning techniques [171, 135] seems interesting.

Appendix A

Density Functional Theory

Density functional theory (DFT) is a coherent set of approximations that enables us to calculate the dynamics of many-electron systems. In a typical macroscopic system there are $O(10^{23})$ atoms and each atoms contribute multiple valence electrons that are interacting both with the lattice of nucleus as well as with other electrons. In principle we can write down a gigantic system of $O(10^{23})$ Schrödinger equations but it is obviously an impractical approach. Fortunately with DFT we can greatly reduce the effective degrees of freedom of this problem and obtain useful results. In this section we present a brief overview of the basics of DFT. For a more detailed introduction please refer to [47, 118, 154].

The first approximation we are going to introduce is the **Born-Oppenheimer approximation**. Since each proton and neutron in the nucleus is more than 1800 times heavier than the electron, we can effectively decouple the dynamics of the nuclei from the dynamics of the electrons. In many problems we are interested in the ground state properties of the electron system. We can freeze the positions of the nuclei and write down a complete description of the electron system $\psi(\mathbf{r}_1, \dots, \mathbf{r}_N)$ via Schrödinger equation:

$$\left[\frac{1}{2m_e} \sum_{i=1}^N \nabla_i^2 + \sum_{i=1}^N V(\mathbf{r}_i) + \sum_{\substack{i,j \\ j \neq i}} U(\mathbf{r}_i, \mathbf{r}_j) \right] \psi = E\psi \quad (\text{A.1})$$

where m_e is the electron mass, V is the external potential from the nuclei in the lattice, and $U(\mathbf{r}_i, \mathbf{r}_j) = e^2/|\mathbf{r}_i - \mathbf{r}_j|$ is the Coulomb potential between electrons. For clarity we drop the spin degree of freedom in our discussion.

A.1 Hartree-Fock Method

Equation A.1 in principle contains all the physics we need to calculate the properties of the electron system. However it is definitely impractical to solve it directly. The next approximation we need is to write the complete wavefunction ψ in terms of single-electron wavefunctions ϕ :

$$\psi(\mathbf{r}_1, \dots, \mathbf{r}_N) = \phi_1(\mathbf{r}_1) \dots \phi_N(\mathbf{r}_N) \quad (\text{A.2})$$

Substituting this into equation A.1 and integrating out all except the i -th wavefunction gives

$$\left[\frac{1}{2m_e} \nabla^2 + V(\mathbf{r}) + e^2 \sum_{j \neq i} \int d^3 \mathbf{r}' \frac{|\phi_j(\mathbf{r}')|^2}{|\mathbf{r}' - \mathbf{r}|^2} \right] \phi_i(\mathbf{r}) = \varepsilon_i \phi_i(\mathbf{r}) \quad (\text{A.3})$$

$$\left[\frac{1}{2m_e} \nabla^2 + V(\mathbf{r}) + e^2 \int d^3 \mathbf{r}' \frac{n(\mathbf{r}')}{|\mathbf{r}' - \mathbf{r}|^2} \right] \phi_i(\mathbf{r}) = \varepsilon_i \phi_i(\mathbf{r}) \quad (\text{A.4})$$

where $n(\mathbf{r})$ is the number density of electrons. The third term inside the bracket is called the Hartree potential. This brings down the dimension of the problem from $3N$ coordinates to 3 and is a much more tractable equation compared to equation A.1. Another feature is that the electron density enters into the effective Hamiltonian. We shall generalize this later.

In order to solve equation A.4 we adopt a self-consistent approach:

1. Start with initial trial electron density $n(\mathbf{r})$.
2. Solve A.4 to find the single-electron wavefunctions ϕ_i .
3. Calculate the electron density n' from the newly found wavefunctions ϕ_i via $n' = \sum_i |\phi_i|^2$.
4. Compare n and n' for convergence. If they differ significantly, repeat above steps with n' as the new initial trial density.

The general DFT calculation follows the same structure as above except the effective Hamiltonian contains a couple more terms than the Hartree Hamiltonian in A.4.

An additional improvement we can make is to incorporate the fact that electrons are fermions and thus the total wavefunction should be anti-symmetric under the exchange of two electrons. This can be done by anti-symmetrizing the expression in A.2, or equivalently by setting the wavefunction to be the Slater determinant

$$\psi(\mathbf{r}_1, \dots, \mathbf{r}_N) = \frac{1}{\sqrt{N!}} \det \begin{pmatrix} \phi_1(\mathbf{r}_1) & \dots & \phi_1(\mathbf{r}_N) \\ \vdots & \ddots & \vdots \\ \phi_N(\mathbf{r}_1) & \dots & \phi_N(\mathbf{r}_N) \end{pmatrix} \quad (\text{A.5})$$

This will result in an additional exchange term in the Hamiltonian for the single-electron equation:

$$\left[\frac{1}{2m_e} \nabla^2 + V(\mathbf{r}) + e^2 \int d^3 \mathbf{r}' \frac{n(\mathbf{r}')}{|\mathbf{r}' - \mathbf{r}|^2} \right] \phi_i(\mathbf{r}) + e^2 \sum_{j \neq i} \int d^3 \mathbf{r}' \frac{\phi_j^*(\mathbf{r}') \phi_i(\mathbf{r}')}{|\mathbf{r}' - \mathbf{r}|^2} \phi_j(\mathbf{r}) = \varepsilon_i \phi_i(\mathbf{r}) \quad (\text{A.6})$$

which is called the Hartree-Fock equation. Solving this equation is significantly more difficult due to the non-local exchange term and coupling between different ϕ 's.

A.2 Hohenberg-Kohn Theorems

The power of DFT stems from the realization that we do not actually need to deal with the wavefunctions directly and instead can express everything in terms of the electron density $n(\mathbf{r})$. This result is proved in the foundational paper by Hohenberg and Kohn [74], and is now referred to as the Hohenberg-Kohn theorems. We reproduce the proof below. In what follows we assume that the ground state of the system is non-degenerate.

Theorem. (Hohenberg-Kohn)

- (I) *The ground state electron density $n_0(\mathbf{r})$ determines all properties of the system. In particular the ground state energy E_0 is a functional of $n_0(\mathbf{r})$.*
- (II) *The energy written as density functional $E[n(\mathbf{r})]$ of the system gives the lowest energy E_0 if and only if the input density $n(\mathbf{r})$ is the true ground state density $n_0(\mathbf{r})$.*

Proof. (I) The only quantity that differs between different systems is the external (lattice) potential $V(\mathbf{r})$. The other terms in the full Hamiltonian describes universal electron-electron interactions. Therefore we can view the Hamiltonian H as a functional of V which in turn also implies that the wavefunction ψ is also a functional of V , i.e.

$$\psi = \psi[V(\mathbf{r})] \quad (\text{A.7})$$

What remains is to show that V can be viewed as a functional of $n_0(\mathbf{r})$. We proof this by contradiction. Suppose there existed two different potentials V and V' (corresponding respectively

to Hamiltonians H, H' , ground state energies E_0, E'_0 and wavefunctions ψ, ψ') that lead to the same ground state density $n_0(\mathbf{r})$, from the variational principle we would have

$$E_0 = \langle \psi | H | \psi \rangle < \langle \psi' | H | \psi' \rangle \quad (\text{A.8})$$

$$= E'_0 + \langle \psi' | H - H' | \psi' \rangle \quad (\text{A.9})$$

$$= E'_0 + \int (V(\mathbf{r}) - V'(\mathbf{r})) n_0(\mathbf{r}) \, d\mathbf{r} \quad (\text{A.10})$$

Now exchanging the roles of primed and unprimed quantities, we also have

$$E'_0 < E_0 + \int (V'(\mathbf{r}) - V(\mathbf{r})) n_0(\mathbf{r}) \, d\mathbf{r} \quad (\text{A.11})$$

Adding the two inequalities together leads to the contradiction:

$$E_0 + E'_0 < E_0 + E'_0 \quad (\text{A.12})$$

Therefore we conclude that V is a functional of n_0 , which in turn means that ψ and subsequently all properties of the system can be viewed as functional of n_0 .

(II) We can write the energy of the system E as a functional of test ground state density n :

$$E[n] = \int V(\mathbf{r}) n(\mathbf{r}) + F[n] \quad (\text{A.13})$$

where F is a universal functional containing kinetic and electron-electron energies that do not depend on the material-specific V . Alternatively we can also view this functional as a functional of ψ and from the variational principle we would have

$$E[\psi] = E_0 < E[\psi'] , \forall \psi' \neq \psi \quad (\text{A.14})$$

where ψ is the true ground state and ψ' is some other wavefunction. Since the wavefunction is itself a functional of the ground state density, we must equivalently have

$$E[n_0] = E_0 < E[n] , \forall n \neq n_0 \quad (\text{A.15})$$

□

The Hohenberg-Kohn theorems convert the problem of interacting electrons from solving a large system of Hartree-Fock type of equations into a much more tractable minimization problem. There

are still two missing pieces - the exact forms of F and V . In DFT lingo, F is called the **exchange-correlation functional** or sometimes **energy functional**. There is no exact solution to F but there are various existing numerical approximations such as LDA, GGA, PBE, HSE and B3LYP. V is determined by the positions of the atoms (lattice structure) as well as the potential generated by each individual atom. Again there is no exact solution to the atomic potential, approximations called **pseudopotentials** need to be specified (usually USPP or PAW). In papers that involve DFT calculations one would find descriptions such as “the calculation is performed using projector augmented wave (PAW) pseudopotentials and the Perdew-Becke-Ernzerhof exchange-correlation functional revised for solids (PBEsol)” that specifies the choice of the energy functional and pseudopotentials. Since DFT calculations are usually not performed in the position space but rather in the reciprocal space, the momentum grid (k -grid) also needs to be specified. For example “3x3x3” means there are 3 grid points in each direction of the Brillouin zone.

A.3 Example Calculation with Quantum ESPRESSO

Quantum ESPRESSO [58, 4] is one of the most popular DFT software packages that specialize in crystalline materials that has a periodic structure. Below is an example input file for calculation of silicon electron wavefunctions. For detailed documentation please refer to [2, 1].

```
&control
  calculation= 'scf'
  restart_mode= 'from_scratch'
  prefix='silicon'
  tstress= .false.
  tprnfor= .false.
  pseudo_dir= './'
  outdir= './'
  verbosity= 'high'
/
&system
  ibrav= 2
  celldm(1)= 10.330495
  nat= 2
  ntyp= 1
  ecutwfc= 59.0
  nbnd= 56
```

```

nosym= .true.
noinv= .true.
/
&electrons
  diagonalization= 'david'
  mixing_mode= 'plain'
  mixing_beta= 0.7
  conv_thr= 1.0d-8
  diag_full_acc= .true.
/
ATOMIC_SPECIES
Si 28.0855 Si.upf
ATOMIC_POSITIONS crystal
Si 0.00 0.00 0.00
Si 0.25 0.25 0.25
K_POINTS automatic
8 8 8 0 0 0

```

The exchange-correlation functional and pseudopotential are specified in a separate file (`Si.upf`). In some cases we can also manually specify the functional by adding an option such as `input_dft='hse'` under the `system` section. The `K_POINTS` section specifies the k-grid used for the calculation. In the above example it is a 8x8x8 Monkhorst-Pack grid. In general we want to have the minimum k-points as long as the result of our calculation still converges to the correct value. There is no a priori rules for choice of parameters such as the k-grid, `ecutwfc` and `nbnd`. Convergence tests need to be performed by repeating the calculation for a range of different values to find right combination.

Once the wavefunctions and the energies are solved via DFT, they need to be post-processed and combined to get the structure factor. Some code that I have written and improved over the years can be found at [3].

A.4 Additional Corrections to DFT

There are a couple important omissions in DFT calculations that are relevant to dark matter direct detection. We briefly describe them in this section.

Core Electrons By design the pseudopotential lumps together the nucleus and the core electrons (figure A.1) in order to improve computation efficiency as core electrons are usually inert in many

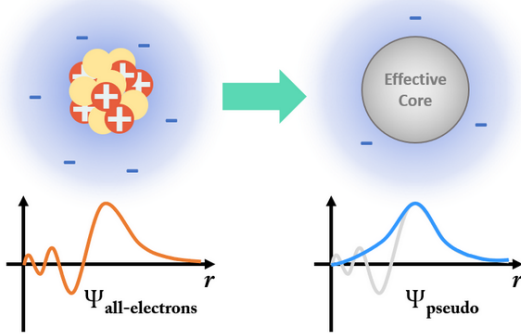


Figure A.1: By lumping together the nucleus and core electrons in the atoms, the resultant potential leads to a smoother wavefunction (hence fewer basis components are needed), and fewer degrees of freedom as we have dropped the core electrons from our wavefunction.

processes. As a result of this there is no degree of freedom for the core electrons in DFT calculations. However it was found that the core electrons can in fact contribute significantly to the electron transition rate [159]. As such separate calculations need to be performed alongside DFT calculations in order to properly include this effect. The EXCEED-DM package [159] includes capabilities for all-electron calculations of the electron transition structure factor.

Phonons DFT operates under the Born-Oppenheimer approximation where the positions of the nuclei are assumed to be fixed. As such contributions involving phonons, such as phonon-assisted electron transitions, are neglected in DFT calculations. A simple way to include effects of phonons is via the semi-classical **Williams-Lax theory** [174]. In this theory we assume that the positions of the nuclei are Gaussian distributed around their nominal positions. For each position configuration \mathbf{x} of the lattice we perform a separate DFT calculation and calculate the ensemble average of our target quantity F over the distribution:

$$F(T) = \int d\mathbf{x} \left[\prod_i \frac{x_i \exp(-x_i^2/2\sigma_{i,T}^2)}{\sqrt{2\pi}\sigma_{i,T}} \right] F(\mathbf{x}) \quad (\text{A.16})$$

where T represents the temperature of the system and $F(\mathbf{x})$ is the quantity F calculated with position configuration \mathbf{x} . As can be seen this is potentially a very costly calculation as we need to generate a large sample of lattice configurations and repeat the same DFT calculation many times. However it was discovered [173] that we actually only need to perform the calculation over one particular lattice configuration where each nucleus displaced by an amount calculated

from an average of normal modes. This one-shot method is extremely powerful as we are able to include phonon effects without adding any extra computational cost. Figure A.2 shows an example calculation of optical absorption coefficient using this technique.

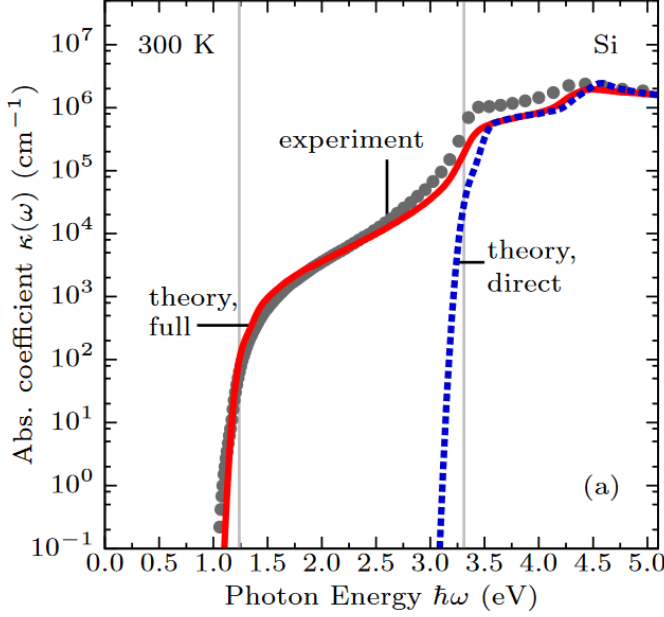


Figure A.2: Figure taken from [173]. Optical absorption coefficient of silicon at room temperature from experimental measurements (gray), DFT calculation with nuclei at their nominal positions (blue), and DFT calculation with nuclei displaced from their nominal positions according to the one-shot recipe (red). We can see that the one-shot method reproduces experimental measured values perfectly by including the contribution from phonons which is significant at sub-gap energies.

Appendix B

Signal Theory and Optimal Filter

Assuming no pile-up, the TES reading $y(t)$ can be modelled by the following equation

$$y(t) = As(t - t_0) + n(t) \quad (\text{B.1})$$

where A is the unknown pulse amplitude that we want to estimate from the signal, $s(t)$ is some normalized pulse shape (**signal template**) that we have pre-determined either from theory or calibration, t_0 is some random time shift due to e.g. statistical error in our triggering method, and $n(t)$ is the noise in our sensor. If we assume that our noise is stationary, then it is fully described by its power spectrum. Therefore it is easier to work in the frequency domain:

$$Y(\omega) = AS(\omega)e^{-i\omega t_0} + N(\omega) \quad (\text{B.2})$$

where the upper case denotes Fourier transform, and probability distribution of $|N(\omega)|$ is given by a normal distribution of mean 0 and variance $J(\omega)$, i.e. $P(|N(\omega)|) \sim \mathcal{N}(0, J(\omega))$. $J(\omega)$ is called the noise **energy spectral density** (ESD). For finite trace length T we also define the noise **power spectral density** (PSD) to be $J(\omega)/T$ which is more well-behaved as $T \rightarrow \infty$. For fixed trace length they only differ by a constant factor so the two terms are loosely interchangeable.

In practice, the TES are read out at discrete time intervals and both the time and frequency labels are discrete. Therefore we replace the functional dependence on ω by subscripts, e.g. $Y_k \equiv Y(\omega_k)$ where ω_k is the position of the k -th frequency bin of the discrete Fourier transform. Thus given

$$Y_k = AS_k e^{-i\omega_k t_0} + N_k, \quad (\text{B.3})$$

$$\mathbb{P}_N(|N(\omega)|) \sim \mathcal{N}(0, J(\omega)) \quad (\text{B.4})$$

we want to construct the best estimator \hat{A} in terms of S_k and J_k .

B.1 Maximum-Likelihood Estimation

The word “best” is somewhat ambiguous. There are at least two independent desiderata for an ideal estimator:

1. **Unbiased:** $\mathbb{E}[\hat{A} - A] = 0$, i.e. the expected value of the estimator is the true value.
2. **Minimal Variance:** $\mathbb{E}[(\hat{A} - A)^2]$ is minimum.

An estimator that satisfies both criteria is called a **minimum-variance unbiased** (MVU) estimator. If we are given a formula for \hat{A} we can calculate its expectation and check whether it is equal to the true value. Therefore it is easy to check whether the first criteria is fulfilled. For the second criteria, we can calculate the variance of our estimator, but how would we know if it is minimum across all possible estimators we can construct?

In the next section we introduce a theorem that gives a lower bound (Cramér-Rao lower bound) to the variance of unbiased estimators. If the variance of an unbiased estimator attains this lower bound, then it is guaranteed that no other estimators have a lower variance than it and thus it is an MVU estimator. An MVU estimator that attains the Cramér-Rao lower bound is called an **efficient** estimator. Efficient estimators are the best estimators one can construct w.r.t. the two requirements above. In what follows we sometimes use “efficient” and “optimal” interchangeably.

Note that there are scenarios where the variance of the MVU estimator, even though by definition being the minimum among all estimators, still does not attain the Cramér-Rao lower bound. In such cases there is no efficient estimator.

Although there is no universal procedure that would allow us to construct an efficient estimator – especially since such an estimator might not even exist – there is a type of estimator that is **asymptotically efficient** as we have sufficiently large number of data points along with satisfying some mild regularity conditions [89]. This is of course none other than the ubiquitous **maximum-likelihood estimator** (MLE). The familiar **Optimal Filter** (OF) [157] is an MLE.

For our problem, the likelihood \mathcal{L} of A (assuming $t_0 = 0$) is given by the probability of observing the particular noise values:

$$\mathcal{L}(A) = \prod_k P_N(|Y_k - AS_k|) \quad (\text{B.5})$$

$$= \prod_k \frac{1}{\sqrt{2\pi J_k}} \exp \left[-\frac{|Y_k - AS_k|^2}{2J_k} \right] \quad (\text{B.6})$$

$$= (\text{const.}) \exp \left[-\frac{1}{2} \sum_k \frac{|Y_k - AS_k|^2}{J_k} \right] \quad (\text{B.7})$$

The MLE for A is then given by the value of A that maximizes this likelihood function. It is conventional to define the chi-squared function $\chi^2(A)$:

$$\chi^2(A) = -2 \ln \mathcal{L}(A) = \sum_k \frac{|Y_k - AS_k|^2}{J_k} \quad (\text{B.8})$$

Then equivalently the MLE is given by maximizing $\chi^2(A)$. If we also include the unknown time shift t_0 then the χ^2 becomes

$$\chi^2(A, t_0) = \sum_k \frac{|Y_k - AS_k e^{i\omega_k t_0}|^2}{J_k} \quad (\text{B.9})$$

We will consider the optimality in these two cases separately.

B.2 Cramér-Rao Lower Bound

The most important result we need from signal theory is the Cramér-Rao lower bound (CRLB) [89, 164], which we will state without proof:

Theorem. (Cramér-Rao) *Let $\mathcal{L}(\theta_i)$ be the likelihood function for a set of (complex) parameters θ_i ($i=1,2,\dots,m$) and assume both the likelihood and its logarithm are both finite and smooth. The covariance matrix of any unbiased estimator $\hat{\theta}_i$ is bounded below by the inverse of Fisher information matrix \mathbf{I} :*

$$\text{Cov}(\hat{\theta}_i, \hat{\theta}_j) \geq [\mathbf{I}^{-1}]_{ij} \quad (\text{B.10})$$

where

$$\mathbf{I}_{ij} = \mathbb{E} \left[\left(\frac{\partial \ln \mathcal{L}}{\partial \theta_i} \right)^* \frac{\partial \ln \mathcal{L}}{\partial \theta_j} \right]. \quad (\text{B.11})$$

Equality holds if and only if the derivative of log-likelihood depends linearly on the error of the estimator with Fisher information as the coefficients:

$$\frac{\partial \ln \mathcal{L}}{\partial \boldsymbol{\theta}} = \mathbf{I}(\hat{\boldsymbol{\theta}} - \boldsymbol{\theta}) \quad (\text{B.12})$$

□

Let us try to apply this theorem to our MLE without time shift. For brevity we switch to matrix notation. We also define the covariance matrix $\mathbf{C} = \mathbb{E}[(\mathbf{Y} - A\mathbf{S})(\mathbf{Y} - A\mathbf{S})^\dagger] = \text{diag}(J_k)$. The log-likelihood is then written as

$$\ln \mathcal{L} = -\frac{1}{2}(\mathbf{Y} - A\mathbf{S})^\dagger \mathbf{C}^{-1}(\mathbf{Y} - A\mathbf{S}) \quad (\text{B.13})$$

For generality we assume A is complex thus we have two independent parameters A and A^* . The case for A is real is easy to derive analogously. First we calculate the derivative of the log-likelihood:

$$\frac{\partial \ln \mathcal{L}}{\partial A} = \frac{1}{2}(\mathbf{Y} - A\mathbf{S})^\dagger \mathbf{C}^{-1} \mathbf{S} + \text{c.c.} \quad (\text{B.14})$$

The Fisher information matrix is given by, e.g.:

$$[\mathbf{I}]_{AA} = \frac{1}{4} \mathbb{E} [\mathbf{S}^\dagger \mathbf{C}^{-1} (\mathbf{Y} - A\mathbf{S})(\mathbf{Y} - A\mathbf{S})^\dagger \mathbf{C}^{-1} \mathbf{S} + (\mathbf{S}^\dagger \mathbf{C}^{-1} (\mathbf{Y} - A\mathbf{S}))(\mathbf{S}^\dagger \mathbf{C}^{-1} (\mathbf{Y} - A\mathbf{S})) + \text{c.c.}] \quad (\text{B.15})$$

$$= \frac{1}{2} \mathbf{S}^\dagger \mathbf{C}^{-1} \mathbf{C} \mathbf{C}^{-1} \mathbf{S} + \frac{1}{4} \mathbb{E} [(\mathbf{S}^\dagger \mathbf{C}^{-1} (\mathbf{Y} - A\mathbf{S}))(\mathbf{S}^\dagger \mathbf{C}^{-1} (\mathbf{Y} - A\mathbf{S})) + \text{c.c.}] \quad (\text{B.16})$$

The second term is zero because the distribution of $\mathbf{N} = \mathbf{Y} - A\mathbf{S}$ is circularly symmetric and thus it must have zero pseudo-variance¹. Simplifying and repeating the calculation for the other

¹Suppose we have a complex random variable Z that is circularly symmetric, we can introduce a rotation $Z' = e^{i\phi} Z$ and from symmetry we must have $\mathbb{E}[ZZ] = \mathbb{E}[Z'Z'] = e^{2i\phi} \mathbb{E}[ZZ]$ which is consistent if and only if $\mathbb{E}[ZZ] = 0$.

pairs of variables we see that the Fisher information matrix is given by

$$\mathbf{I} = \frac{1}{2}(\mathbf{S}^\dagger \mathbf{C}^{-1} \mathbf{S}) \begin{pmatrix} 1 & 1 \\ 1 & 1 \end{pmatrix} \quad (\text{B.17})$$

Returning to equation B.14, we can see that the derivative can be rewritten as

$$\frac{\partial \ln \mathcal{L}}{\partial A} = \frac{1}{2}(\mathbf{S}^\dagger \mathbf{C}^{-1} \mathbf{S}) \left(\frac{\mathbf{Y}^\dagger \mathbf{C}^{-1} \mathbf{S}}{\mathbf{S}^\dagger \mathbf{C}^{-1} \mathbf{S}} - A^* \right) + \text{c.c.} \quad (\text{B.18})$$

$$= [\mathbf{I}]_{AA^*}(\hat{A}^* - A^*) + [\mathbf{I}]_{AA}(\hat{A} - A) \quad (\text{B.19})$$

and similarly for the derivative w.r.t. A^* . Thus equation B.12 is satisfied and the MLE for A (and A^*) is efficient. Note that in the case of complex parameters, efficiency only implies minimum variance in the amplitude $|A|$ since the variance of a complex parameter is equal to the variance of its amplitude. The uncertainty in the phase of the parameter $\arg A$ is not bounded.

For real-valued A this reduces to the familiar OF expression for A :

$$\boxed{\hat{A}_{OF} = \frac{\mathbf{S}^\dagger \mathbf{C}^{-1} \mathbf{Y}}{\mathbf{S}^\dagger \mathbf{C}^{-1} \mathbf{S}} = \frac{\sum_k S_k^* Y_k / J_k}{\sum_k |S_k| / J_k}} \quad (\text{B.20})$$

Therefore we have proven that the OF algorithm **without time shift** is indeed strictly optimal since it is both unbiased (easy to check) and saturates CRLB – there is no other estimator with better resolution. Unfortunately, once we introduce time shift, this optimality no longer holds strictly (although it can still hold asymptotically).

B.3 Translation Invariant Fourier Transform

If we include an unknown time shift we immediately see that the MLE is no longer efficient. This is because the derivative of $\chi^2(A, t_0)$ w.r.t. t_0 would be of the form

$$\frac{\partial \chi^2}{\partial t_0} = (\dots) e^{i\omega_k t_0} + \text{c.c.} \quad (\text{B.21})$$

There is no way we will be able to write this into linear factors of the form $(\hat{t}_0 - t_0)$ which is required by equation B.12. Since equation B.12 is a matrix equation – derivatives w.r.t all parameters need to have the right form concurrently – this means that not only our MLE is not efficient in estimating t_0 it is also no longer efficient in estimating A . Thus, strictly speaking, the

MLE with time shift is not optimal².

Absorbing the phase factor into the signal template will only make the template t_0 dependent and doesn't reduce the number of parameters, and absorbing the phase factor into the amplitude will turn the amplitude into a vector complex vector $A_k = Ae^{i\omega_k t_0}$ which increases the number of parameters. We can work around this issue if we perform an additional transform to linearize our time shift by replacing the phases in our Fourier transform coefficient by phase differences, e.g.

$$\arg Y_k \rightarrow \arg Y_k - \arg Y_{k+1} \quad (\text{B.22})$$

The argument of the highest frequency component is left unchanged to make this transformation invertible. By applying this additional transformation, the time shift will now introduce a **constant** factor instead of a k -dependent factor:

$$e^{i\omega_k t_0} \rightarrow e^{i(\omega_k - \omega_{k+1})t_0} \quad (\text{B.23})$$

$$= e^{-i\Delta\omega t_0} \quad (\text{B.24})$$

Now if we absorb this factor into the amplitude, we will just have a single complex amplitude in place of the original two real parameters. In particular, our χ^2 now becomes

$$\chi^2(A, t_0) = \sum_k \frac{|Y_k - AS_k e^{i\Delta\omega t_0}|^2}{J_k} \quad (\text{B.25})$$

$$= \sum_k \frac{|Y_k - A'S_k|^2}{J_k} \quad (\text{B.26})$$

where $A' = Ae^{i\Delta\omega t_0}$. The χ^2 is transformed back into the case without time shift, and we have already shown that the MLE is efficient in this case even when A' is complex. Thus the variance of A' which is equal to the variance of A is minimal. This combination of discrete Fourier transform plus phase-shift transformation is called **Translation-Invariant Fourier Transform** (TIFT). By applying TIFT we can restore strict optimality of our MLE. This is important later when we apply machine learning techniques to remove the need for knowing the signal template beforehand.

B.4 Stationarity and Cyclostationarity

Before proceeding further we shall take a detour to delve a little deeper into our noise assumption. Throughout this chapter we have assumed that each of the noise components N_k is independently

²In practice this is usually not an issue as for each trace we collect a large number of points (long traces with high sampling frequency) which allows us to attain the asymptotic optimality.

distributed following a normal distribution with mean zero and variance given by some constant J_k . Effectively this limits us to only consider (wide-sense) stationary³ noise. To see why this is the case, we introduce another important theorem from signal theory:[169, 170, 91]

Theorem. (Wiener–Khinchin) *The power spectral density $J(\omega)/T$ and the auto-correlation function $R(t) = \mathbb{E}[n(\tau - t)n(\tau)]$ of a signal are Fourier transform pairs.*

Proof. Using the convolution property of Fourier transform, we have

$$J(\omega)/T = \frac{1}{T} \mathbb{E}[N^*(\omega)N(\omega)] \quad (\text{B.27})$$

$$= \frac{1}{T} \mathcal{F}\{\mathbb{E}[n(-t)*n(t)]\} \quad (\text{B.28})$$

$$= \frac{1}{T} \mathcal{F}\left\{\int_T \mathbb{E}[n(t'-t)n(t')]dt'\right\} \quad (\text{B.29})$$

$$= \mathcal{F}\{R(t)\} \quad (\text{B.30})$$

□

Note that if the noise process is not stationary then the right hand side would have been time-dependent since the Fourier transform and convolution integral are only performed on the finite time window T . Therefore OF cannot handle non-stationary noise in general.

However, we can also see from the above derivation that the auto-correlation does not need to be *strictly* stationary. If the auto-correlation function is time-dependent but is periodic with period τ , then the PSD will be equal to the average of $R(t)$ over the time window of T which will still be time independent as long as $\tau \ll T$. Processes with periodic auto-correlation are called **cyclostationary**. Cyclostationarity introduces correlations between noises of different frequencies and thus our covariance matrix⁴ \mathbf{C} is no longer diagonal. However this is not an issue since everything covered in section B.2 still holds even if the covariance matrix is non-diagonal. In other words, OF is optimal for both stationary and cyclostationary noises!

To gain a better intuition on cyclostationary noises, let us consider a simple example. The pulse tubes on dilution fridges often generates periodic “chirps” that has the form illustrated in figure B.1. This is a great example of cyclostationary noise.

In conclusion we have shown that OF can handle not only stationary but also cyclostationary noises. However optimality for non-stationary noise beyond cyclostationarity is not guaranteed.

³Stationarity means the statistical properties of $n(t)$ stay constant over time. In particular the auto-correlation between two points in time $R(t_1, t_2) = \mathbb{E}[n(t_1)n(t_2)]$ only depends on the time difference $R(t_1, t_2) = R(t_2 - t_1) = R(t)$.

⁴also referred to as the **spectral correlation density** (SCD) in the context of cyclostationary processes.

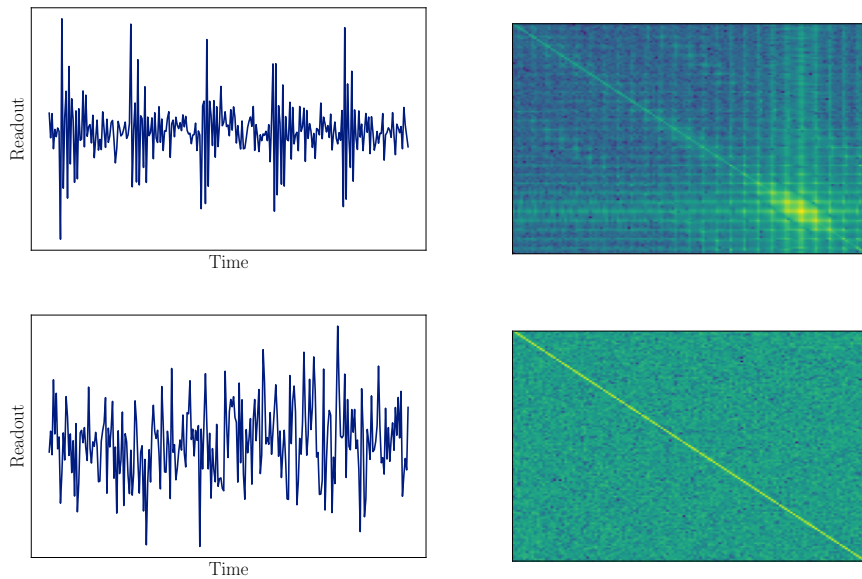


Figure B.1: (top) An example of chirp noise and the corresponding covariance matrix in the frequency domain. The chirp noise which is cyclostationary introduces plenty of non-diagonal entries in the covariance matrix. (bottom) An example of pure white noise and the corresponding covariance matrix in the frequency domain. The stationary white noise has only diagonal elements in its covariance matrix. In fact it is approximately an identity matrix. The covariance matrix is well-defined in both cases and thus OF is optimal regardless of whether the noise is stationary or cyclostationary.

B.5 Templateless Optimal Filter

Now that we have clarified the assumptions we made for our noise. Let us turn our attention to the other piece of the input which is the signal template. The signal template is usually constructed from calibration data by averaging pulse shape that corresponds to the energy range of interest. Alternatively we can also construct analytical model of the signal template and use that the fit our amplitude. In either case extra work is required to build a reasonable signal template. In this section we show that we can skip this step and simultaneously fit the amplitude and the signal template in the TIFT domain via the **Expectation Maximization** (EM) algorithm [19].

Suppose we have collected a dataset of M traces where each trace $\mathbf{Y}^{(j)}$ has a different complex amplitude $A^{(j)}$ but all share the same signal template \mathbf{S} as well as noise distribution. Then we can construct the χ^2 over the entire dataset:

$$\chi^2 = \sum_{j=1}^M (\mathbf{Y}^{(j)} - A^{(j)}\mathbf{S})^\dagger \mathbf{C}^{-1} (\mathbf{Y}^{(j)} - A^{(j)}\mathbf{S}) \quad (\text{B.31})$$

The algorithm works as follows. First we initialize a random trial template and then perform the E-step of the EM algorithm. The E-step proceeds exactly the same as normal OF, where we fix the template \mathbf{S} and optimize the coefficients $A^{(j)}$:

$$\frac{\partial \chi^2}{\partial A^{(j)}} = 0 \quad (\text{B.32})$$

$$(\mathbf{Y}^{(j)} - A^{(j)}\mathbf{S})^\dagger \mathbf{C}^{-1} \mathbf{S} = 0 \quad (\text{B.33})$$

$$A^{(j)} = \frac{\mathbf{S}^\dagger \mathbf{C}^{-1} \mathbf{Y}^{(j)}}{\mathbf{S}^\dagger \mathbf{C}^{-1} \mathbf{S}} \quad (\text{B.34})$$

This gives us an initial guess for the coefficients. Once we have the initial guess we perform the M-step where we fix the coefficients and optimize the template:

$$\frac{\partial \chi^2}{\partial \mathbf{S}} = 0 \quad (\text{B.35})$$

$$\sum_j (\mathbf{Y}^{(j)} - A^{(j)}\mathbf{S})^\dagger \mathbf{C}^{-1} A^{(j)} = 0 \quad (\text{B.36})$$

$$\sum_j \mathbf{Y}^{(j)} A^{(j)*} \mathbf{C}^{-1} = \mathbf{S} \sum_j |A^{(j)}|^2 \mathbf{C}^{-1} \quad (\text{B.37})$$

By solving this linear equation we can obtain our next iteration of the template. To improve convergence, at the end of this step the template is smoothed and normalized.

The optimality of this algorithm is guaranteed by the CRB since it is a linear model under the assumption that the true signal actually lies within the appropriate vector space, and that the EM procedure correctly converges to the true minima. Again, the CRB guarantees minimum variance only in the amplitude but not the phase. In other words we attain optimal resolution in pulse height but not necessarily time shift. We can also generalize this algorithm to include more freedom in pulse shape variation by having multiple templates. See [172] for further discussion.

Appendix C

Event Reconstruction with Machine Learning

In the larger SuperCDMS HV detectors we have multiple TES channels (figure C.1) which in principle allow us to reconstruct not only the energy deposited by the scattering event but also its position. While the energy can be estimated via the total sum of energy in all channels, it is not so clear how we can precisely reconstruct the event position. Various machine-learning based approaches has been explored and in this section we shall give an overview of work done in this direction.

C.1 Deep Convolutional Network

The most direct approach is to train a neural network on simulation data. This approach has been summarized in [163]. For an energy deposit with a certain energy and position we can simulate the resultant readout of the TES channels. We can encode the time traces from all the TES channels as a 2D image (figure C.2) and then train a deep convolutional neural network with the energy and position as the output of the neural network similar to that demonstrated in [48]. However the performance of the trained model greatly suffers when we apply to real data due to severe distribution shift between training data, which is generated from simulation, and real experimental data, which can look quite different from simulation (different fall/rise times, saturation, glitches, etc.).

Before this approach can be practical we need to continue to improve and calibrate the simulation against real data until the two look similar. However given the flexibility of the neural network, the

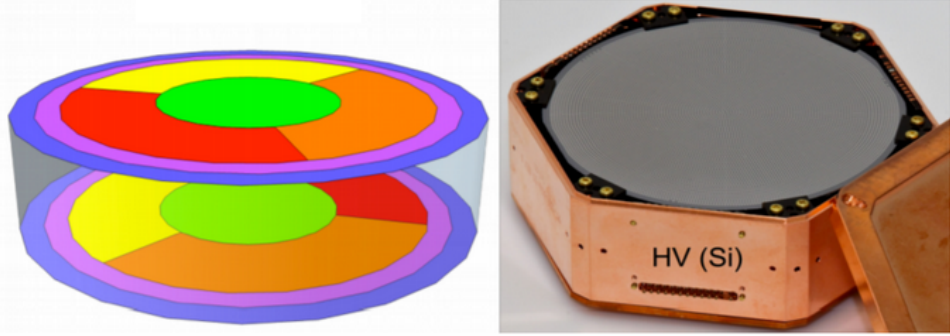


Figure C.1: Channel map of the SuperCDMS HV detector. Shown colored are the 12 TES channels.

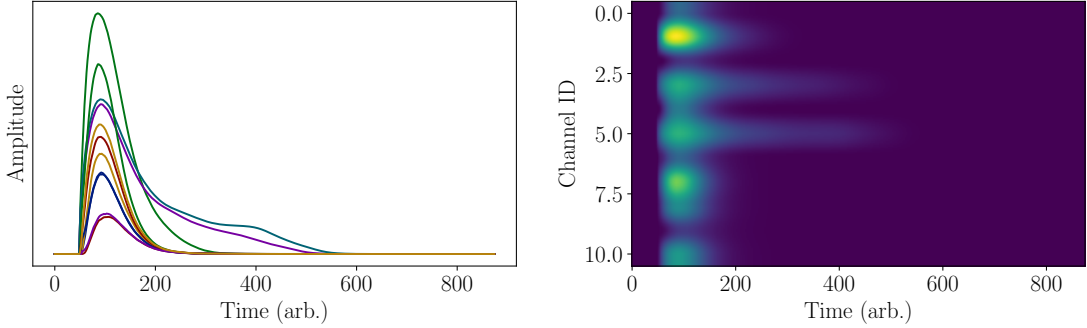


Figure C.2: Detector readout from each TES channels shown as time traces (left), and 2D image (right) in which the pixel brightness represents the amplitude. The 2D image is used as input to the convolutional neural network described in [163].

trained network may still latch onto any residual differences between real data and simulation. This can potentially be alleviated via the reverse gradient propagation described in [54] where one trains a real data vs simulation discriminator simultaneously and back-propagate the reverse gradient of the discriminator to suppress the main network's ability to use any features that are specific only to simulation (e.g. simulation artifacts) or only to real data (e.g. glitches). Even so it is likely that the trained model will not be very robust against any changes in the noise environment or individual detector differences.

C.2 Neural Ordinary Differential Equations

The lack of robustness ultimately stems from the fact that we are trying to map from a very high dimensional input (10000 readings for 12 channels and 1024 time steps) to a very low dimensional output (4 numbers for energy and 3D position). The high degree of degeneracy means that it is unlikely that the trained model will correctly learn all the physics and thus be fully generalized.

Instead of learning the direct mapping from trace to reconstructed quantities, a better approach would be to learn the dynamics of the system [36] which is much more constrained. To be specific, let us consider just one TES channel. We learn the mapping that takes the TES reading at one time step x_t to the next time step x_{t+1} via

$$x_t = F(x_{t+1}) + I_t \quad (\text{C.1})$$

where I is the external impulse that we want to reconstruct and the function F is learned via neural network. This neural network now only has a single input and a single output which is much less degenerate.

This approach has the following advantages compared to the first approach:

1. The behavior of the neural net is completely transparent since we can simply plot F .
2. The neural network can be trained directly using real data since we only need time traces. Pretraining with simulation data would help but is not strictly necessary. We can even jump start with traces generated from a simple TES model.
3. The neural network can be easily recalibrated by fine-tuning on time traces whenever the noise environment or detector parameters has changed.

Once F has been learned from data, we can freeze the weights and find I which is the impulse function we want to reconstruct. This can be achieved by back-propagation of the same loss function as well.

In practice, we can either perform this procedure on a per-channel basis, or treat the amplitude of the 12 channels as a single \mathbf{x} . Furthermore since we do not directly observe all the TES variables (e.g. we do not know the temperature directly) we should include some additional latent variables in order to accommodate the latent dynamics. This is called augmented neural ODE (ANODE) [46, 176]. This seems to be a very promising approach which still requires further study.

Bibliography

- [1] Pwscf user's guide. https://www.quantum-espresso.org/Doc/user_guide/. Accessed: 2022-11-15.
- [2] Pw.x input guide. https://www.quantum-espresso.org/Doc/INPUT_PW.html. Accessed: 2022-11-15.
- [3] qe-erf2. <https://github.com/ytcs/qe-erf2>. Accessed: 2022-11-15.
- [4] User's guide for quantum espresso. https://www.quantum-espresso.org/Doc/pw_user_guide/. Accessed: 2022-11-15.
- [5] 2018. Updated limit provided by F. Reindl in private communication, paper in prep.
- [6] Nabila Aghanim, Yashar Akrami, Mark Ashdown, J Aumont, C Baccigalupi, M Ballardini, AJ Banday, RB Barreiro, N Bartolo, S Basak, et al. Planck 2018 results-vi. cosmological parameters. *Astronomy & Astrophysics*, 641:A6, 2020.
- [7] R Agnese, AJ Anderson, T Aramaki, I Arnquist, W Baker, D Barker, R Basu Thakur, DA Bauer, A Borgland, MA Bowles, et al. Projected sensitivity of the supercdms snolab experiment. *Physical Review D*, 95(8):082002, 2017.
- [8] F. Ajzenberg-Selove. Energy levels of light nuclei $a = 13\text{--}15$. *Nuclear Physics A*, 523(1):1 – 196, 1991.
- [9] Musaab Al-Bakry, Imran Alkhatib, Dorian Praia do Amaral, Taylor Aralis, Tsuguo Aramaki, Isaac Arnquist, Iman Ataee Langroud, Elham Azadbakht, Samir Banik, Corey Bathurst, et al. A search for low-mass dark matter via bremsstrahlung radiation and the migdal effect in supercdms. *arXiv preprint arXiv:2203.02594*, 2022.
- [10] Haipeng An, Maxim Pospelov, and Josef Pradler. Dark matter detectors as dark photon helioscopes. *Physical review letters*, 111(4):041302, 2013.

- [11] Haipeng An, Maxim Pospelov, and Josef Pradler. New stellar constraints on dark photons. *Physics Letters B*, 725(4-5):190–195, 2013.
- [12] Philip Warren Anderson. Localized magnetic states in metals. *Physical Review*, 124(1):41, 1961.
- [13] G. Angloher, P. Bauer, A. Bento, C. Bucci, L. Canonica, X. Defay, A. Erb, F. v. Feilitzsch, N. Ferreiro Iachellini, P. Gorla, A. Gütlein, D. Hauff, J. Jochum, M. Kiefer, H. Kluck, H. Kraus, J. C. Lanfranchi, A. Langenkämper, J. Loebell, M. Mancuso, E. Mondragon, A. Münster, L. Oberauer, C. Pagliarone, F. Petricca, W. Potzel, F. Pröbst, R. Puig, F. Reindl, J. Rothe, K. Schäffner, J. Schieck, S. Schönert, W. Seidel, M. Stahlberg, L. Stodolsky, C. Strandhagen, R. Strauss, A. Tanzke, H. H. Trinh Thi, C. Türkoğlu, M. Uffinger, A. Ulrich, I. Usherov, S. Wawoczny, M. Willers, M. Wüstrich, and A. Zöller. Results on MeV-scale dark matter from a gram-scale cryogenic calorimeter operated above ground. *European Physical Journal C*, 77:637, September 2017.
- [14] E. Aprile, J. Aalbers, F. Agostini, M. Alfonsi, L. Althueser, F. D. Amaro, M. Anthony, F. Arneodo, L. Baudis, B. Bauermeister, M. L. Benabderrahmane, T. Berger, P. A. Breur, A. Brown, A. Brown, E. Brown, S. Bruenner, G. Bruno, R. Budnik, C. Capelli, J. M. R. Cardoso, D. Cichon, D. Coderre, A. P. Colijn, J. Conrad, J. P. Cussonneau, M. P. Decowski, P. de Perio, P. di Gangi, A. di Giovanni, S. Diglio, A. Elykov, G. Eurin, J. Fei, A. D. Ferella, A. Fieguth, W. Fulgione, A. Gallo Rosso, M. Galloway, F. Gao, M. Garbini, C. Geis, L. Grandi, Z. Greene, H. Qiu, C. Hasterok, E. Hogenbirk, J. Howlett, R. Itay, F. Joerg, B. Kaminsky, S. Kazama, A. Kish, G. Koltman, H. Landsman, R. F. Lang, L. Levinson, Q. Lin, S. Lindemann, M. Lindner, F. Lombardi, J. A. M. Lopes, J. Mahlstedt, A. Manfredini, T. Marrodán Undagoitia, J. Masbou, D. Masson, M. Messina, K. Micheneau, K. Miller, A. Molinario, K. Morâ, M. Murra, J. Naganoma, K. Ni, U. Oberlack, B. Pelssers, F. Piastra, J. Pienaar, V. Pizzella, G. Plante, R. Podviianiuk, N. Priel, D. Ramírez García, L. Rauch, S. Reichard, C. Reuter, B. Riedel, A. Rizzo, A. Rocchetti, N. Rupp, J. M. F. Dos Santos, G. Sartorelli, M. Scheibelhut, S. Schindler, J. Schreiner, D. Schulte, M. Schumann, L. Scotto Lavina, M. Selvi, P. Shagin, E. Shockley, M. Silva, H. Simgen, D. Thers, F. Toschi, G. Trinchero, C. Tunnell, N. Upole, M. Vargas, O. Wack, H. Wang, Z. Wang, Y. Wei, C. Weinheimer, C. Wittweg, J. Wulf, J. Ye, Y. Zhang, T. Zhu, and Xenon Collaboration. Dark Matter Search Results from a One Ton-Year Exposure of XENON1T., 121:111302, September 2018.
- [15] Elena Aprile, Jelle Aalbers, F Agostini, M Alfonsi, L Althueser, FD Amaro, Vasile C Antochi, E Angelino, F Arneodo, Derek Barge, et al. Search for light dark matter interactions enhanced

- by the migdal effect or bremsstrahlung in xenon1t. *Physical review letters*, 123(24):241803, 2019.
- [16] Neil W Ashcroft and N David Mermin. *Solid state physics*. Cengage Learning, 2022.
 - [17] Wilfried G. Aulbur, Lars Jönsson, and John W. Wilkins. Quasiparticle calculations in solids. volume 54 of *Solid State Physics*, pages 1 – 218. Academic Press, 2000.
 - [18] Howard Baer, Ki-Young Choi, Jihn E Kim, and Leszek Roszkowski. Dark matter production in the early universe: beyond the thermal wimp paradigm. *Physics Reports*, 555:1–60, 2015.
 - [19] Stephen Bailey. Principal component analysis with noisy and/or missing data. *Publications of the Astronomical Society of the Pacific*, 124(919):1015, 2012.
 - [20] C Bareille, FL Boariu, H Schwab, P Lejay, F Reinert, and AF Santander-Syro. Momentum-resolved hidden-order gap reveals symmetry breaking and origin of entropy loss in . *Nature Communications*, 5(1):1–11, 2014.
 - [21] A. L. Barry, B. Lehmann, D. Fritsch, and D. Braunig. Energy dependence of electron damage and displacement threshold energy in 6H silicon carbide. *IEEE Transactions on Nuclear Science*, 38(6):1111–1115, 1991.
 - [22] Matthew J Beck, L Tsetseris, and ST Pantelides. Stability and dynamics of frenkel pairs in si. *Physical review letters*, 99(21):215503, 2007.
 - [23] Douglas A Bennett, Daniel S Swetz, Daniel R Schmidt, and Joel N Ullom. Resistance in transition-edge sensors: A comparison of the resistively shunted junction and two-fluid models. *Physical Review B*, 87(2):020508, 2013.
 - [24] G. W. Bennett, B. Bousquet, H. N. Brown, G. Bunce, R. M. Carey, P. Cushman, G. T. Danby, P. T. Debevec, M. Deile, H. Deng, W. Deninger, S. K. Dhawan, V. P. Druzhinin, L. Duong, E. Efstathiadis, F. J. M. Farley, G. V. Fedotovich, S. Giron, F. E. Gray, D. Grigoriev, M. Grosse-Perdekamp, A. Grossmann, M. F. Hare, D. W. Hertzog, X. Huang, V. W. Hughes, M. Iwasaki, K. Jungmann, D. Kawall, M. Kawamura, B. I. Khazin, J. Kindem, F. Krienen, I. Kronkvist, A. Lam, R. Larsen, Y. Y. Lee, I. Logashenko, R. McNabb, W. Meng, J. Mi, J. P. Miller, Y. Mizumachi, W. M. Morse, D. Nikas, C. J. G. Onderwater, Y. Orlov, C. S. Özben, J. M. Paley, Q. Peng, C. C. Polly, J. Pretz, R. Prigl, G. zu Putlitz, T. Qian, S. I. Redin, O. Rind, B. L. Roberts, N. Ryskulov, S. Sedykh, Y. K. Semertzidis, P. Shagin, Yu. M. Shatunov, E. P. Sichtermann, E. Solodov, M. Sossong, A. Steinmetz, L. R. Sulak, C. Timmermans, A. Trofimov, D. Urner, P. von Walter, D. Warburton, D. Winn, A. Yamamoto, and

- D. Zimmerman. Final report of the e821 muon anomalous magnetic moment measurement at BNL. *Physical Review D*, 73(7), apr 2006.
- [25] Gianfranco Bertone. *Particle dark matter: observations, models and searches*. Cambridge University Press, 2010.
- [26] Gianfranco Bertone and Dan Hooper. History of dark matter. *Reviews of Modern Physics*, 90(4):045002, 2018.
- [27] G. Bertuccio and R. Casiraghi. Study of silicon carbide for x-ray detection and spectroscopy. *IEEE Transactions on Nuclear Science*, 50(1):175–185, Feb 2003.
- [28] J. Billard, E. Figueroa-Feliciano, and L. Strigari. Implication of neutrino backgrounds on the reach of next generation dark matter direct detection experiments. *Phys. Rev. D*, 89:023524, Jan 2014.
- [29] Itay M Bloch, Rouven Essig, Kohsaku Tobioka, Tomer Volansky, and Tien-Tien Yu. Searching for dark absorption with direct detection experiments. *Journal of High Energy Physics*, 2017(6):1–21, 2017.
- [30] Svetlana V Boriskina, Thomas Alan Cooper, Lingping Zeng, George Ni, Jonathan K Tong, Yoichiro Tsurimaki, Yi Huang, Laureen Meroueh, Gerald Mahan, and Gang Chen. Losses in plasmonics: from mitigating energy dissipation to embracing loss-enabled functionalities. *Advances in Optics and Photonics*, 9(4):775–827, 2017.
- [31] Joseph Callaway. Model for lattice thermal conductivity at low temperatures. *Phys. Rev.*, 113:1046–1051, Feb 1959.
- [32] Xavier Calmet and Folkert Kuipers. Theoretical bounds on dark matter masses. *Physics Letters B*, 814:136068, 2021.
- [33] Xavier Calmet and Nathaniel Sherrill. Implications of quantum gravity for dark matter searches with atom interferometers. *Universe*, 8(2):103, 2022.
- [34] Brian Campbell-Deem, Peter Cox, Simon Knapen, Tongyan Lin, and Tom Melia. Multiphonon excitations from dark matter scattering in crystals. *Phys. Rev. D*, 101(3):036006, 2020.
- [35] C. Canali, M. Martini, G. Ottaviani, and A. A. Quaranta. Measurements of the average energy per electron-hole pair generation in silicon between 5-320k. *IEEE Transactions on Nuclear Science*, 19(4):9–19, Aug 1972.

- [36] Ricky TQ Chen, Yulia Rubanova, Jesse Bettencourt, and David K Duvenaud. Neural ordinary differential equations. *Advances in neural information processing systems*, 31, 2018.
- [37] Piers Coleman. Heavy fermions and the kondo lattice: a 21st century perspective. 2015.
- [38] CRESST collaboration, F. Petricca, G. Angloher, P. Bauer, A. Bento, C. Bucci, L. Canonica, X. Defay, A. Erb, F. v. Feilitzsch, N. Ferreiro Iachellini, P. Gorla, A. Gütlein, D. Hauff, J. Jochum, M. Kiefer, H. Kluck, H. Kraus, J. C. Lanfranchi, A. Lagenkämper, J. Loebell, M. Mancuso, E. Mondragon, A. Münster, C. Pagliarone, W. Potzel, F. Pröbst, R. Puig, F. Reindl, J. Rothe, K. Schäffner, J. Schieck, S. Schönert, W. Seidel, M. Stahlberg, L. Stodolsky, C. Strandhagen, R. Strauss, A. Tanzke, H. H. Trinh Thi, C. Türkoğlu, A. Ulrich, I. Usherov, S. Wawoczny, M. Willers, and M. Wüstrich. First results on low-mass dark matter from the CRESST-III experiment. *ArXiv e-prints*, page arXiv:1711.07692, November 2017.
- [39] P Cushman, C Galbiati, DN McKinsey, H Robertson, TMP Tait, D Bauer, A Borgland, B Cabrera, F Calaprice, J Cooley, et al. Snowmass cf1 summary: Wimp dark matter direct detection. *arXiv preprint arXiv:1310.8327*, 2013.
- [40] Syamal Kumar Dana, Dipendra Chandra Sengupta, and Kossi D Edoh. Chaotic dynamics in josephson junction. *IEEE Transactions on Circuits and Systems I: Fundamental Theory and Applications*, 48(8):990–996, 2001.
- [41] Leonardo Degiorgi, MB Hunt, Hans Rudolf Ott, Martin Dressel, Bokke Johannes Feenstra, George Grüner, Zachary Fisk, and P Canfield. Optical evidence of anderson-mott localization in fesi. *EPL (Europhysics Letters)*, 28(5):341, 1994.
- [42] Martin Dressel and George Grüner. Electrodynamics of solids: optical properties of electrons in matter, 2002.
- [43] Mildred Dresselhaus, Gene Dresselhaus, Stephen B Cronin, and A Gomes Souza Filho. Solid state properties. *Alemania: Springer-Verlag*, 2018.
- [44] Andrzej K. Drukier, Sebastian Baum, Katherine Freese, Maciej Górska, and Patrick Stengel. Paleo-detectors: Searching for dark matter with ancient minerals. *Phys. Rev. D*, 99:043014, Feb 2019.
- [45] Peizhi Du. Direct detection of sub-mev dark matter with doped semiconductors. BSM PAN-DEMIC Delta Series, 2021.

- [46] Emilien Dupont, Arnaud Doucet, and Yee Whye Teh. Augmented neural odes. *Advances in Neural Information Processing Systems*, 32, 2019.
- [47] Eberhard Engel and Reiner M Dreizler. Density functional theory. *Theoretical and Mathematical Physics*, pages 351–399, 2011.
- [48] Martin Erdmann, Jonas Glombitza, and David Walz. A deep learning-based reconstruction of cosmic ray-induced air showers. *Astroparticle Physics*, 97:46–53, 2018.
- [49] Rouven Essig, Marivi Fernandez-Serra, Jeremy Mardon, Adrian Soto, Tomer Volansky, and Tien-Tien Yu. Direct detection of sub-gev dark matter with semiconductor targets. *Journal of High Energy Physics*, 2016(5):1–54, 2016.
- [50] Rouven Essig, Jesús Pérez-Ríos, Harikrishnan Ramani, and Oren Slone. Direct detection of nuclear scattering of sub-gev dark matter using molecular excitations. *Physical Review Research*, 1(3):033105, 2019.
- [51] Marco Fabbrichesi, Emidio Gabrielli, and Gaia Lanfranchi. *The Physics of the Dark Photon: A Primer*. Springer, 2021.
- [52] Lukas J Fiderer and Daniel Braun. Quantum metrology with quantum-chaotic sensors. *Nature communications*, 9(1):1–9, 2018.
- [53] A Liam Fitzpatrick, Wick Haxton, Emanuel Katz, Nicholas Lubbers, and Yiming Xu. The effective field theory of dark matter direct detection. *Journal of Cosmology and Astroparticle Physics*, 2013(02):004, 2013.
- [54] Yaroslav Ganin and Victor Lempitsky. Unsupervised domain adaptation by backpropagation. In *International conference on machine learning*, pages 1180–1189. PMLR, 2015.
- [55] Fei Gao and William J Weber. Recovery of close frenkel pairs produced by low energy recoils in sic. *Journal of applied physics*, 94(7):4348–4356, 2003.
- [56] William A Gardner. Cyclostationarity in communications and signal processing. Technical report, STATISTICAL SIGNAL PROCESSING INC YOUNTVILLE CA, 1994.
- [57] R. Matthias Geilhufe, Felix Kahlhoefer, and Martin Wolfgang Winkler. Dirac materials for sub-mev dark matter detection: New targets and improved formalism. *Physical Review D*, 101(5), Mar 2020.
- [58] Paolo Giannozzi, Stefano Baroni, Nicola Bonini, Matteo Calandra, Roberto Car, Carlo Cavazzoni, Davide Ceresoli, Guido L Chiarotti, Matteo Cococcioni, Ismaila Dabo, et al. Quantum

- espresso: a modular and open-source software project for quantum simulations of materials. *Journal of physics: Condensed matter*, 21(39):395502, 2009.
- [59] Steven M Girvin and Kun Yang. *Modern condensed matter physics*. Cambridge University Press, 2019.
- [60] C. J. Glassbrenner and Glen A. Slack. Thermal conductivity of silicon and germanium from 3k to the melting point. *Phys. Rev.*, 134:A1058–A1069, May 1964.
- [61] Sinéad M Griffin, Yonit Hochberg, Katherine Inzani, Noah Kurinsky, Tongyan Lin, and To Chin Yu. Silicon carbide detectors for sub-gev dark matter. *Physical Review D*, 103(7):075002, 2021.
- [62] Sinéad M Griffin, Katherine Inzani, Tanner Trickle, Zhengkang Zhang, and Kathryn M Zurek. Multichannel direct detection of light dark matter: Target comparison. *Physical Review D*, 101(5):055004, 2020.
- [63] Sinéad M Griffin, Katherine Inzani, Tanner Trickle, Zhengkang Zhang, and Kathryn M Zurek. Extended calculation of dark matter-electron scattering in crystal targets. *Physical Review D*, 104(9):095015, 2021.
- [64] G. L. Harris. *Properties of Silicon Carbide (E M I S Datareviews Series)*. IEE, 1995.
- [65] S. A. Hertel, A. Biekert, J. Lin, V. Velan, and D. N. McKinsey. A Path to the Direct Detection of sub-GeV Dark Matter Using Calorimetric Readout of a Superfluid ^4He Target. *arXiv e-prints*, page arXiv:1810.06283, October 2018.
- [66] Alexander Cyril Hewson. *Models of Magnetic Impurities*. Cambridge Studies in Magnetism. Cambridge University Press, 1993.
- [67] Hideo Hirayama. Lecture note on photon interactions and cross sections. *KEK, High Energy Accelerator Research Organization, Oho, Tsukuba, Ibaraki, Japan*, 2000.
- [68] Yonit Hochberg, Yonatan Kahn, Noah Kurinsky, Benjamin V Lehmann, To Chin Yu, and Karl K Berggren. Determining dark-matter-electron scattering rates from the dielectric function. *Physical review letters*, 127(15):151802, 2021.
- [69] Yonit Hochberg, Yonatan Kahn, Mariangela Lisanti, Kathryn M Zurek, Adolfo G Grushin, Roni Ilan, Sinéad M Griffin, Zhen-Fei Liu, Sophie F Weber, and Jeffrey B Neaton. Detection of sub-mev dark matter with three-dimensional dirac materials. *Physical Review D*, 97(1):015004, 2018.

- [70] Yonit Hochberg, Tongyan Lin, and Kathryn M Zurek. Absorption of light dark matter in semiconductors. *Physical Review D*, 95(2):023013, 2017.
- [71] Yonit Hochberg, Matt Pyle, Yue Zhao, and Kathryn M Zurek. Detecting superlight dark matter with fermi-degenerate materials. *Journal of High Energy Physics*, 2016(8):1–44, 2016.
- [72] Yonit Hochberg, Belina von Krosigk, Eric Kuflik, and To Chin Yu. Impact of dark compton scattering on direct dark matter absorption searches. *Physical Review Letters*, 128(19):191801, 2022.
- [73] Martin Hoferichter, Philipp Klos, Javier Menéndez, and Achim Schwenk. Nuclear structure factors for general spin-independent wimp-nucleus scattering. *Phys. Rev. D*, 99:055031, Mar 2019.
- [74] P. Hohenberg and W. Kohn. Inhomogeneous electron gas. *Phys. Rev.*, 136:B864–B871, Nov 1964.
- [75] Bob Holdom. Two u (1)’s and charge shifts. *Physics Letters B*, 166(2):196–198, 1986.
- [76] Dan Hooper, Rebecca K Leane, Yu-Dai Tsai, Shalma Wegsman, and Samuel J Witte. A systematic study of hidden sector dark matter: application to the gamma-ray and antiproton excesses. *Journal of High Energy Physics*, 2020(7):1–38, 2020.
- [77] MB Hunt, MA Chernikov, E Felder, HR Ott, Z Fisk, and P Canfield. Low-temperature magnetic, thermal, and transport properties of fesi. *Physical Review B*, 50(20):14933, 1994.
- [78] A. V. Inyushkin, A. N. Taldenkov, V. G. Ralchenko, A. P. Bolshakov, A. V. Koliadin, and A. N. Katrusha. Thermal conductivity of high purity synthetic single crystal diamonds. *Phys. Rev. B*, 97:144305, Apr 2018.
- [79] Kent D Irwin and Gene C Hilton. Transition-edge sensors. In *Cryogenic particle detection*, pages 63–150. Springer, 2005.
- [80] Jan Isberg, Johan Hammersberg, Erik Johansson, Tobias Wikström, Daniel J. Twitchen, Andrew J. Whitehead, Steven E. Coe, and Geoffrey A. Scarsbrook. High carrier mobility in single-crystal plasma-deposited diamond. *Science*, 297(5587):1670–1672, 2002.
- [81] Alexander M. Ivanov, Evgenia V. Kalinina, G. Kholuyanov, Nikita B. Strokan, G. Onushkin, Andrey O. Konstantinov, Anders Hallén, and Andrej Yu. Kuznetsov. High energy resolution detectors based on 4h-sic. In *Silicon Carbide and Related Materials 2004*, volume 483 of *Materials Science Forum*, pages 1029–1032. Trans Tech Publications Ltd, 2 2005.

- [82] Carlo Jacoboni and Lino Reggiani. The monte carlo method for the solution of charge transport in semiconductors with applications to covalent materials. *Rev. Mod. Phys.*, 55:645–705, Jul 1983.
- [83] Daniel Jardin. A likelihood search for low-mass dark matter via inelastic scattering in supercdms. Technical report, Fermi National Accelerator Lab.(FNAL), Batavia, IL (United States), 2019.
- [84] Fedja Kadribasic, Nader Mirabolfathi, Kai Nordlund, and Flyura Djurabekova. Crystal defects: A portal to dark matter detection. *arXiv preprint arXiv:2002.03525*, 2020.
- [85] Yonatan Kahn, Gordan Krnjaic, and Bashi Mandava. Dark matter detection with bound nuclear targets: The poisson phonon tail. *Physical review letters*, 127(8):081804, 2021.
- [86] Yonatan Kahn and Tongyan Lin. Searches for light dark matter using condensed matter systems. *Reports on Progress in Physics*, 2022.
- [87] Steven B Kaplan. Acoustic matching of superconducting films to substrates. *Journal of Low Temperature Physics*, 37(3):343–365, 1979.
- [88] Georgia Karagiorgi, Gregor Kasieczka, Scott Kravitz, Benjamin Nachman, and David Shih. Machine learning in the search for new fundamental physics. *Nature Reviews Physics*, 4(6):399–412, 2022.
- [89] Steven M Kay. *Fundamentals of statistical signal processing: estimation theory*. Prentice-Hall, Inc., 1993.
- [90] Alex Keshavarzi, Kim Siang Khaw, and Tamaki Yoshioka. Muon g- 2: a review. *Nuclear Physics B*, page 115675, 2022.
- [91] Alexander Khintchine. Korrelationstheorie der stationären stochastischen prozesse. *Mathematische Annalen*, 109(1):604–615, 1934.
- [92] Tsunenobu Kimoto, editor. *Physical Properties of Silicon Carbide*, chapter 2, pages 11–38. John Wiley & Sons, Ltd, 2014.
- [93] Claude A. Klein. Bandgap dependence and related features of radiation ionization energies in semiconductors. *Journal of Applied Physics*, 39(4):2029–2038, 1968.
- [94] O. Klein and Y. Nishina. *On the Scattering of Radiation by Free Electrons According to Dirac's New Relativistic Quantum Dynamics*, pages 113–129. 1994.

- [95] Simon Knapen, Jonathan Kozaczuk, and Tongyan Lin. Dark matter-electron scattering in dielectrics. *Physical Review D*, 104(1):015031, 2021.
- [96] Simon Knapen, Jonathan Kozaczuk, and Tongyan Lin. Migdal effect in semiconductors. *Physical Review Letters*, 127(8):081805, 2021.
- [97] Simon Knapen, Tongyan Lin, and Kathryn M. Zurek. Light Dark Matter in Superfluid Helium: Detection with Multi-excitation Production. *Phys. Rev.*, D95(5):056019, 2017.
- [98] J. Koike, D. M. Parkin, and T. E. Mitchell. Displacement threshold energy for type iiA diamond. *Applied Physics Letters*, 60(12):1450–1452, 1992.
- [99] Chris Kouvaris and Josef Pradler. Probing sub-gev dark matter with conventional detectors. *Physical Review Letters*, 118(3):031803, 2017.
- [100] N. Kurinsky, P. Brink, B. Cabrera, R. Partridge, M. Pyle, and SuperCDMS Collaboration. SuperCDMS SNOLAB Low-Mass Detectors: Ultra-Sensitive Phonon Calorimeters for a Sub-GeV Dark Matter Search. In *Proceedings of the 38th International Conference on High Energy Physics (ICHEP2016). 3-10 August 2016. Chicago*, page 1116, January 2016.
- [101] Noah Kurinsky. *The low-mass limit: Dark matter detectors with eV-scale energy resolution*. Stanford University, 2018.
- [102] Noah Kurinsky, To Chin Yu, Yonit Hochberg, and Blas Cabrera. Diamond detectors for direct detection of sub-gev dark matter. *Physical Review D*, 99(12):123005, 2019.
- [103] M.I. Landstrass, M.A. Plano, M.A. Moreno, S. McWilliams, L.S. Pan, D.R. Kania, and S. Han. Device properties of homoepitaxially grown diamond. *Diamond and Related Materials*, 2(5):1033 – 1037, 1993. Diamond 1992.
- [104] Robert Lasenby and Anirudh Prabhu. Dark matter-electron scattering in materials: Sum rules and heterostructures. *Physical Review D*, 105(9):095009, 2022.
- [105] A. A. Lebedev, N. S. Savkina, A. M. Ivanov, N. B. Strokan, and D. V. Davydov. 6H-SiC epilayers as nuclear particle detectors. *Semiconductors*, 34(2):243–249, 2000.
- [106] Benjamin W Lee and Steven Weinberg. Cosmological lower bound on heavy-neutrino masses. *Physical Review Letters*, 39(4):165, 1977.
- [107] Song Li, Yang Xiao, and Jin Min Yang. A pedagogical review on muon $g - 2$. *arXiv preprint arXiv:2110.04673*, 2021.

- [108] Zheng-Liang Liang, Chongjie Mo, Fawei Zheng, and Ping Zhang. Describing the migdal effect with a bremsstrahlung-like process and many-body effects. *Physical Review D*, 104(5):056009, 2021.
- [109] Tongyan Lin. Tasi lectures on dark matter models and direct detection. *arXiv preprint arXiv:1904.07915*, 2019.
- [110] Mark Anton Lindeman. *Microcalorimetry and the transition-edge sensor*. University of California, Davis, 2000.
- [111] Jens Lindhard, V Nielsen, M Scharff, and PV Thomsen. Integral equations governing radiation effects. *Mat. Fys. Medd. Dan. Vid. Selsk*, 33(10):1–42, 1963.
- [112] A. E. Litherland, H. E. Gove, R. P. Beukens, X.-L. Zhao, and W. E. Kieser. Low-level ^{14}C measurements and accelerator mass spectrometry. *AIP Conference Proceedings*, 785(1):48–56, 2005.
- [113] C-P Liu, Chih-Pan Wu, Hsin-Chang Chi, and Jiunn-Wei Chen. Model-independent determination of the migdal effect via photoabsorption. *Physical Review D*, 102(12):121303, 2020.
- [114] I-Te Lu and Marco Bernardi. Using defects to store energy in materials—a computational study. *Scientific reports*, 7(1):1–8, 2017.
- [115] G. Lucas and L. Pizzagalli. Ab initio molecular dynamics calculations of threshold displacement energies in silicon carbide. *Phys. Rev. B*, 72:161202, Oct 2005.
- [116] Guillaume Lucas and Laurent Pizzagalli. Theoretical study of the recombination of frenkel pairs in irradiated silicon carbide. *Journal of Physics: Condensed Matter*, 19(8):086208, 2007.
- [117] A Lushchik, Ch Lushchik, V Nagirnyi, E Shablonin, and E Vasil’chenko. Low-temperature creation of frenkel defects via hot electron-hole recombination in highly pure nacl single crystals. *Low Temperature Physics*, 42(7):547–551, 2016.
- [118] Richard M Martin, Lucia Reining, and David M Ceperley. *Interacting electrons*. Cambridge University Press, 2016.
- [119] Dan McCammon. Thermal equilibrium calorimeters—an introduction. In *Cryogenic particle detection*, pages 1–34. Springer, 2005.
- [120] Andrea Mitridate, Tanner Trickle, Zhengkang Zhang, and Kathryn M Zurek. Detectability of axion dark matter with phonon polaritons and magnons. *Physical Review D*, 102(9):095005, 2020.

- [121] Andrea Mitridate, Tanner Trickle, Zhengkang Zhang, and Kathryn M Zurek. Dark matter absorption via electronic excitations. *Journal of High Energy Physics*, 2021(9):1–39, 2021.
- [122] Bartomeu Monserrat and R. J. Needs. Comparing electron-phonon coupling strength in diamond, silicon, and silicon carbide: First-principles study. *Physical Review B*, 89(21), Jun 2014.
- [123] Tamar More and Humphrey J Maris. Directionality from anisotropic phonon production in solid state dark matter detection. *Journal of Low Temperature Physics*, 93(3):387–392, 1993.
- [124] H Muramatsu, T Hayashi, N Yuasa, R Konno, A Yamaguchi, K Mitsuda, NY Yamasaki, K Maehata, H Kikunaga, M Takimoto, et al. Optimized tes microcalorimeters with 14 ev energy resolution at 30 kev for γ -ray measurements of the 229th isomer. *Journal of Low Temperature Physics*, 200(5):452–460, 2020.
- [125] H. Mutschke, A. C. Andersen, D. Clement, Th. Henning, and G. Peiter. Infrared properties of SiC particles, 1999.
- [126] K Nagayoshi, ML Ridder, MP Bruijn, L Gottardi, E Taralli, P Khosropanah, H Akamatsu, S Visser, and J-R Gao. Development of a ti/au tes microcalorimeter array as a backup sensor for the athena/x-ifu instrument. *Journal of Low Temperature Physics*, 199(3):943–948, 2020.
- [127] F Nava, G Bertuccio, A Cavallini, and E Vittone. Silicon carbide and its use as a radiation detector material. *Measurement Science and Technology*, 19(10):102001, aug 2008.
- [128] Lina Necib. Boosting (in) direct detection of dark matter. *arXiv preprint arXiv:1706.01137*, 2017.
- [129] Lina Necib, Mariangela Lisanti, and Vasily Belokurov. Inferred evidence for dark matter kinematic substructure with sdss–gaia. *The Astrophysical Journal*, 874(1):3, 2019.
- [130] A. J. Neves and M. H. Nazaré, editors. *Properties, Growth and Applications of Diamond*. INSPEC, 2001.
- [131] RC Newman. Defects in silicon. *Reports on Progress in Physics*, 45(10):1163, 1982.
- [132] P Nozieres and D Pines. Electron interaction in solids. characteristic energy loss spectrum. *Physical Review*, 113(5):1254, 1959.
- [133] SEA Orrigo, L Alvarez-Ruso, and C Peña-Garay. A new approach to nuclear form factors for direct dark matter searches. *Nuclear and particle physics proceedings*, 273:414–418, 2016.

- [134] S Paschen, E Felder, MA Chernikov, L Degiorgi, H Schwer, HR Ott, DP Young, JL Sarrao, and Z Fisk. Low-temperature transport, thermodynamic, and optical properties of fesi. *Physical Review B*, 56(20):12916, 1997.
- [135] Jaideep Pathak, Brian Hunt, Michelle Girvan, Zhixin Lu, and Edward Ott. Model-free prediction of large spatiotemporally chaotic systems from data: A reservoir computing approach. *Physical review letters*, 120(2):024102, 2018.
- [136] Michael E Peskin and Daniel V Schroeder. *An introduction to quantum field theory*. CRC press, 2018.
- [137] David Pines. Collective energy losses in solids. *Rev. Mod. Phys.*, 28:184–198, Jul 1956.
- [138] Maxim Pospelov, Adam Ritz, and Mikhail Voloshin. Bosonic super-wimps as kev-scale dark matter. *Physical Review D*, 78(11):115012, 2008.
- [139] Maxim Pospelov, Adam Ritz, and Mikhail Voloshin. Secluded wimp dark matter. *Physics Letters B*, 662(1):53–61, 2008.
- [140] Dimitur Ivanov Pushkarov. *Quasiparticle theory of defects in solids*. World scientific, 1991.
- [141] Matt Christopher Pyle. *Optimizing the design and analysis of cryogenic semiconductor dark matter detectors for maximum sensitivity*. Stanford University, 2012.
- [142] Chen-Kai Qiao, Hsin-Chang Chi, Shin-Ted Lin, Peng Gu, Shu-Kui Liu, and Chang-Jian Tang. Compton scattering energy spectrum for Si and Ge systems. *Journal of Physics G: Nuclear and Particle Physics*, 47(4):045202, 2020.
- [143] Surjeet Rajendran, Nicholas Zobrist, Alexander O Sushkov, Ronald Walsworth, and Mikhail Lukin. A method for directional detection of dark matter using spectroscopy of crystal defects. *Physical Review D*, 96(3):035009, 2017.
- [144] Karthik Ramanathan and Noah Kurinsky. Ionization yield in silicon for ev-scale electron-recoil processes. *Physical Review D*, 102(6):063026, 2020.
- [145] Peter S Riseborough. Heavy fermion semiconductors. *Advances in Physics*, 49(3):257–320, 2000.
- [146] R.-P. Riwar and G. Catelani. Efficient quasiparticle traps with low dissipation through gap engineering. *Phys. Rev. B*, 100:144514, Oct 2019.

- [147] R. K. Romani, P. L. Brink, B. Cabrera, M. Cherry, T. Howarth, N. Kurinsky, R. A. Moffatt, R. Partridge, F. Ponce, M. Pyle, A. Tomada, S. Yellin, J. J. Yen, and B. A. Young. Thermal detection of single e-h pairs in a biased silicon crystal detector. *Applied Physics Letters*, 112:043501, January 2018.
- [148] Vera C Rubin. A brief history of dark matter. *The dark universe: matter, energy and gravity*, pages 1–13, 2004.
- [149] Youssef Sarkis, Alexis Aguilar-Arevalo, and Juan Carlos D’Olivo. Study of the ionization efficiency for nuclear recoils in pure crystals. *Physical Review D*, 101(10):102001, 2020.
- [150] K Schneck, B Cabrera, DG Cerdeno, V Mandic, HE Rogers, R Agnese, AJ Anderson, M Asai, D Balakishiyeva, D Barker, et al. Dark matter effective field theory scattering in direct detection experiments. *Physical Review D*, 91(9):092004, 2015.
- [151] Marc Schumann. Direct detection of wimp dark matter: concepts and status. *Journal of Physics G: Nuclear and Particle Physics*, 46(10):103003, 2019.
- [152] Matthew D Schwartz. *Quantum field theory and the standard model*. Cambridge University Press, 2014.
- [153] Varley F. Sears. Neutron scattering lengths and cross sections. *Neutron News*, 3(3):26–37, 1992.
- [154] David S Sholl and Janice A Steckel. *Density functional theory: a practical introduction*. John Wiley & Sons, 2011.
- [155] Kyle Michael Sundqvist. *Carrier transport and related effects in detectors of the cryogenic dark matter search*. University of California, Berkeley, 2012.
- [156] SuperCDMS Collaboration, R. Agnese, T. Aralis, T. Aramaki, I. J. Arnquist, E. Azadbakht, W. Baker, S. Banik, D. Barker, D. A. Bauer, T. Binder, M. A. Bowles, P. L. Brink, R. Bunker, B. Cabrera, R. Calkins, R. A. Cameron, C. Cartaro, D. G. Cerdeño, Y. Y. Chang, J. Cooley, B. Cornell, P. Cushman, F. De Brienne, T. Doughty, E. Fascione, E. Figueroa- Feliciano, C. W. Fink, M. Fritts, G. Gerbier, R. Germond, M. Ghaith, S. R. Golwala, H. R. Harris, N. Herbert, Z. Hong, E. W. Hoppe, L. Hsu, M. E. Huber, V. Iyer, D. Jardin, A. Jastram, C. Jena, M. H. Kelsey, A. Kennedy, A. Kubik, N. A. Kurinsky, R. E. Lawrence, B. Loer, E. Lopez Asamar, P. Lukens, D. MacDonell, R. Mahapatra, V. Mandic, N. Mast, E. Miller, N. Mirabolfathi, B. Mohanty, J. D. Morales Mendoza, J. Nelson, H. Neog, J. L. Orrell, S. M. Oser, W. A. Page, R. Partridge, M. Pepin, F. Ponce, S. Poudel, M. Pyle, H. Qiu, W. Rau, A. Reisetter, R. Ren,

- T. Reynolds, A. Roberts, A. E. Robinson, H. E. Rogers, T. Saab, B. Sadoulet, J. Sander, A. Scarff, R. W. Schnee, S. Scorza, K. Senapati, B. Serfass, D. Speller, C. Stanford, M. Stein, J. Street, H. A. Tanaka, D. Toback, R. Underwood, A. N. Villano, B. von Krosigk, S. L. Watkins, J. S. Wilson, M. J. Wilson, J. Winchell, D. H. Wright, S. Yellin, B. A. Young, X. Zhang, and X. Zhao. Search for Low-Mass Dark Matter with CDMSlite Using a Profile Likelihood Fit. *arXiv e-prints*, page arXiv:1808.09098, August 2018.
- [157] AE Szymkowiak, RL Kelley, SH Moseley, and CK Stahle. Signal processing for microcalorimeters. *Journal of Low Temperature Physics*, 93(3):281–285, 1993.
- [158] The DarkSide Collaboration, P. Agnes, I. F. M. Albuquerque, T. Alexander, A. K. Alton, G. R. Araujo, D. M. Asner, M. Ave, H. O. Back, B. Baldin, G. Batignani, K. Biery, V. Bocci, G. Bonfini, W. Bonivento, B. Bottino, F. Budano, S. Bussino, M. Cadeddu, M. Cadoni, F. Calaprice, A. Caminata, N. Canci, A. Candela, M. Caravati, M. Cariello, M. Carlini, M. Carpinelli, S. Catalanotti, V. Cataudella, P. Cavalcante, S. Cavuoti, R. Cereseto, A. Chepurnov, C. Cicalò, L. Cifarelli, A. G. Cocco, G. Covone, D. D’Angelo, M. D’Incecco, D. D’Urso, S. Davini, A. De Candia, S. De Cecco, M. De Deo, G. De Filippis, G. De Rosa, M. De Vincenzi, P. Demontis, A. V. Derbin, A. Devoto, F. Di Eusonio, G. Di Pietro, C. Dionisi, M. Downing, E. Edkins, A. Empl, A. Fan, G. Fiorillo, K. Fomenko, D. Franco, F. Gabriele, A. Gabrieli, C. Galbiati, P. Garcia Abia, C. Ghiano, S. Giagu, C. Giganti, G. K. Giovanetti, O. Gorshakov, A. M. Goretti, F. Granato, M. Gromov, M. Guan, Y. Guardincerri, M. Gulino, B. R. Hackett, M. H. Hassanshahi, K. Herner, B. Hosseini, D. Hughes, P. Humble, E. V. Hungerford, Al. Ianni, An. Ianni, V. Ippolito, I. James, T. N. Johnson, Y. Kahn, K. Keeter, C. L. Kendziora, I. Kochanek, G. Koh, D. Koralev, G. Korga, A. Kubankin, M. Kuss, M. La Commara, M. Lai, X. Li, M. Lisanti, M. Lissia, B. Loer, G. Longo, Y. Ma, A. A. Machado, I. N. Machulin, A. Mandarano, L. Mapelli, S. M. Mari, J. Maricic, C. J. Martoff, A. Messina, P. D. Meyers, R. Milincic, S. Mishra-Sharma, A. Monte, M. Morrocchi, B. J. Mount, V. N. Muratova, P. Musico, R. Nania, A. Navrer Agasson, A. O. Nozdrina, A. Oleinik, M. Orsini, F. Ortica, L. Pagani, M. Pallavicini, L. Pandola, E. Pantic, E. Paoloni, F. Pazzona, K. Pelczar, N. Pelliccia, V. Pesudo, A. Pocar, S. Pordes, S. S. Poudel, D. A. Pugachev, H. Qian, F. Ragusa, M. Razeti, A. Razeto, B. Reinhold, A. L. Renshaw, M. Rescigno, Q. Riffard, A. Romani, B. Rossi, N. Rossi, D. Sablone, O. Samoylov, W. Sands, S. Sanfilippo, M. Sant, R. Santorelli, C. Savarese, E. Scapparone, B. Schlitzer, E. Segreto, D. A. Semenov, A. Shchagin, A. Sheshukov, P. N. Singh, M. D. Skorokhvatov, O. Smirnov, A. Sotnikov, C. Stanford, S. Stracka, G. B. Suffritti, Y. Suvorov, R. Tartaglia, G. Testera, A. Tonazzo, P. Trinchese, E. V. Unzhakov, M. Verducci, A. Vishneva, B. Vogelaar, M. Wada, T. J. Waldrop, H. Wang, Y. Wang, A. W. Watson, S. Westerdale, M. M. Wojcik, M. Wojcik, X. Xiang, X. Xiao,

- C. Yang, Z. Ye, C. Zhu, A. Zichichi, and G. Zuzel. Low-Mass Dark Matter Search with the DarkSide-50 Experiment. *arXiv e-prints*, page arXiv:1802.06994, February 2018.
- [159] Tanner Trickle. Exceed-dm: Extended calculation of electronic excitations for direct detection of dark matter. *arXiv preprint arXiv:2210.14917*, 2022.
- [160] Tanner Trickle, Zhengkang Zhang, Kathryn M Zurek, Katherine Inzani, and Sinéad M Griffin. Multi-channel direct detection of light dark matter: theoretical framework. *Journal of High Energy Physics*, 2020(3):1–36, 2020.
- [161] G Tupper. Acoustic čerenkov radiation by supersonic neutrons. *Physical Review B*, 36(10):5574, 1987.
- [162] Teresa Marrodan Undagoitia and Ludwig Rauch. Dark matter direct-detection experiments. *Journal of Physics G: Nuclear and Particle Physics*, 43(1):013001, 2015.
- [163] Lucas Valenca Soares Bezerra. Supercdms event reconstruction using convolutional neural networks. Master’s thesis, University of British Columbia, 2020.
- [164] Adriaan Van den Bos. A Cramér-Rao lower bound for complex parameters. *IEEE Transactions on Signal Processing*, 42 (10), 1994.
- [165] KM Van Vliet. Derivation of the fluctuation-dissipation theorem. *Physical Review*, 109(4):1021, 1958.
- [166] JB Wallace, LB Aji, AA Martin, SJ Shin, L Shao, and SO Kucheyev. The role of frenkel defect diffusion in dynamic annealing in ion-irradiated si. *Scientific reports*, 7(1):1–7, 2017.
- [167] Scott Watson, Bobby Samir Acharya, Gordon Kane, and Piyush Kumar. A non-thermal wimp miracle. 2009.
- [168] FC Wellstood, C Urbina, and John Clarke. Hot-electron effects in metals. *Physical Review B*, 49(9):5942, 1994.
- [169] N. Wiener. *Time Series*. M.I.T. Press, 1964.
- [170] Norbert Wiener. Generalized harmonic analysis. *Acta mathematica*, 55(1):117–258, 1930.
- [171] Dongchuan Yu, Fang Liu, and Pik-Yin Lai. Input reconstruction of chaos sensors. *Chaos: An Interdisciplinary Journal of Nonlinear Science*, 18(2):023106, 2008.
- [172] To Chin Yu. Template-free pulse height estimation of microcalorimeter responses with pca. *arXiv preprint arXiv:1910.14261*, 2019.

- [173] Marios Zacharias and Feliciano Giustino. One-shot calculation of temperature-dependent optical spectra and phonon-induced band-gap renormalization. *Physical Review B*, 94(7):075125, 2016.
- [174] Marios Zacharias, Christopher E Patrick, and Feliciano Giustino. Stochastic approach to phonon-assisted optical absorption. *Physical review letters*, 115(17):177401, 2015.
- [175] Huaguang Zhang, Derong Liu, and Zhiliang Wang. *Controlling chaos: suppression, synchronization and chaotification*. Springer Science & Business Media, 2009.
- [176] Tianjun Zhang, Zhewei Yao, Amir Gholami, Joseph E Gonzalez, Kurt Keutzer, Michael W Mahoney, and George Biros. Anodev2: A coupled neural ode framework. *Advances in Neural Information Processing Systems*, 32, 2019.
- [177] CX Zhao, Wen Xu, and FM Peeters. Cerenkov emission of terahertz acoustic-phonons from graphene. *Applied physics letters*, 102(22):222101, 2013.
- [178] Beata Ziaja, Richard A. London, and Janos Hajdu. Unified model of secondary electron cascades in diamond. *Journal of Applied Physics*, 97(6):064905, 2005.